Supersonic Quiet-Tunnel Development for Laminar-Turbulent Transition Research: Final Report for NASA Langley Grant NAG-1-1607

P-172

Steven P. Schneider

Assistant Professor of Aerodynamics

School of Aeronautical and Astronautical Engineering

Purdue University

West Lafayette, IN 47907-1282

Abstract

This grant supported research into quiet-flow supersonic wind-tunnels, between February 1994 and February 1995. Quiet-flow nozzles operate with laminar nozzle-wall boundary layers, in order to provide low-disturbance flow for studies of laminar-turbulent transition under conditions comparable to flight. Major accomplishments include: (1) development of the Purdue Quiet-Flow Ludwieg Tube, (2) computational evaluation of the square nozzle concept for quiet-flow nozzles, and (3) measurement of the presence of early transition on the flat sidewalls of the NASA LaRC Mach 3.5 supersonic low-disturbance tunnel. Since items (1) and (2) are described in the final report for companion grant NAG-1-1133, only item (3) is described here.

1   Introduction

The general goals and background for this program were reported on recently in the final report for NASA Grant NAG-1-1133 [7], so these will not be repeated here. The grant reported on here supported additional graduate-student efforts closely related to those supported under NAG-1-1133. Items (1) and (2) from the abstract were reported on recently in the final report for NAG-1-1133 [7]. Some of the details for item (2) are contained in reference [1], which was completed after submission of reference [7] and is appended to this report. No further summary of items (1) and (2) will be presented here.

Grant NAG-1-1607 also supported hot-wire measurements in the boundary layers on the flat sidewalls of the 2D NASA LaRC Mach 3.5 quiet tunnel, which were carried out during the summer of 1994 by Christine Haven (who was also supported under NAG-1-1133). These measurements were carried out in order to determine the Reynolds numbers at which the boundary layers on the sidewalls became turbulent. Computations of the boundary layers on the sidewalls of square nozzles [7] had provided clear evidence supporting earlier conjectures that transition on the sidewalls of square and rectangular nozzles is dominated by the crossflow instability. These computations also indicated that transition would occur very early due to this crossflow instability. This expectation of early transition on flat sidewalls subject to the 3D crossflow instability was supported by earlier unpublished pitot-probe measurements on the flat sidewalls of the NASA LaRC Mach 3.5 supersonic low-disturbance tunnel (SLDT) (S. Wilkinson, private communication).

This early transition on the flat sidewalls is very significant to design of quiet-tunnel nozzles, for it suggests the following:

1. The bleed slots for the flat sidewalls probably do not affect transition on the sidewalls, since transition still occurs near the throat due to crossflow. The turbulent boundary layer will be somewhat thinner with the bleed slots present, but it is hard to see why this would have a substantial effect on the size of the quiet flow region, although it would affect the radiated frequencies. Since these bleed slots add substantial mechanical complexity and cost, they should probably be omitted from future 2D designs.

2. The rapid-expansion design is essential to the success of the Mach 3.5 SLDT (with the 2D nozzle [2, 3]). The size of the quiet-flow region in a 2D nozzle is probably dominated by the noise radiating inward along Mach lines from the sidewalls (beginning at a point where the sidewall Mach number is 1.5 to 2, and the radiation becomes significant [5]). Inviscid computations carried out with the codes described in reference [7] indicate that longer nozzles cause the noise from the sidewalls to affect the centerline flow closer to the beginning of the uniform flow region. This makes a rapid expansion crucial to limiting the sidewall problem, since the only alternative is a very wide nozzle in which most of the massflow is wasted. However, recent work has found that a slow-expansion design is essential to achieving high Reynolds number quiet flow through reductions in the Görtler instability on the curved nozzle walls [9]. This conflict between the requirements for limiting the noise

2

from the sidewalls and the curved walls makes 2D nozzles unattractive for future high-Reynolds number quiet-flow designs.

The significance of these sidewall transition issues made further measurements of transition on the sidewalls of the existing nozzle a priority. Clear measurements of the transition location would remove some of the uncertainty involved in the arguments. In order to obtain these measurements, Christine Haven spent the summer of 1994 in residence at NASA Langley attempting to set up and perform hot-wire measurements of the state of the sidewall boundary layer under various conditions. These measurements form the second part of her M.S. thesis [4]. Less than two days of tunnel access were provided, due to other priorities for the tunnel schedule. Unfortunately, this proved to be a severe limitation, since unexpected difficulties with noise generated by the traversing mechanism seriously corrupted the hot-wire data, and available resources did not allow for correcting the problem and re-acquiring the data.

In spite of these difficulties with the noise in the data, some fairly definite conclusions can be drawn regarding the state of the sidewall boundary layer. The evidence for these conclusions is summarized in the balance of this report.

2   Hot-Wire Measurements in the Flat Sidewall of the Mach 3.5 SLDT

Most of the details of Christine Haven's work in the SLDT at Langley are contained in her M.S. thesis [4]. Since some 256 megabytes of data were acquired, not all aspects of this work can be presented. The thesis has not been appended to this report, since the noisy quality of the data make the conclusions less clearcut, and the presentation does not match the quality of reference [1].

The data was acquired with a LeCroy model 9424 oscilloscope with 8-bit resolution. Records of 40,000 bytes were acquired at 400kHz using a prototype constant-voltage anemometer made by AS&M. The wire was placed about 0.025 inches above the flat wall of the nozzle, and was moved streamwise and spanwise to sample different locations, which were mostly in the corners and in the exit plane. Data was also taken on the centerline of the tunnel for comparison to earlier measurements. Further details can be found in reference [4].

The large amount of noise in the data is evident from Figure 1, which shows the power spectrum of the hot-wire data at the nozzle exit. The conditions for the 3 files plotted can be found in Table 1. File r1_45 was
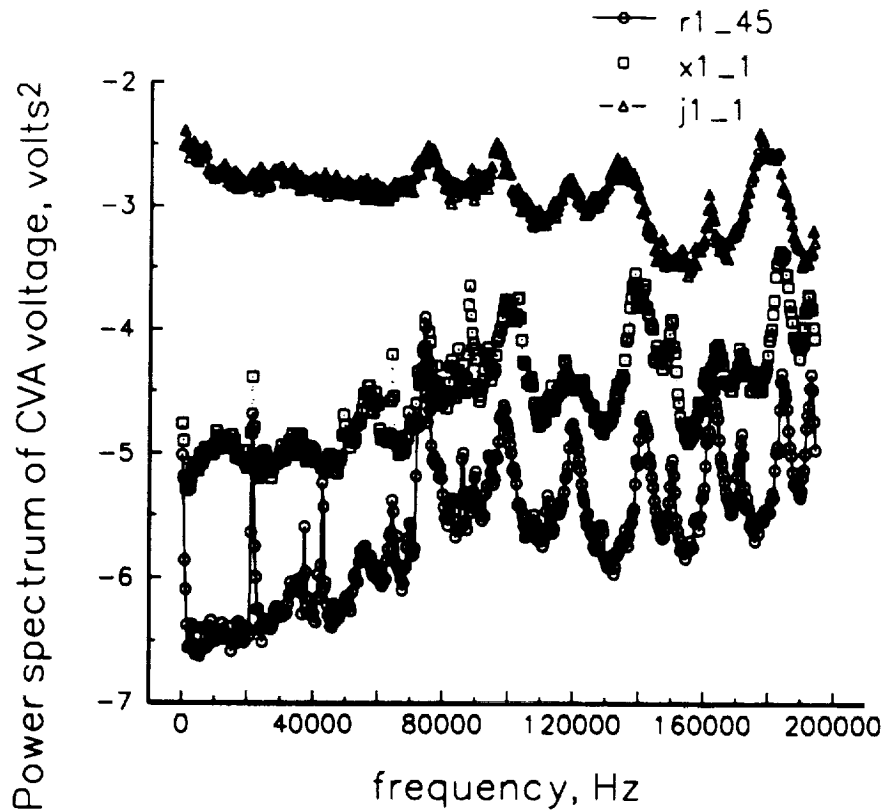
3

Figure 1: Power Spectrum of Hot-Wire Data at Various Conditions

obtained under what were probably quiet flow conditions, whereas the other two files are probably of turbulent flow. The data show many spikes which were traced to electromagnetic interference from the DC motors in the traversing mechanism. Since most of the noise is above 50kHz, the signal to noise ratio can be enhanced by looking only at the signal content in the 0-50kHz band.

Haven plots the power content in this 0-50kHz band in Table 2 in her thesis [4], and in figures 38-45. The power content is really in units of volts squared, but is mislabeled there as volts squared per second. In addition, there is an erroneous constant factor in her results. The original data that is cited in Table 2 of the thesis was reprocessed using a carefully checked spectral analysis program written by the author and based on reference [6]. This spectral program computes and checks Parseval's theorem for each dataset processed. The results are shown in Table 1.

Here, x is the streamwise distance from the throat, in inches, y is the

file	x	y	P_0	V_m	$V'_{50,h}$	V'_{50}	$V'_{50,h}/V'_{50}$	V'_{50}/V_m
d1_45	3.95	1.92	11.1	2.24	2.35	0.276	8.5	0.12
j1_1	15.07	3.01	34.0	2.52	4.10	0.483	8.5	0.19
k1_1	15.47	3.00	4.8	2.08	0.73	0.087	8.4	0.04
p1_1	15.47	3.00	28.2	2.38	1.54	0.182	8.5	0.08
r1_45	4.22	0.0	9.1	2.61	0.09	0.011	8.2	0.004
x1_1	15.22	0.0	68.3	3.05	0.30	0.036	8.3	0.012

Table 1: Sample Data from Haven (1995)

spanwise distance from the centerplane, in inches, P_0 is the stagnation pressure in psia, and V_m is the mean CVA output voltage in volts. Files d1_45 and j1_1 were measured in the corner, k1_1 and p1_1 were measured on the sidewall in the exit plane, and r1_45 and x1_1 were measured on the tunnel centerline. Also, $V'_{50,h}$ is the rms power content in the fluctuating signal between 0 and 50kHz, as computed by Haven (the square root of the data in column 6 of her table 2, p. 62 in [4]), and V'_{50} is the rms power content in the fluctuating signal between 0 and 50kHz as recomputed by the author. This makes V'_{50}/V_m the normalized power content in the 0 to 50kHz range. Note that the ratio of $V'_{50,h}$ to V'_{50} is consistently about 8.4. It thus appears that Haven has an erroneous but consistent constant factor of 8.4 in her conversion from the signal to the integrated power. The rest of the data reported here will use Haven's processed results, but correct them using this factor of 8.4.

Since the signals and spectra are corrupted by noise, it is difficult to determine which of the data correspond to laminar conditions and which to turbulent. Without knowledge of the amplitude of the fluctuations, only a rather uncertain assessment can be made [4]. However, Haven acquired data on the centerline of the tunnel at known freestream conditions with the same hot wire used to acquire most of the rest of the data. The massflow can be computed for these conditions and compared to the hot-wire mean voltage. The results are presented in figure 2, which reproduces figure 19 from reference [4]. It can be seen that the data form a consistent set. Since all the data was acquired with the same overheat ratio, 1.3, which is fairly high, it is reasonable to assume that the voltage is primarily responding to massflow fluctuations. Since the stagnation temperature was not changed during the run, and neither was the hot-wire voltage, the only mean temperature change would be that present in the boundary layer due to viscous heating effects. Since this cannot be determined from Haven's data, which was obtained at a single overheat, it will be neglected here. The assumption will be made that the wire is responding primarily to massflow fluctuations, due to the high over-
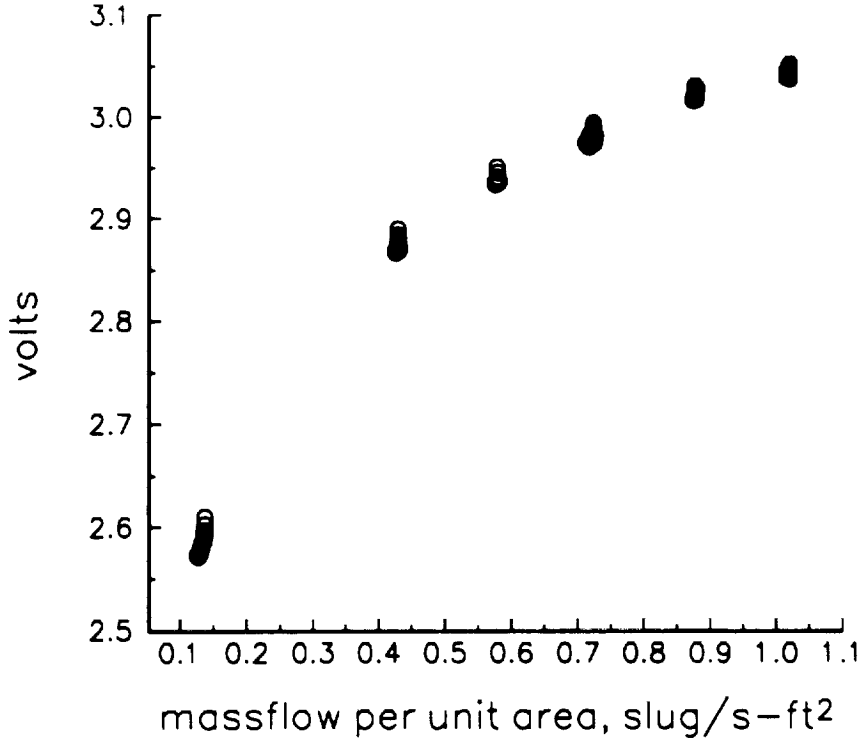
Figure 2: Calibration of Wire One Used by Haven

heat. This is a common assumption in CTA work [8], although the validity in the present case is unknown.

If the voltage V is then assumed to depend only on the massflow ρu, we can derive a relation between the normalized voltage fluctuations and the normalized massflow fluctuations by assuming small disturbances. Using a Taylor expansion, we find that

$$V'/V_m = \frac{dV}{d(\rho u)} \frac{(\rho u)_m}{V_m} \frac{(\rho u)'}{(\rho u)_m}.$$

Here, V' is the fluctuating part of the voltage, V_m is the mean, $(\rho u)'$ is the fluctuating part of the massflow, and $(\rho u)_m$ is the mean. Although the small disturbance approximation is not valid for some of the data, it is a useful first approximation. Examination of figure 2 shows that $dV/d(\rho u)$ varies from roughly 1 at $V_m = 2.6$ to about $1/4$ at $V_m = 3.0$, and $(\rho u)_m/V_m$ varies from about $1/20$ at $V_m = 2.6$ to about $1/4$ at $V_m = 3.0$. The combined conversion

6

factor, $[dV/d(\rho u)][(\rho u)_m/V_m]$, varies from about 1/20 to about 1/16 over the same range. Values of this factor for smaller values of V_m will be smaller than 1/20, by an unknown amount. This makes the normalized massflow fluctuations about 16 to 20 times larger than the normalized voltage fluctuations, for small fluctuation levels.

Using this rough calibration, we can then estimate the values of the normalized rms massflow fluctuations using the normalized rms voltage fluctuations shown in Table 1. It seems clear that only file r1_45 on the centerline can represent non-turbulent fluctuations. The fluctuations present even in this file are much larger than those measured in earlier, accurate LaRC data, but the difference is probably due to the additional electromagnetic interference noise in the present data. The data in the boundary layer from the flat sidewall all contain normalized massflow fluctuations that seem to be above 10 percent, and the corner data also seem to be above 10 percent. This amplitude data provide additional evidence that the flow on the flat sidewall of the nozzle is turbulent, although the several assumptions present in the calibration preclude drawing a firm conclusion.

Data for the centerline fluctuations reduced using the process is shown in figure 3. These were taken under conditions where previous LaRC data showed a transition from quiet to noisy flow at about 11 inches from the throat. Since the mean voltage is about 3 volts, the normalized massflow fluctuations can be taken as about 16 times the normalized voltage fluctuations. The high fluctuation levels present in the upstream regions are presumably due to the electromagnetic noise from the traverse.

The rms fluctuation levels for the lowest Reynolds number sidewall data are shown in figure 4. The data were taken at a total pressure of about 9 psia, the lowest pressure achieved during the runs. Four lines are plotted, for data taken along four different streamwise lines that are different distances from the curved wall. The four values of y_{exit} for the four curves are the distance between the data-acquisition line and the centerplane, at the exit. The line with the smallest value of y_{exit} is still fairly near the corner, about 6/7 of the distance from the centerplane to the corner. The figure reproduces the data in Figure 39 of reference [4], except for the corrected scaling. It appears from the large values of the normalized voltage fluctuations that the flow is turbulent for all cases. The data for the $y_{exit} = 2.63$ case near the throat exhibits a large amplitude spike in the spectra at about 15 kHz; this spike decreases in amplitude as the probe is moved downstream, until it is washed out in the general turbulence. Although this interesting spike may represent the instability waves that cause the transition, it is not emphasized here because there is no way to be sure that it was not caused by probe vibration or some

7

Centerline Hot—Wire Data at 48.4 psia total pressure
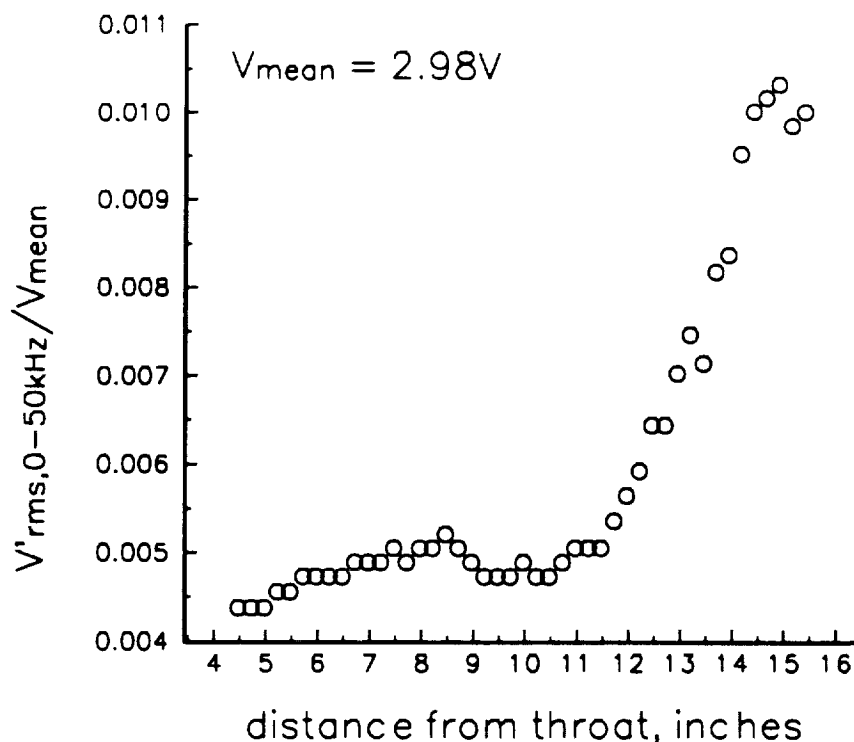data reprocessed from fig. 38 of Haven (1995)

Figure 3: Normalized Fluctuations on the Centerline

other interfering effect.

3   Summary

This graduate-education grant supported in part work by three master's students: Timothy Alcenius, Christine Haven, and Laura Randall. Although Alcenius was interested in continuing for a PhD, the early termination of the original 3-year graduate-student-education grant (after one year) forced Alcenius to obtain other employment. His work, and the first part of Haven's work, is reported on elsewhere [7]. The second part of Haven's work involved hot-wire measurements in the boundary layer of the flat sidewalls in the NASA Langley Mach 3.5 low-disturbance tunnel. As shown above, these provide further evidence that transition occurs very early on these flat sidewalls, which are in effect always turbulent. Seven months of Randall's two-year M.S. pro-
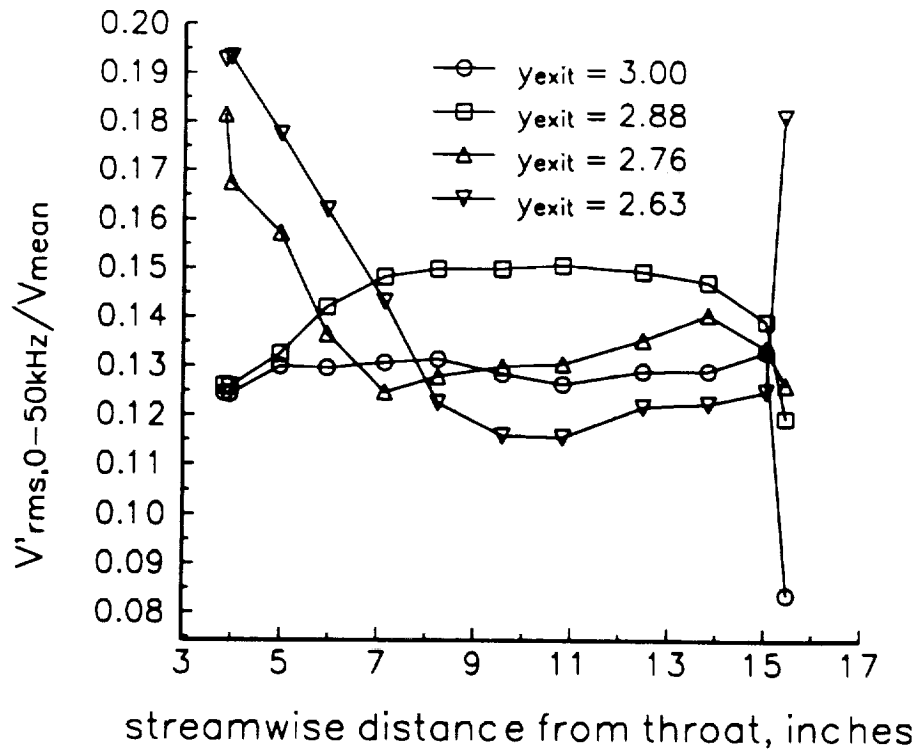
Figure 4: Normalized Fluctuations on the Flat Sidewall
9 psia total pressure, various distances from centerplane

gram were also supported by this grant, at half of the usual student stipend. Her M.S. thesis is expected to appear in July 1995.

4 Acknowledgements

5 References

[1] Timothy John Alcenius. Development of square nozzles for high-speed, low-disturbance wind tunnels. Master's thesis, School of Aeronautics and Astronautics, Purdue University, December 1994.

[2] I.E. Beckwith and W.O. Moore III. Mean flow and noise measurements in a Mach 3.5 pilot quiet tunnel. Paper 82-0569, AIAA, 1982.

[3] F.-J. Chen, M. R. Malik, and I.E. Beckwith. Boundary-layer transition on a cone and flat plate at Mach 3.5. *AIAA Journal*, 27(6):687–693, 1989.

[4] Christine Elizabeth Haven. Measurements of laminar-turbulent transition on supersonic wind tunnel walls. Master's thesis, School of Aeronautics and Astronautics, Purdue University, May 1995.

[5] John Laufer. Aerodynamic noise in supersonic wind tunnels. *Journal of Aerospace Sciences*, 28:685–692, 1961.

[6] W. H. Press, B. P. Flannery, S. A. Teukolsky, and W. T. Vetterling. *Numerical Recipes: The Art of Scientific Computing*. Cambridge University Press, Cambridge, 1986.

[7] Steven P. Schneider. Development of quiet-flow supersonic wind tunnels for laminar-turbulent transition research. Contractor Report CR-197286, NASA, January 1995.

[8] E.F. Spina and C.B. McGinley. Constant-temperature anemometry in hypersonic flow: Critical issues and sample results. *Experiments in Fluids*, 17:365–374, 1994.

[9] S. P. Wilkinson, S. G. Anders, and F.-J. Chen. Status of Langley quiet flow facility developments. Paper 94-2498, AIAA, 1994. Presented at the June 1994 Ground Testing Conference.

A Appendix: Timothy Alcenius's Master's Thesis

DEVELOPMENT OF SQUARE NOZZLES FOR HIGH-SPEED,

LOW-DISTURBANCE WIND TUNNELS

A Thesis

Submitted to the Faculty

of

Purdue University

by

Timothy John Alcenius

In Partial Fulfillment of the

Requirements for the Degree

of

Masters of Science in Aeronautical and Astronautical Engineering

December 1994

For Jenny, whose love, support, and faith have helped me go further than I ever could
have on my own.

ACKNOWLEDGMENTS

TABLE OF CONTENTS

LIST OF TABLES

LIST OF FIGURES

NOMENCLATURE

a	Speed of Sound
c	Phase Speed
C1	Transition Estimation Technique of Arnal and Coustols
e	Internal Energy
H	Compressibility Correction in Reed and Haynes Crossflow Reynolds Number
H_{shp}	Streamwise Shape Factor
L	Cooling Correction in Reed and Haynes Crossflow Reynolds Number
M	Mach Number
M_B	Mach Number at the End of the Radial Flow Region for the Axisymmetric Design
M_C	Nozzle Design Mach Number
M_e	Local Edge Mach Number
N	Natural Logarithm of the Amplitude Ratio of a Boundary-Layer Disturbance Mode to its Initial Value
N_G	N-Factor for the Görtler Instability
N_{TS}	N-Factor for Tollmien-Schlichting Waves
P	Pressure
P_o	Stagnation (Total) Pressure
P_{oedge}	Total Pressure at Boundary-Layer Edge
P_{oFS}	Freestream Total Pressure
P_{omax}	Maximum Calculated Total Pressure
P_{owall}	Total Pressure at the Wall
Pr	Prandtl Number
q_x, q_y, q_z	Heat-Flux in the x, y, and z directions
R	Reed and Haynes Transition Estimator

R_a	Radius of Curvature
R_{cf}	Standard Crossflow Reynolds Number
$R_{cfR\&H}$	Reed and Haynes Crossflow Reynolds Number
$R_{cf_{tr}}$	Transition Crossflow Reynolds Number
$R_{\delta 2}$	Crossflow Reynolds Number by Beasley
$R_{\Delta x}$	Quiet-Test Reynolds Number
Re_L	Reynolds Number Based on Reference Length L
r_{th}	Throat Radius
R_∞	Unit Reynolds Number
T	Temperature
T_o	Stagnation Temperature
T_w	Local Wall Temperature
u, v, w	Velocity Components in the x, y, and z-directions
U_e	Edge Velocity
U_∞	Freestream of Reference Velocity
W	Crossflow Velocity
W_{MAX}	Maximum Crossflow Velocity in a Given Profile
x, y, z	Directions Parallel (x) and Perpendicular (y,z) to the Nozzle Axis
α	Wave Number
γ	Ratio of Specific Heats
δ^*	Displacement Thickness
$\delta 10$	Farthest Distance from Wall where Crossflow is 10% of W_{MAX}
η_{edge}	Distance from Wall to Boundary-Layer Edge
μ	Viscosity
ν_e	Kinematic Viscosity at the Boundary-Layer Edge
ϕ	Disturbance Angle with respect to the Wall
θ	Momentum Thickness
θ_a	Approach Angle
θ_w	Nozzle Wall Angle at the Inflection Point
ρ	Density
$\tau_{xx}, \tau_{yy}, \tau_{zz}$	Shear-Stress Tensor along Specific Faces
$\tau_{xy}, \tau_{xz}, \tau_{yz}$	
ξ, η, ζ	Streamwise and Two Normal-to-Wall Computational Coordinates
ω	Frequency ($= \alpha c$)
∞	Subscript Referring to a Freestream or Reference Condition

ABSTRACT

Alcenius, Timothy John. M. S., Purdue University, December, 1994. Development of Square Nozzles for High-Speed, Low-Disturbance Wind Tunnels. Major Professor: Steven P. Schneider.

Wind tunnels with low freestream disturbances are required to advance boundary-layer stability and transition research and provide accurate transition prediction methods for advanced aircraft. Developments in quiet-tunnel technology are reviewed. Also reviewed are the types of nozzles used for wind tunnel designs and the boundary-layer disturbances inherent in these designs. Three-dimensional nozzles may be best suited for quiet-flow tunnels if the boundary-layer crossflow remains small. To study the three-dimensional design for quiet nozzles, the flow fields in two Mach 2.4 nozzles were numerically simulated. Some design results for a Mach 8 nozzle are also presented. Preliminary estimates of crossflow-induced transition in the wall boundary-layers of the Mach 2.4 nozzles indicate that transition is likely to occur near the throat in both nozzles. A simple analysis of the crossflow pressure gradient in the throat is also presented. This preliminary analysis indicates that a radius of curvature of 10 throat radii or greater may be necessary to eliminate transition in the throat region.

CHAPTER I INTRODUCTION

Accurate methods of estimating the location of boundary-layer transition are required for the development of aircraft for the Twenty-first Century, such as the High-Speed Civil Transport and NASP. To verify advanced computational fluid dynamics (CFD) codes used in the design of such aircraft, new ground test facilities must be developed. These facilities must be capable of obtaining transition Reynolds numbers on models comparable to those from flight data.

The many factors involved in high-speed boundary-layer transition make it difficult to understand (see Morkovin [1]). To advance current knowledge, stability experiments in both the supersonic and hypersonic regimes are needed to clarify experimental and theoretical discrepancies [2,3]. New low-disturbance wind tunnels are essential for this purpose [4].

Pate and Schueler [5] conclusively showed that wind tunnel noise was the major influencing factor in the scatter of measured transition Reynolds numbers on similar experiments in different experimental facilities. The high noise levels generally observed were caused by eddy Mach wave radiation from the turbulent boundary-layers on the nozzle walls [6]. Efforts by NASA Langley Research Center to develop quiet supersonic wind tunnels have shown that laminar boundary-layers are required on the nozzle walls. Measured transition Reynolds numbers on test models in quiet tunnels were then found to be as high as those observed in flight [7].

To introduce the laminar-flow control problem for wind tunnels, quiet-tunnel developments will first be reviewed. Then the types of nozzles used in quiet-tunnel designs will be discussed along with their inherent advantages and disadvantages. Disturbances that can cause boundary-layer transition will then be reviewed with emphasis on their application to quiet-tunnel design. Finally, the objectives of this research will be presented.

1.1 Quiet-Tunnels

The considerable scatter in transition data from various conventional tunnels showed that new tunnels with low-freestream disturbances were necessary to provide accurate transition measurements. Since Laufer [6] had shown that wind tunnel noise was primarily due to the noise radiated along Mach lines from turbulent nozzle-wall boundary-layers, one of the main goals was to keep the boundary-layers laminar as far downstream of the throat as possible. Attempts to use shielding devices [8] and rapid-expansion nozzles with fully turbulent wall boundary-layers [9] were made. However, maintaining laminar boundary-layers along the nozzle walls proved to be more practical than either of these methods. Reviews of the evolution of high-speed quiet tunnel technology can be found in references 4 and 10.

The first operational quiet tunnel was the Mach 3.5 Pilot Tunnel at NASA Langley. Measurements showed that the quiet-test length in this tunnel decreased from 25 to 13 cm as the freestream unit Reynolds number (R_∞) ncreased from 1 to 3 x 10^7 m^{-1}. Efforts to maximize the quiet length Reynolds number ($R_{\Delta x}$) were then made to advance future designs. The first theoretical advance was determining how the nozzle design parameters affected the length of the quiet-test region. Calculations using the e^N method [11] showed that transition was caused by the formation and amplification of Görtler vortices along the concave part of the nozzle walls, instead of by the amplification of Tollmien-Schlichting waves. This result led to the design of a "slow-expansion" nozzle [12].

The maximum wall angle at the inflection point of slow-expansion nozzles is much smaller than for rapid-expansion nozzles [11]. With the use of small wall angles, it is possible to insert a region of radial flow corresponding to a straight line wall section, inclined at the wall angle, upstream of the inflection point. This design change delayed the onset of the Görtler vortices and reduced their growth rates by moving the inflection point far downstream where the boundary-layer is much thicker and the radius of curvature of the concave wall is much larger. Even though the Görtler number doesn't change much, longer nozzles give smaller values of integrated amplification for the Görtler instability [13]. The $R_{\Delta x}$ values are then considerably larger than in the rapid-expansion nozzles. Measurements confirmed these predictions.

Reviews of the current facilities at NASA Langley are given in references 10 and 14. Background for new facilities at NASA Ames and Purdue University is given in references 15 and 16 respectively. Heating of the nozzle walls can also be used to maintain laminar boundary-layers. Background for the nozzle used in the investigation

of this method at Montana State University is given in reference 17 and the heating results in reference 18.

1.2 Nozzle Types

Generally, three types of nozzles are used for supersonic wind tunnels. These are: axisymmetric (circular cross-sections), two-dimensional (two contoured walls and two flat sidewalls), and three-dimensional (four contoured walls with square or rectangular cross-sections). Each has advantages and disadvantages to its use in a quiet-tunnel design. These are discussed below.

1.2.1 Axisymmetric Nozzles

The main advantage in using an axisymmetric nozzle is that stability issues that are inherent in two and three-dimensional nozzles are not present. Specifically, flow in corners and boundary-layer crossflow, which can cause stability problems, do not occur. Also, this type of nozzle will generally require a smaller mass flow rate than a two-dimensional nozzle with the same throat height. Finally, tolerances are easier to maintain in hypersonic nozzles since they have small, heated throats.

There are, however, several disadvantages in using this type of design. First, machining imperfections can cause disturbances that are then focused along the axis of the nozzle. This may require smaller machining tolerances during fabrication to assure that freestream noise levels would be small. Also, the surface finish is difficult to maintain in the most critical location, the throat, due to access problems. Another problem is that long nozzles must be built in sections. This means that the joints between sections must be perfect or the same focusing effect caused by wall waviness would occur due to the surface discontinuities. The main disadvantage, however, is that circular walls complicate the use of optical grade windows. This means that standard flow visualization techniques such as Schlerien would be difficult to use in this type of nozzle. Since optical diagnostics are a highly desirable feature, this is a major limiting factor. However, new focusing Schlerien systems make straight walls non-essential for flow visualization using this technique.

1.2.2 Two-Dimensional Nozzles

The two-dimensional design has several advantages over the axisymmetric design. First, since all the walls are fabricated separately and the cross-sections are rectangular, disturbances created by machining imperfections will not focus on the nozzle centerline. The disturbances will instead be laterally distributed across the flow. For this reason, machining tolerances are not as strict as in the axisymmetric design. Second, flat sidewalls allow for the use of optical diagnostics. Third, the nozzle can be taken apart to allow access to the throat region for polishing and maintenance. Finally, the long span between the two sidewalls can accommodate wider test models than the axisymmetric or three-dimensional designs would allow. However, noise from the sidewall boundary-layer could cause premature transition on the model if the model is too wide.

The main problem with two-dimensional nozzles for quiet-flow applications is that transition on the sidewalls and in the corners is not well understood. To avoid these problems, the nozzles are made wide enough so that noise radiated from the sidewall boundary-layers and the corners will not affect the test region. The drawbacks to this approach are the increased cost necessary for a large nozzle, and the larger mass flow rates required. Finally, in high Mach number, two-dimensional nozzles the throat becomes so narrow and hot that it becomes impossible to maintain tolerances.

1.2.3 Three-Dimensional Nozzles

Three-dimensional nozzles seem to provide a compromise between the other two designs. The large mass flow rates that are required for wide two-dimensional nozzles are not needed for this design (assuming the throat heights are the same). Also, since all the walls are machined separately, the focusing effect that is evident in the axisymmetric nozzle does not occur. Like two-dimensional nozzles, these nozzles can also be taken apart for access to the throat for polishing and maintenance. Finally, use of optical grade windows is easier than in the axisymmetric design.

The main drawback in this type of nozzle is the lack of understanding of the transition mechanics due to crossflow and cornerflow. If further investigations can show these effects to be minimal or provide reasonable measures to limit the growth of these disturbances, this type of nozzle design may prove to be the most viable for quiet-flow applications.

1.3 Types of Disturbances

Transition is a complicated process which is initiated by disturbances entering the boundary-layer. The process of entering the boundary-layer is known as receptivity and presently is poorly understood. After entering the boundary-layer, disturbances can grow or decay in either a linear or nonlinear fashion depending on their size and how they interact. Finally, they become large enough that the boundary-layer begins to become unstable and turbulent bursts are formed. Soon after, the entire boundary-layer will be turbulent. Reshotko [2] reviews the current knowledge of receptivity and disturbance evolution.

Many different types of disturbances exist that can adversely affect boundary-layer stability. Since quiet-flow nozzles require laminar boundary-layers along the nozzle walls as far downstream of the throat as possible, it is desirable to keep all disturbances to a minimum. The boundary-layer stability on wind tunnel walls is evaluated by analyzing first and second mode viscous instability waves (first mode is otherwise known as Tollmien-Schlichting waves), Taylor-Görtler vortices, wall roughness effects, corner flows, and crossflow. The effects that these disturbances have on boundary-layer stability can be estimated using Reynolds number correlations, linear stability analysis (e^N), or the Parabolized Stability Equations (PSE) [19, 20]. However, these techniques are not capable of predicting transition when the disturbances become nonlinear. This happens when two of more disturbance waves interact and create a wave which is nonlinear.

1.3.1 Tollmien-Schlichting Waves

The continuity and Navier-Stokes relations can be manipulated to obtain the set of linearized disturbance equations. By assuming incompressible flow, no buoyancy effects, no curvature, and parallel flow for the basic flow and the disturbances, the most general form of a three-dimensional disturbance is found to be a traveling wave whose amplitude varies with y and moves along the wall at angle ϕ with respect to the x-axis [21]. These are referred to as Tollmien-Schlichting waves and can be written as:

$$(\hat{u}, \hat{v}, \hat{w}, \hat{p}) = [u(y), v(y), w(y), p(y)] \exp\{i\alpha(x\cos\phi + z\sin\phi - ct)\} \qquad (1)$$

where

α   Wave Number

c   Phase Speed

ω   Frequency $(= \alpha c)$

These waves form one type of laminar-flow instability.

To gain insight into the effect of these waves on nozzle-wall boundary-layer stability, an understanding of how pressure gradient affects wave growth must be developed. Nozzles with supersonic test sections have favorable pressure gradients if no shock waves are present. Wazzan, as shown in White [21], computed the neutral stability curves for the Falkner-Skan wedge-flow profiles. The results of this work showed that favorable pressure gradients strongly retard the amplification of Tollmien-Schlichting waves while adverse gradients promote them.

The amplification of TS waves must still be considered, however, especially in slow-expansion nozzles. The e^N method from linear stability theory is the preferred method for computing amplification of these waves. The value of N_{TS} at the location where $N_G = 9$ (the location where transition takes place due to the Görtler instability) was negligible for the Mach 3.5 rapid-expansion nozzle but increased for the slow-expansion nozzles to 2.3 for the Mach 3.5 axisymmetric nozzle [12], to 3.6 for the Mach 6 axisymmetric nozzle [22], and to 4.5 for the Mach 2.4 axisymmetric nozzle [23]. Although, TS waves have not become large enough to cause transition in slow-expansion nozzle designs, this must be verified for each new design.

1.3.2 Taylor-Görtler Vortices

Taylor-Görtler vortices are counter-rotating vortices in viscous regions created by centrifugal instabilities. Rayleigh, as quoted in White [21], found that: "An inviscid rotating flow is unstable if the square of its circulation decreases outward." In other words, if the square of the product of the radius and the velocity decreases with increasing radius, the flow is unstable. Figure 1 [24] shows these vortices in the boundary-layer flow over a concave wall.

As Beckwith, Malik, and Chen [11] noted, in supersonic nozzles, a uniform test region cannot be produced without a concave wall to cancel initial expansion waves. Therefore, the Görtler instability will be present in any supersonic nozzle design. It also should be noted that a concave region must also exist in the subsonic portion of the
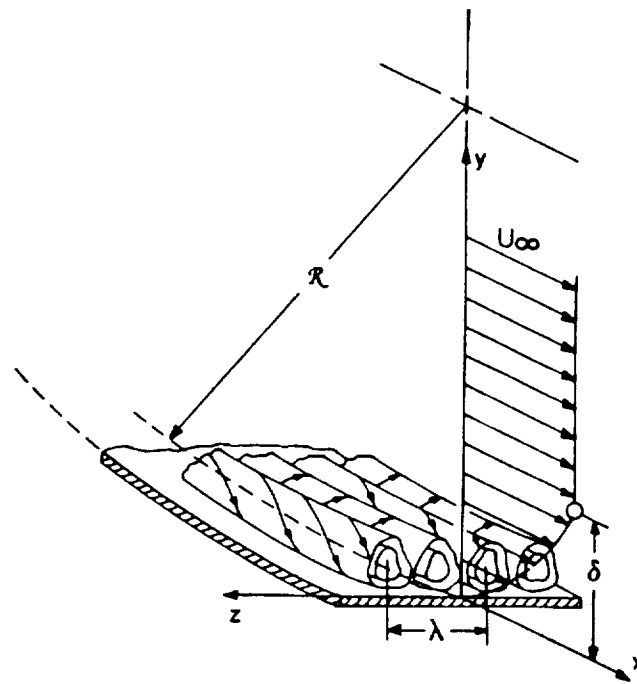
Figure 1 - Görtler Vortices within a Boundary-Layer Flow over a Concave Wall [24]

nozzle to bring the flow from the settling chamber to the nozzle throat. However, any instabilities generated in this region can be sucked away by the use of bleed slots just downstream of the inflection point.

Since it has been shown that boundary-layer transition on the walls of most quiet-tunnel nozzles is due to the Görtler instability rather than Tollmien-Schlichting waves [11], the main goal in new nozzle designs is to delay and limit the growth of the Görtler vortices as was discussed in the section on quiet-tunnels. A straight wall section, inclined at the maximum wall angle, is included in new designs for this purpose.

1.3.3 Surface Roughness

Experimental and computational data analyzing the effect of wall roughness on transition is presently lacking [14]. Therefore, it is difficult to determine exactly how

disturbances created by machining imperfections will affect boundary-layer stability. Beckwith, Malik, and Chen [11] have provided, however, a limited set of data for experiments in the NASA Langley Mach 3.5 Supersonic Low-Disturbance Pilot Tunnel with the tunnel walls "clean", "repolished", and "dirty". The "clean" condition corresponded to the nozzle being wiped with a lint-free cloth dampened with alcohol followed by vacuuming to remove atmospheric dust and lint. The "repolished" condition contained a significant reduction in the rms and peak-to-valley profilometer readings due to the polishing. Finally, the "dirty" condition occurred when there was a visible build-up of lint, dust, and other contaminants before a run. Conclusions from these runs showed that the repolishing operation resulted in a significant increase in laminar flow in the wall boundary-layer. Therefore, walls with small machining tolerances, and frequent cleaning and polishing seem necessary for quiet-tunnel operation.

As a compromise between performance and machining capabilities in more recent quiet-flow tunnels, finish tolerances at the throat with maximum deviations in the range of 2 microinch rms have typically been specified.

1.3.4 Corner Flow

Corner flow is a complex three-dimensional flow formed by two intersecting surfaces. The three-dimensionality is enhanced by the presence of crossflow along the walls that transport mass, momentum, and energy into and out of the corner region [25]. It has been shown that two counter-rotating vortices centered about the corner bisector are also present in laminar supersonic flow through a duct with a mild adverse pressure gradient [26]. Clearly, the different factors that contribute to corner flow make determining the flow stability a difficult problem.

The boundary-layer in a streamwise corner has been investigated. Recent examples of these studies are given in references [25-28]. The only known experimental study of transition in a corner flow with a favorable pressure gradient is that of Misu as reported by Beckwith [29]. It was shown that reverse transition in the corner of a rectangular shaped contraction occurred at about the same streamwise location as on the walls. Following these results, it would seem reasonable to expect a similar result for transition in square nozzles since they also contain favorable pressure gradients. Although experiments by Zamir [30] were conducted close to zero

streamwise pressure gradient, he concluded that for Reynolds numbers greater than 10^4, the corner boundary-layer is only stable with some favorable streamwise pressure gradient. Again, it is hoped that the favorable pressure gradient which exists in square nozzles will be helpful in preventing transition in the corners.

Pfenninger and Syberg [31] have found that premature transition in the corner boundary-layer at the juncture of aircraft components can be prevented by suction. This result has been verified experimentally by Goldsmith (cited in reference 29). These results suggest that suction at the corners of the square nozzles could be used if required.

1.3.5 Crossflow

Various fluid flows occur in a way that creates a pressure gradient normal to the mean flow direction near a body. This pressure gradient will cause the development of a velocity component inside the boundary-layer that is perpendicular to the local inviscid flow and parallel to the wall. This is known as crossflow. Such applications consist of but are not limited to: flow over swept wings, flow on rotating disks and rotating axisymmetric bodies, flow in corners, and attachment-line flows. The crossflow profile is defined by a maximum somewhere in the middle of the boundary-layer and goes to zero at the boundary-layer edge and at the wall. A schematic of a three-dimensional boundary-layer profile along with the streamwise and crossflow components is shown in figure 2 [32]. The crossflow profile contains an inflection point which is known to be dynamically unstable. This instability often leads to the formation of corotating vortices, which can be stationary or traveling crossflow disturbances.

Two and three-dimensional nozzles exhibit a transverse pressure gradient due to the uneven expansion along the walls. This gradient will cause crossflow in the boundary-layers of these nozzles. Since crossflow is poorly understood for nozzle flows, a thorough investigation of nozzle wall boundary-layer stability in the presence of crossflow must be completed before three-dimensional nozzles will be proven useful for quiet-tunnel designs.

The phenomena of crossflow and its effects on transition has been studied extensively, and comprehensive reviews are given in references [32-37]. Since a vast amount of material exists on the subject, only material relevant to this research will be
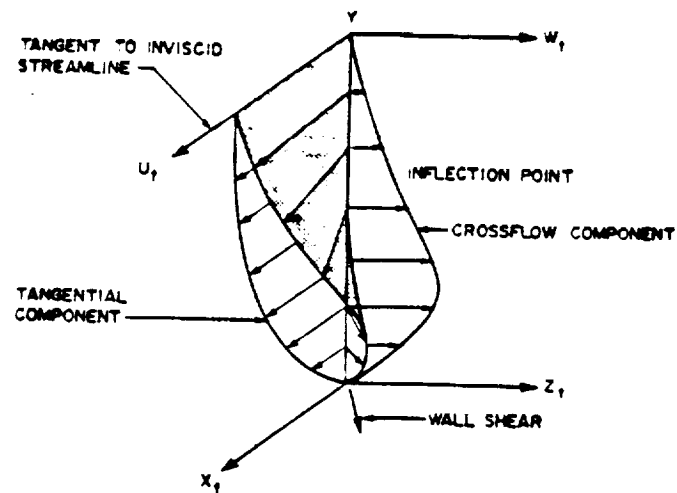
Figure 2 - Velocity Components within a Three-Dimensional Boundary-Layer [32]

covered. First, a discussion of the crossflow Reynolds number and its use in estimating transition is presented. Then some basic fundamentals of crossflow in subsonic and supersonic flow will be discussed.

1.3.5.1 Crossflow Reynolds Number

The earliest attempt to evaluate boundary-layer stability and transition in the presence of crossflow was through the development of the crossflow Reynolds number. The equation for this is shown below:

$$R_{cf} = \frac{W_{MAX}\delta_{10}}{v_e} \tag{2}$$

where (see figure 3) [38]

W_{MAX}	Maximum crossflow velocity
δ_{10}	Maximum distance from wall where crossflow is 10% of W_{MAX}
v_e	Kinematic viscosity at edge of boundary-layer
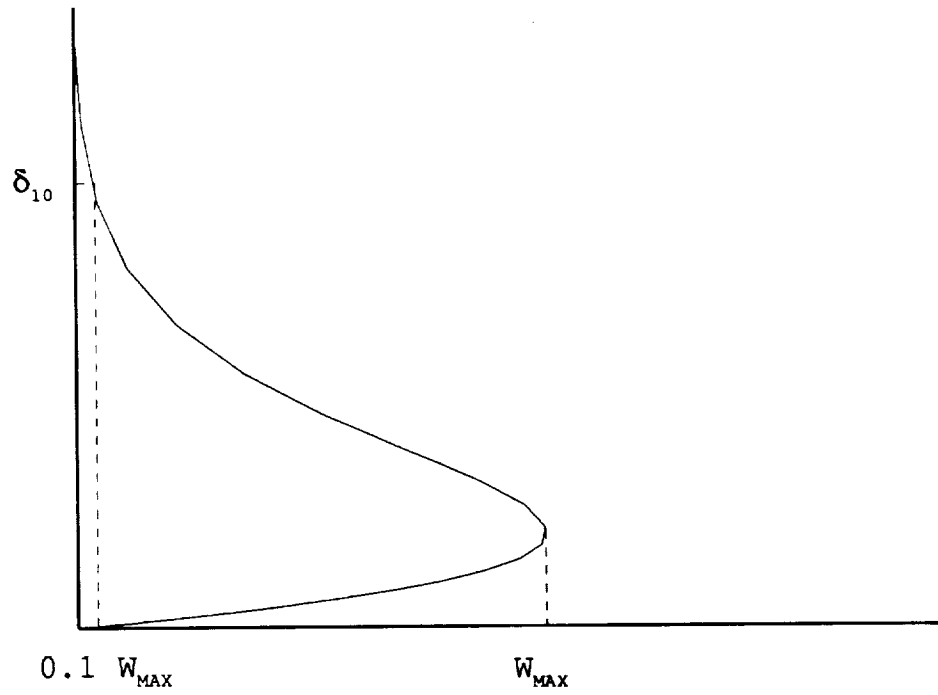
Figure 3 - Definition of Variables for Calculation of Crossflow Reynolds Number

Even though linear stability analysis is the technique recommended for determining transition location, there is still a desire to have parameters based purely on basic-state profiles which can be correlated to transition location. These parameters can then easily be incorporated into existing programs and would require much less time and computing effort than e^N methods to find the location of crossflow dominated transition. For this reason, crossflow Reynolds number techniques for estimating transition location are still used for preliminary design purposes.

The introduction of the crossflow Reynolds number is credited to Owen and Randall [32 and 39]. They also suggested that transition occurs when the crossflow Reynolds number becomes on the order of 150 as observed in two-dimensional wing experiments at different sweep angles (Poll [37] discusses the details of this correlation). Further review by Poll shows that although initial experiments agreed with this correlation fairly well, experiments by Boltz, Kenyon, and Allen using a different wing section but the same sweep angles gave a transition Reynolds number from 200 to 250. Finally, Poll states that experimental investigations of flow over a rotating disc found a transition crossflow Reynolds number of 680, significantly different than on swept wings.

Various applications of the crossflow Reynolds number have been attempted to find a method for estimating the transition location which works for many different cases. Beasley, as cited by Arnal [34, 36], defined a new crossflow Reynolds number based on an integral of the crossflow profile. This definition of the crossflow Reynolds number is shown in equation 3 below:

$$R_{\delta 2} = \frac{1}{v_e} \int_0^{\eta_e} w \, dy \qquad (3)$$

where

v_e Kinematic viscosity at edge of boundary-layer

η_e Distance to the boundary-layer edge along the wall normal

w Crossflow velocity

Using experimental data, it was suggested that transition would generally occur when this parameter reached 150. However, as shown before and noted by Arnal [36] and Poll [37], the use of a single parameter to estimate transition cannot be good for all situations. For this reason, Arnal and Coustols [34, 36] developed two criteria, C1 and
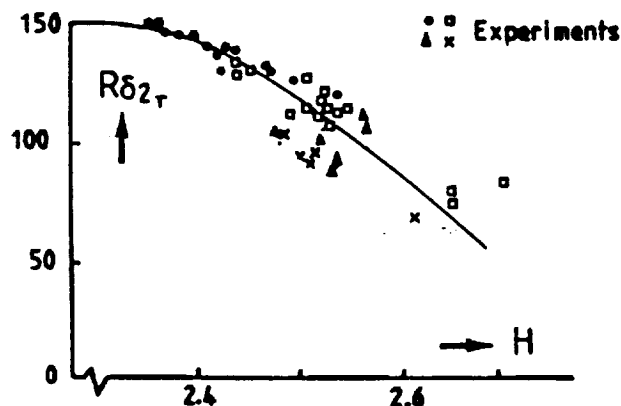
Figure 4 - C1 Crossflow Criterion [34]

C2, which they felt could more accurately estimate transition. The first method, C1, is based on Beasley's crossflow Reynolds number and the streamwise shape factor. A curve fit of experimental data was used to give a transition crossflow Reynolds number for various streamwise shape factors. This is shown in figure 4. Although some scatter of data still exists in this correlation, it appears to be much better than assuming that transition occurs at a constant value of the crossflow Reynolds number.

The second method, C2, was developed in an attempt to reduce the scatter seen in the C1 criterion. This method is based on results from linear stability theory instead of a fully empirical development. Here, each disturbance angle is checked from $0°$ (fully streamwise profile) to $90°$ (fully crossflow profile). Then the critical Reynolds number can be found and checked against the streamwise shape factor and the freestream turbulence level to determine if transition has occurred. Although this method is based on linear stability theory, the authors admit that calculations to find the critical Reynolds number are long and costly, and not as accurate as e^N. This deters its use for initial design estimations.

Reed and Haynes [39] discovered that a single value for the crossflow Reynolds number does not correlate with transition in the supersonic regime either. Initially, they found that Chapman and Pate had concluded that the crossflow Reynolds number correlated well with the location of transition. Experiments by King on a yawed cone,

however, showed that the crossflow Reynolds number did not correlate with transition location. By completing calculations on rotating cones at various conditions, Reed and Haynes were then able to show that the crossflow Reynolds number at transition varied from 250 to 450, much different than the 150 observed in the subsonic regime.

After showing the wide scatter in the crossflow Reynolds number for yawed and spinning cones, Reed and Haynes [39] presented a new crossflow Reynolds number, shown in equation 4, that included corrections for both compressibility and wall cooling.

$$R_{cfR\&H} = \frac{W_{MAX}\delta_{10}}{\nu_e} HL \tag{4}$$

The equations for the compressibility correction, H, and the wall cooling, L, are given in equations 32-34 in chapter 2.2.3. Calculating this new crossflow Reynolds number from their numerical data on spinning cones, two points were established. First, their computed incompressible value fell among the compressible values. Second, a relationship seemed to exist between the new crossflow Reynolds number and the maximum crossflow velocity. Checking this new crossflow Reynolds number on the experimental data of King, two more important points were noted. First, it appeared they could estimate transition by dividing the new crossflow Reynolds number by the maximum crossflow velocity over the edge velocity (W_{MAX}/U_e) in percentages. This gave a constant value at transition of 44.0 for quiet flows and 33.7 for noisy flows. Secondly, they noted that the values of the new crossflow Reynolds number were in the neighborhood of 150 when W_{MAX}/U_e was on the order of 3% which was consistent with the results of Owen and Randall.

Godil and Bertelrud [40] also noted that although the crossflow Reynolds number at transition is on the order of 200 in subsonic flows, the transition crossflow Reynolds number increased with Mach number as was shown by results from linear stability theory. Using these results, transition was then estimated from the standard crossflow Reynolds number with a correction for compressibility. Checking the results presented for both the corrected crossflow Reynolds number and linear stability theory on a biconvex wing at Mach 6, the new crossflow Reynolds seemed to estimate transition close to where it is predicted by linear stability theory (N = 9 for transition).

1.3.5.2 Crossflow in the Subsonic Regime

Crossflow and its effects on transition have been studied extensively in subsonic flows, especially over wings, for laminar flow control design. On swept wings, a chordwise pressure gradient near the leading edge is the cause for the development of crossflow. Experiments by Dagenhart [41] on a 45° swept wing showed the existence of both stationary and traveling crossflow waves. Linear stability predicted the traveling wave frequencies accurately but stability results were about 30 percent larger than the observed stationary frequencies. Further work by Radeztsky, Reibert, and Saric [42] showed that linear theory does accurately predict mode shapes and expected wavelengths for stationary crossflow vortices. However, linear theory does not accurately predict the growth rates for low-amplitude waves. They report that this is a further extension of the experiments of Bippes and Dagenhart that showed the failure of linear theory for very large crossflow vortices. Finally, Dagenhart [38] concluded that crossflow disturbance amplification rates are proportional to the maximum crossflow velocity when all other factors are held constant.

Analysis of flight measured data by linear stability theory [43] applied the theory of separation of transition mechanisms, the study of two or more disturbances which occur simultaneously but are assumed to act individually in causing the boundary-layer to become unstable, and found reasonable agreement with data from other experiments. Pfenninger [44] noted that this separation into independent parts is physically acceptable as long as strongly amplified crossflow and Tollmien-Schlichting waves do not occur simultaneously. In another attempt to study non-linear disturbances, Malik, Li, and Chang [45] completed a numerical study of the flow over a swept cylinder. The interaction studied was between traveling and stationary crossflow vortices. They conclude that when the disturbance amplitude reaches about 4 percent, the stationary and traveling modes begin to depart from their linear values. Another important conclusion from this work is that although the initial amplitude of the stationary vortex was much larger than the traveling modes, as the flow moves downstream, the traveling mode becomes the same order of magnitude as the stationary mode.

Another type of flow that has been considered is flow over a rotating disk. In this problem, flow moves axially toward the disk and as the three-dimensional boundary-layer builds on the surface, the fluid is cast off the edge like a centrifugal pump. This causes a stationary crossflow instability on the disk which spirals outward. A compilation of data has shown that traveling waves have a higher amplification rate

than stationary waves according to theory [32]. The importance of secondary instabilities still remains unclear for this problem (see reference 33 for a discussion of the effects of secondary instabilities in crossflow induced transition).

1.3.5.3 Crossflow in the Supersonic Regime

Few numerical or experimental results have been obtained for crossflow in the compressible regime. Although Wang, Herbert, and Stucker [46] have completed some Parabolized Stability Equations calculations for a compressible swept wing flow, they "...have not pursued this supersonic case because data for comparison are lacking." Dagenhart [38] suggests that it seems that incompressible flow theory as it relates to crossflow is a physically reasonable approximation although it is somewhat conservative. Finally, Arnal [34] states that the crossflow instability is dominated by the inflection point properties which are not affected by compressibility very much. For this reason, he also believes that incompressible criteria can be used to estimate transition in the compressible region.

Numerical investigations of crossflow over various bodies at supersonic and hypersonic speeds showed, however, that transition in these flows does not agree with the predicted location using the crossflow Reynolds number. Reed and Haynes [39] show that the standard crossflow Reynolds number has a spread on the order of 200% for their calculations of flow over a rotating cone. They also show that the experimental results of King for flow over a yawed cone give even larger spreads than they observed for spinning cones. Finally, Godil and Bertelrud [40] stated that the transition crossflow Reynolds number increases with Mach number which was verified by the use of linear stability analysis.

Supersonic flow inside a square or rectangular duct has been investigated by various researchers. Numerical results from Davis, Gessner, and Kerlick [26] of laminar flow through a square duct with a mild adverse pressure gradient show the development of two counter-rotating vortices around the corner bisector. They find that this secondary flow causes a bulging of the total pressure contours in the corner region, a characteristic that is distinctly different from crossflow investigated in an unbounded corner problem. Numerical investigations of compressible turbulent flow through a square duct [25] showed similar total pressure contours and crossflow profiles to those measured in incompressible square duct flow at approximately the same streamwise

location. A numerical investigation of turbulent flow in square Mach 4.7 and Mach 6 nozzles [47] showed some interesting flow phenomena that could also be expected in slow-expansion nozzles. Both nozzles showed the development of counter-rotating vortices in the corners that were then shed to the centerline. At the exit, these vortices were greater than 30 percent of the spanwise length of the wall. However, it is stated that agreement is not very good compared with experimental data close to the wall. Mach number contours at the exit also show small structures near the corner that are not discussed in the paper. This is probably the same type of structures shown by other investigators in corner regions.

Comparisons of predictions and experiments for a Mach 3 two-dimensional nozzle [17] showed the development of crossflow along the nozzle walls. However, in this investigation, the crossflow originated at the center of the contoured wall and moved toward the corner and then down the sidewall. This created one vortex in the corner instead of the counter-rotating vortices observed in square ducts or unbounded corner problems. Another important conclusion in this work is that the calculated Görtler instability was insufficient to cause transition, and the observed crossflow could have contributed to the transition process. No details were provided for the affect of crossflow on transition, however.

Experiments have also been performed on swept cylinders at Mach 10 [48]. The results showed that although no transition occurred, streaks generated by the crossflow instability were seen. Linear stability analysis applied to the flow provided two significant conclusions. First, increasing the wall temperature seemed to have a destabilizing effect on the stationary crossflow disturbance. Second, the maximum N factor calculated was less than 2. This shows that no transition should have occurred, verifying experimental results.

Clearly, more work needs to be done in this area for a complete understanding of crossflow-induced instability and transition in high-speed applications.

1.4 Objectives

The objective of this research is to numerically study crossflow in two Mach 2.4 square nozzle designs to estimate the boundary-layer stability. Specifically, a short and a long Mach 2.4 nozzle will be studied to determine if length has an effect on crossflow stability. The initial design for a Mach 8 nozzle is also presented as an initial step

towards examining the effects of Mach number on crossflow. To get a general idea of crossflow instability and transition, three crossflow Reynolds numbers will be calculated and simple transition estimators using these parameters will be studied. These are: 1) The standard crossflow Reynolds number with the transition estimator given by Godil and Bertelrud [40], 2) The new crossflow Reynolds number presented by Reed and Haynes [39], 3) The crossflow Reynolds number of Beasley [34, 36] with transition estimated using the C1 criteria of Arnal and Coustols [34, 36]. Although the crossflow Reynolds number is a technique with limited accuracy, alternate techniques such as e^N or the Parabolized Stability Equations require far more resources than are available at this initial point in the design phase. It should also be noted that no data exists, to the authors knowledge, for crossflow-induced transition on nozzle wall boundary-layers with which these more accurate techniques can be evaluated. Therefore, the crossflow Reynolds numbers are used as an initial attempt to discover how crossflow will affect the boundary-layer.

The nozzles for this study are designed using previously developed design techniques that have been found to limit certain disturbance amplifications. As discussed earlier, slow-expansion nozzles have been shown to limit the growth of Taylor-Görtler vortices while not significantly enhancing Tollmien-Schlichting waves. Therefore, this design will follow previous work and use a large radius of curvature at the throat, a small expansion angle, and a long radial flow region. It will then be assumed that neither of these disturbances becomes large enough to cause transition. Further investigation of these disturbances must be completed in the future for a full understanding of the overall boundary-layer stability.

The subsonic portion of the nozzle must also be dealt with to insure a laminar boundary-layer upstream of the throat. To accomplish this, a bleed slot will be inserted in the nozzle downstream of the subsonic wall inflection point [8]. The purpose of this slot is to remove the contraction-wall boundary-layer and create a new laminar layer starting on the slot lip. The slot will not be considered in this portion of the research, so the upstream boundary in these calculations will be taken where the slot lip would begin for each nozzle.

Although no design procedures exist for corner flows, this issue still must be addressed for a complete picture of the problem. It has been shown that transition in the corner occurs at roughly the same streamwise location as on the walls [29]. Other results suggest that suction could be used to limit transition in the corner regions if necessary. Therefore, stability of the corner flow will not be considered here.

CHAPTER II   NUMERICAL SIMULATION TECHNIQUE

Various computer programs for the design of the nozzles, the numerical simulation, and the data post-processing were either implemented or developed. A discussion of these programs and the design procedures used follows.

2.1 Nozzle Development

Since most wind tunnel nozzles in use are two-dimensional or axisymmetric, few design methods exist for three-dimensional nozzles. Beckwith, Ridyard, and Cromer [49] developed a method for designing a three-dimensional nozzle using an axisymmetric flow field. In this procedure, an axisymmetric design is calculated by the method of characteristics in the supersonic region. A cross-sectional shape is then selected at the exit and the streamlines passing through the exit shape are tracked upstream. This provides a three-dimensional nozzle with an arbitrary cross-section.

In quiet-flow nozzles, the three-dimensional contour is required starting from the bleed-slot lip. Therefore, the contour must also be found in the transonic region of the nozzle. Using a series solution developed by Hopkins and Hill [50], an axisymmetric wall contour can be developed for the transonic region of the nozzle. The streamline traces from the supersonic portion of the nozzle can then be continued into the transonic region, completing the nozzle contour.

If this method is applied to a nozzle with a square test section, the cross-sections will only be square at the exit and at the throat if the flow is parallel and uniform. All other cross-sections will "bowed" in or out between the corners. This will be discussed in further detail in subsequent sections. A correction can be made by assuming a constant area and then each cross-section can be "squared-off". This approximation has been used for the 31-Inch Mach 10 Wind Tunnel and two lower Mach number scramjet testing nozzles at NASA Langley as reported by Beckwith [29]. A boundary-layer

correction is also included in the design of these nozzles. This consists of the addition of the local boundary-layer displacement thickness to the inviscid contour. The boundary-layer thickness is computed using a two-dimensional method with the centerplane pressure distribution. Flow surveys in the Mach 10 nozzle have shown that the flow uniformity is excellent. This indicates that the assumptions used in the design were satisfactory.

The subsequent sections discuss the application of this method for the design of both Mach 2.4 nozzles and the preliminary Mach 8 design.

2.1.1 Wall Contour Design

The inviscid design for the wall contour is performed using the method of characteristics technique developed by Sivells [51] in the supersonic region, and the method of Hopkins and Hill [50] in the transonic region. A brief description of the codes used in this stage of the design follows.

The beginning of any nozzle designed using this method is in the transonic region. The method developed by Hopkins and Hill uses an inverse solution to find the body geometry given a velocity distribution along the axis. Assuming steady, irrotational, adiabatic, shock-free flow of a perfect gas with constant specific heats, two differential equations that satisfy continuity and irrotationality were found using asymptotic methods. The equations were then transformed to use the velocity potential and the stream function as the independent variables. The dependent variables were then expressed in terms of a power series with the accuracy dependent on its order. These equations can then be solved point-by-point as long as the Mach number distribution is specified along the nozzle axis. A code was written [52] to solve these equations developed by Hopkins and Hill. This code is described below.

First, the streamline that corresponded to the wall contour needed to be determined. Since the equations were normalized with respect to the throat radius, the streamline that had a minimum at $y = 1.0$ corresponded to the wall contour. This streamline was found by using an iteration process, over Hopkins and Hill's variable ξ, to find the location where $dy/dx = 0$ when $y = 1.0$.

The Mach number distribution along the axis could then be specified as long as the initial and final Mach numbers were known. These values were initially arbitrary and therefore a method was developed to find them. The starting location was taken

where the angle of the wall contour streamline was the same as the approach angle, θ_a. This location was chosen since it corresponds to the inflection point of the wall in the subsonic region. The location is, therefore, assumed to be the preliminary location of the bleed slot in these designs. The starting location was found by solving for the flow angle, as the dependent variable, using a bisection method, until the angle θ_a was found. The corresponding Mach number on the reference line was then used as the initial Mach number for the calculation. The final location was taken at the throat, where $x = 0$, so that the code could easily be patched with the method of characteristics code. This location was also found by solving for the dependent variable x using a bisection iteration method. After this location was found, the corresponding Mach number on the reference line was set as the final Mach number.

The supersonic region was started at the end of the transonic flow solution, slightly downstream of the sonic line. Starting from this point, a characteristic net is developed up to the characteristic that defines the beginning of the radial flow region. The radial flow region is then patched to the solution with the requirement that the first and second derivatives of the Mach number on the centerline be continuous. Finally, the rest of the nozzle was calculated using the method of characteristics beginning at the characteristic that marks the end of the radial flow region. A fourth order polynomial is fit between M_B and M_C to assure a smooth wall contour. The coordinates of the wall were determined by integrating the mass flow rate along the characteristic lines to satisfy the conservation of mass principle.

After the solution to the flowfield was found, a square cross-section is defined in the exit plane and the corresponding streamlines are tracked upstream. Since the entire flow solution is known in the supersonic region, each of the desired streamlines could be found by its corresponding inflection angle. The limits of the streamlines were θ_w and $\theta_w / \sqrt{2.0}$ corresponding to the cornerplane and centerplane of the square contour. However, in the transonic region, each of the desired streamlines must be found as if it were considered to be the wall. Therefore, the streamlines from where $y = 1 / \sqrt{2.0}$ (corresponding to the square nozzle wall in the centerplane [see figure 5]) to when $y = 1.0$ must be determined. This gives all the streamlines for the square nozzle contour. The streamlines from the Hopkins and Hill formulation in the transonic region are matched to the streamlines produced by Sivell's code, at the streamwise location of the throat ($x=0$). It is important to note that although Sivell's code uses a different asymptotic formulation for the transonic region, the two formulations match smoothly at the throat where they are patched together. This is not surprising since both
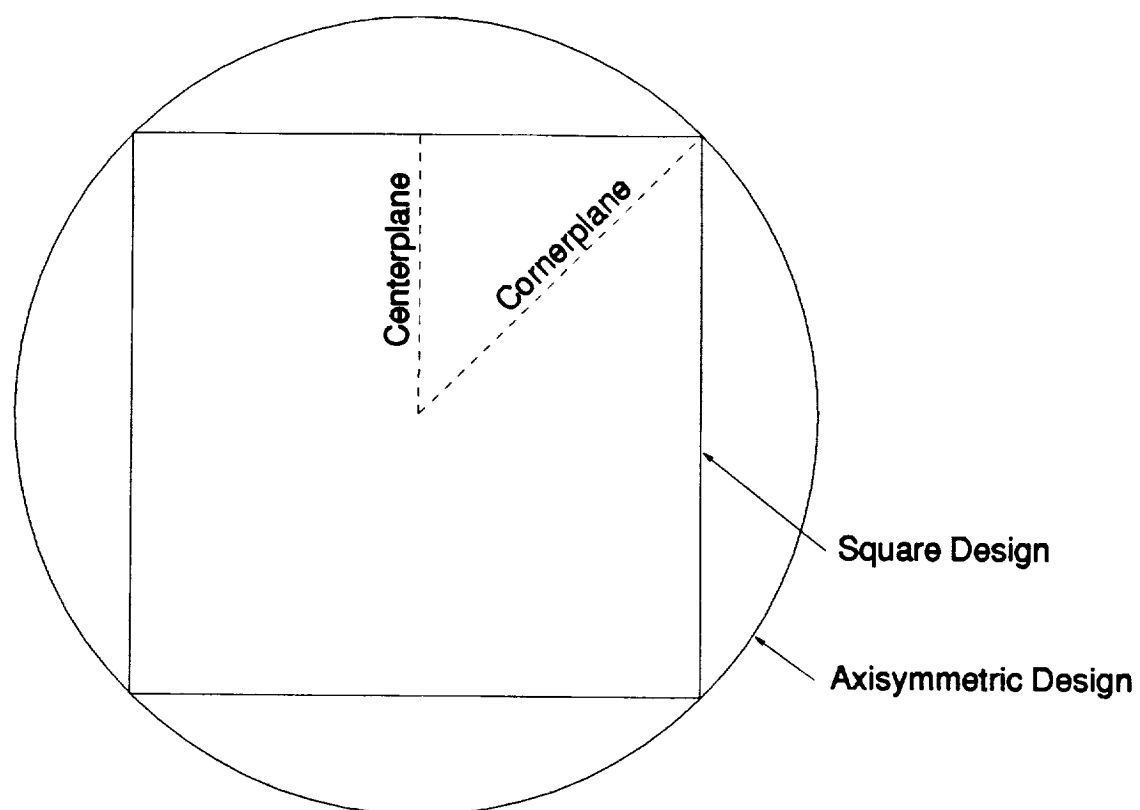
Figure 5-Geometry Definition

formulations are asymptotic solutions valid near the throat.

The first phase in developing the desired nozzles was to obtain an axisymmetric contour. The data required for this were the radius of curvature at the throat (R_a), the approach angle (θ_a), the expansion angle (θ_w), the Mach number along the centerline at the end of the radial flow region (M_B), and the exit Mach number (M_C). To keep the Görtler instability as small as possible, a large radius of curvature, small expansion angle, and long radial flow region are necessary. These are reflected in the design parameters given in table 1. Note the radius of curvature at the throat is non-dimensionalized with respect to the throat radius, so this value is dimensionless.

Nozzle 1 is the first axisymmetric design and is referred to as the short Mach 2.4 design from here on. The second Mach 2.4 nozzle (nozzle 2 in table 1, and referred to as the long Mach 2.4 nozzle) was designed using a smaller expansion angle, a smaller approach angle, and a larger radius of curvature. The design of the Mach 8 nozzle (nozzle 3 in table 1) was selected to match the size of the Mach 8 Variable Density Tunnel (M8VDT) [10] as closely as possible.

Table #1 -Nozzle Design Parameters

Nozzle	R_a	θ_a	θ_w	M_B	M_C	P_0 (psia)	T_0 (^{o}R)	R_∞ (ft^{-1})	r_{th} (in)
1	5.5	42.42^o	5.44^o	2.39	2.4	100	540	3.182 x 10^7	3.65
2	6.22	35.36^o	2.83^o	2.39	2.4	100	540	3.182 x 10^7	3.65
3	3.3	30.0^o	6.50^o	7.75	8.0	1000	1380	9.764 x 10^7	0.525

Note that the parameters R_a, θ_a, and θ_w are along the diagonal of the square nozzle which corresponds to the radius of the axisymmetric design (see figure 5). To find the parameters along the centerplane for any wall of the square nozzle, those given above must be divided by the square root of two.

The parameters R_a, θ_a, θ_w, M_B, and M_C are entered into the program, described above, that uses Sivells implementation of the method of characteristics for axisymmetric inviscid nozzle design with the method of Hopkins and Hill for the transonic portion. The streamlines corresponding to a square in the exit plane were written to a file for post-processing to develop the final three-dimensional contour.

Once all the streamlines required from the axisymmetric contour were known, the final square contour can be completed. Full descriptions of the programs used can be found in references 52 and 53. A program named SNODEC [53] was developed by Michael Moen as a post-processing code for the development of square nozzles from axisymmetric designs. This code reads in the streamline data and creates the final square contour. While reading the data, the code asks for the number of planes downstream of the throat that are desired. The documentation suggests that no more than 200 planes be taken so as not to exceed the limits of the interpolation routine. However, the number of planes chosen should be the same order of magnitude as the number of grid points in the streamwise direction to maintain accuracy in the grid generation program. Therefore, 200 planes are chosen for all cases examined. Since the finest grid examined only has 305 points in the streamwise direction, 200 planes should be adequate for the interpolation routine. After the streamlines are read in and the data is interpolated to uniform stations, the square contour can be generated. Some bowing will occur in each cross-section except at the exit and at the throat, if the flow is parallel, during this procedure. Figure 6 shows the difference in the z-coordinate between the corner and center through the short Mach 2.4 nozzle. If the difference in the z-coordinate between the corner and the center were zero, the cross-section would be a square with a height of z. However, some bowing can be seen both inward and outward. This is caused by the streamlines not being parallel at every location. This bowing creates a contour that is not completely square. To square the cross-sections, a numerical integration is completed at every streamwise location to find the area and then the square root of the area is taken to obtain the square height.

The nozzle contour is then completed by the calculation and addition of a boundary-layer correction. This correction is made by the addition of the displacement thickness calculated assuming a two-dimensional flow along the nozzle centerplane. Specifying the pressure distribution, calculated in the SNODEC code, and the wall coordinates, a program written by Harris and Blanchard [54] for solving two-dimensional and axisymmetric boundary-layers was used. Also necessary are the throat radius, Prandtl number, stagnation pressure, stagnation temperature, and universal gas
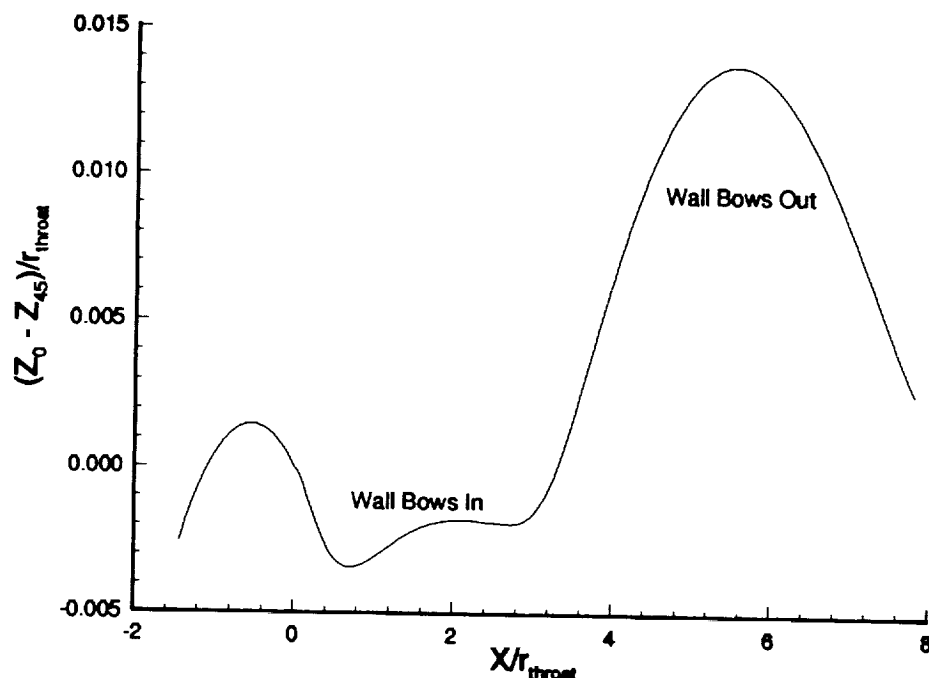
Figure 6-Wall Bowing Due to Streamline Tracking of the Square Geometry

constant. Given this data, the displacement thickness is calculated and then added to the inviscid contour by use of the SNODEC code. The SNODEC code is also used to calculate the pressure gradient between the corner and centerplane which will be compared to the results from the Navier-Stokes solutions. The final nozzle contour is given in terms of feet.

The techniques described were then used to create the square contours for the two Mach 2.4 nozzles and the Mach 8 nozzle. The stagnation pressure, stagnation temperature, and throat radius are also shown in table 1 for each nozzle. To account for the location of the bleed-slot in these nozzles, they are cut-off at an approximate Mach number of 0.5 as an initial estimation. The final three-dimensional outline for the short Mach 2.4 nozzle is shown in figure 7, the Mach 2.4 long nozzle in figure 8, and the Mach 8 nozzle in figure 9. All of the units have been converted to inches in these figures. As was stated, the Mach 8 nozzle was designed to match the operating parameters of the M8VDT as closely as possible. The overall length of the nozzle using these design parameters is approximately 1.75" shorter than the M8VDT and the distance along the diagonal at the exit is 0.047" larger. Although a grid was generated
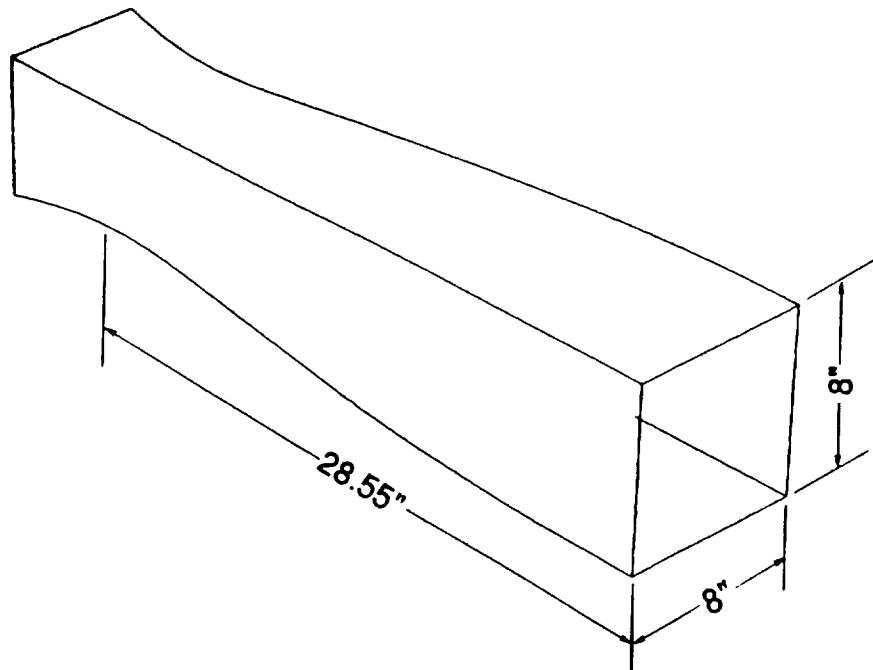
Figure 7-Short Mach 2.4 Nozzle Contour
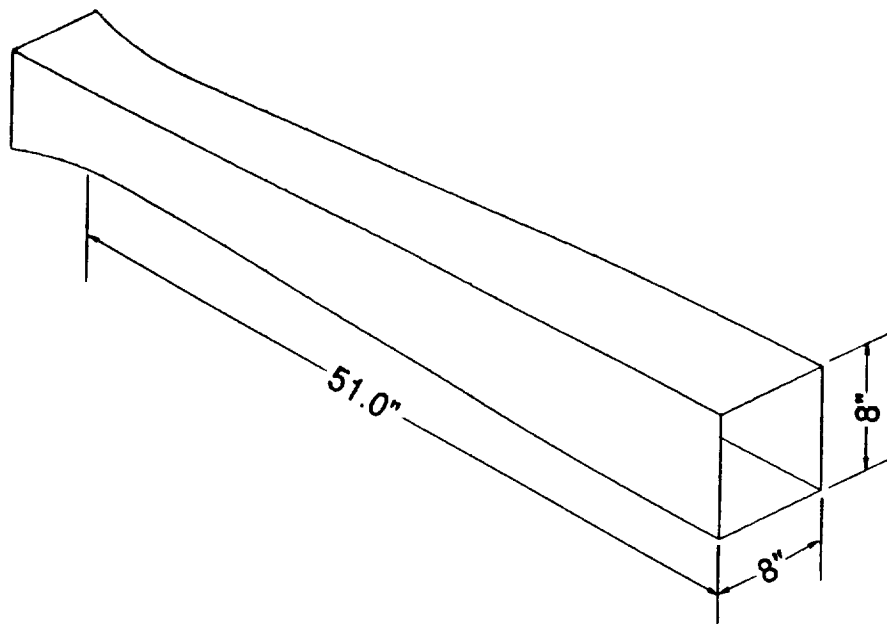
Figure 8-Long Mach 2.4 Nozzle Contour
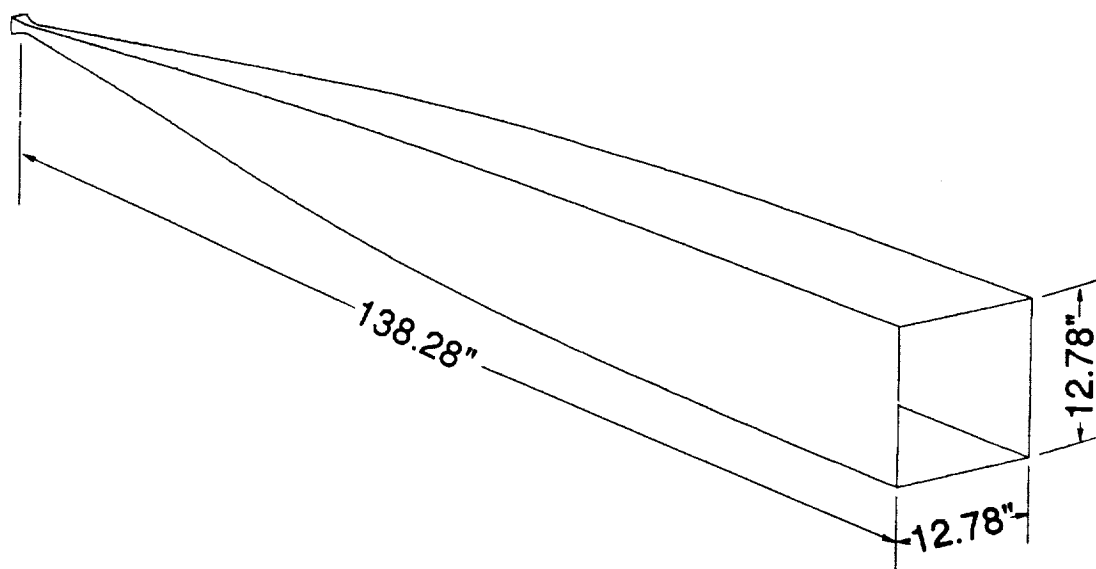
Figure 9-Mach 8 Nozzle Contour

for the Mach 8 nozzle, simulations were not completed on this nozzle. Further investigations will be completed on this design at a later time.

2.1.2 Grid Generation

The grid used in all nozzles is a simple body fitted grid with constant spacing in the streamwise direction and stretching in the normal directions. Two programs were written to generate the grids. They are listed in appendix A.

The first of these two programs takes the final square contour from the *.csd file generated by the SNODEC code. The structure for the *.csd file is shown in appendix A. The purpose of this program is to read in the contour from this file, convert it to metric units, and then write the coordinates in a generalized form. This form is: the x location, the minimum and maximum y values, and the minimum and maximum z values. Also written at the top of the data file are the minimum and maximum x values, to set the grid spacing in the next program. One important note, a number 1 must be

added to the bottom of the *.csd file to signify to this program that the data set is complete.

The second program is used to generate the grid for the Navier-Stokes calculation. First, the data set that was created by the first program is read. Then the user is prompted for the stretching constant which controls the stretching near the wall. The choices for the stretching variable will be described later. Finally, the program asks the user if Tecplot [55] data is desired. The data generated for use in Tecplot consists of three files. The first file contains cross-sectional data at various constant x locations, the second contains a plane where y is the maximum value, also a wall contour, and the third contains a plane where z is zero, also a centerplane. These can be used to evaluate the grid without the unnecessary work of converting the full binary file.

The grid dimensions are then set in the IMAX, JMAX, and KMAX variables. Next are constants defined for the grid stretching. These variables are set in the program since they remain constant for most cases. The variable XBAR can be set between zero and one and determines the weight of stretching near the wall versus the amount of stretching near the centerline. For these grids, this variable is chosen to be zero so all the stretching is near the wall. The variable EX is an exponential that limits how the centerline stretching affects points near the wall and how the wall stretching affects points near the centerline. However, when XBAR is zero, this parameter plays no role in the calculation. Variable SFACTC is the stretching variable for the grid near the centerline. This also plays no role in the calculation when XBAR is zero. This stretching function was originally developed by Dr. John Korte at NASA Langley and has been adapted for use in this code.

An interpolation routine is set up so that no matter how many points are in the input file, an even spacing of points in the streamwise direction is developed. For this, a linear interpolation is used between points in the input file if necessary. Therefore, the number of points used to generate the *.csd file in SNODEC should be approximately the same number of points used in the grid in the streamwise direction. Finally, all of the points are calculated and written to a binary file that can be read by the Navier-Stokes solver. A listing of both of these codes as well as the file generated by the first code for the Mach 2.4 nozzle is given in appendix A.

Since the flow is symmetric about any centerplane in the nozzle, the solution only needs to be calculated in one quadrant. Four calculations have been completed on the two Mach 2.4 nozzles. Three were done on the short Mach 2.4 nozzle as a grid resolution study. The grids used were 137x41x41, 201x65x65, and 305x97x97

corresponding to 2/3 and 3/2 of the medium grid. These grids were chosen to be multigridable up to at least four levels. The stretching constant was defined for these grids to be 1.00005. This was found by developing numerous grids using the medium resolution case to find a stretching parameter that would place approximately 20 points in the boundary-layer at the exit. The boundary-layer thickness was taken from the results from the Harris and Blanchard boundary-layer code. Then the same stretching was used on the coarse grid. The stretching was also attempted on the fine grid, but the high aspect ratios generated using this stretching caused too much artificial dissipation in the Navier-Stokes solver and the code would not converge. To correct this, a slightly larger stretching factor of 1.0005 was used for the fine grid. Further studies of this grid showed that the ratio of points in the boundary-layer was still approximately 3:2 between the high resolution and medium resolution cases.

The results from the grid resolution study have shown that the medium resolution grid is adequate for the crossflow Reynolds number techniques used. For this reason, the medium grid is also used on the Mach 2.4 long nozzle. Since the exit dimensions are the same, the medium resolution grid with a stretching factor of 1.00005 was adequate to resolve the boundary-layer properties. The problem with using this grid is since the long nozzle is almost twice as long as the short nozzle, the spacing in the streamwise direction becomes almost twice as large in the long nozzle. However, it will be shown that this should be adequate to resolve the flow.

2.2 Numerical Solution and Crossflow Calculation

The purpose of this section is to describe the techniques used by the three-dimensional Navier-Stokes solver and the data post-processing program. Documentation for the Navier-Stokes solver, LARCK (Langley Algorithm for Research in Chemical Kinetics) [56], is not yet available since the code is still under development at NASA Langley. Only the portions necessary for this problem are described.

2.2.1 Governing Equations

The equations to be solved for all of the nozzles considered are the full three-dimensional compressible Navier-Stokes equations. These are written in non-

dimensional form below

$$\frac{\partial U}{\partial t} + \frac{\partial E}{\partial x} + \frac{\partial F}{\partial y} + \frac{\partial G}{\partial z} = 0 \qquad (4)$$

where **U**, **E**, **F**, and **G** are the vectors

$$U = \begin{bmatrix} \rho \\ \rho u \\ \rho v \\ \rho w \\ E_t \end{bmatrix} \qquad E = \begin{bmatrix} \rho u \\ \rho u^2 + p - \tau_{xx} \\ \rho uv - \tau_{xy} \\ \rho uw - \tau_{xz} \\ (E_t + p)u - u\tau_{xx} - v\tau_{xy} - w\tau_{xz} + q_x \end{bmatrix}$$

$$F = \begin{bmatrix} \rho v \\ \rho uv - \tau_{xy} \\ \rho v^2 + p - \tau_{yy} \\ \rho vw - \tau_{yz} \\ (E_t + p)v - u\tau_{xy} - v\tau_{yy} - w\tau_{yz} + q_y \end{bmatrix} \qquad (5)$$

$$G = \begin{bmatrix} \rho w \\ \rho uw - \tau_{xz} \\ \rho vw - \tau_{yz} \\ \rho w^2 + p - \tau_{zz} \\ (E_t + p)w - u\tau_{xz} - v\tau_{yz} - w\tau_{zz} + q_z \end{bmatrix}$$

and

$$E_t = \rho \left(e + \frac{u^2 + v^2 + w^2}{2} \right) \qquad (6)$$

which are non-dimensionalized using the relations

$$\rho = \rho^* \big/ \rho_\infty \qquad u = u^* \big/ a_\infty \qquad v = v^* \big/ a_\infty \qquad w = w^* \big/ a_\infty \qquad x = x^* \big/ L \qquad y = y^* \big/ L$$

$$z = z^* \big/ L \qquad T = T^* \big/ T_\infty \qquad P = P^* \big/ (\rho_\infty a_\infty^2) \qquad E_t = E_t^* \big/ (\rho_\infty a_\infty^2) \qquad t = t^* \big/ (L / a_\infty)$$

The components of the shear-stress tensor and the heat-flux vector in non-dimensional form are given by

$$\tau_{xx} = \frac{2\mu M_\infty}{3Re_L}\left(2\frac{\partial u}{\partial x} - \frac{\partial v}{\partial y} - \frac{\partial w}{\partial z}\right)$$

$$\tau_{yy} = \frac{2\mu M_\infty}{3Re_L}\left(2\frac{\partial v}{\partial y} - \frac{\partial u}{\partial x} - \frac{\partial w}{\partial z}\right)$$

$$\tau_{zz} = \frac{2\mu M_\infty}{3Re_L}\left(2\frac{\partial w}{\partial z} - \frac{\partial u}{\partial x} - \frac{\partial v}{\partial y}\right)$$

$$\tau_{xy} = \frac{\mu M_\infty}{Re_L}\left(\frac{\partial u}{\partial y} + \frac{\partial v}{\partial x}\right)$$

$$\tau_{xz} = \frac{\mu M_\infty}{Re_L}\left(\frac{\partial u}{\partial z} + \frac{\partial w}{\partial x}\right) \tag{7}$$

$$\tau_{yz} = \frac{\mu M_\infty}{Re_L}\left(\frac{\partial v}{\partial z} + \frac{\partial w}{\partial y}\right)$$

$$q_x = -\frac{\mu M_\infty}{(\gamma-1)Re_L Pr}\frac{\partial T}{\partial x}$$

$$q_y = -\frac{\mu M_\infty}{(\gamma-1)Re_L Pr}\frac{\partial T}{\partial y}$$

$$q_z = -\frac{\mu M_\infty}{(\gamma-1)Re_L Pr}\frac{\partial T}{\partial z}$$

where M_∞ is the freestream or reference Mach number

$$M_\infty = \frac{U_\infty}{\sqrt{\gamma R T_\infty}} \tag{8}$$

and the perfect gas equations of state are

$$p = (\gamma - 1)\rho e \tag{9}$$

$$T = \frac{\gamma p}{\rho}$$

and Re_L is the Reynolds number based on a reference length is

$$Re_L = \frac{\rho_\infty U_\infty L}{\mu_\infty} \tag{10}$$

To solve these equations, constant specific heats are assumed as well as a constant Prandtl number. The viscosity is found by using Sutherland's Law. The variables included in the above equations are as follows

x, y, z	Principal directions in the Cartesian coordinate system
u, v, w	Velocities in the x, y, and z directions
ρ	Density
p	Pressure
T	Temperature
γ	Ratio of Specific Heats
E_t	Total Energy
e	Internal Energy
U_∞	Freestream or Reference Velocity
a	Speed of Sound
R	Universal Gas Constant
μ	Viscosity
q_x, q_y, q_z	Heat-Flux in the x, y, and z directions
$\tau_{xx}, \tau_{yy}, \tau_{zz}$	Shear-Stress Tensor along Specific Faces
$\tau_{xy}, \tau_{xz}, \tau_{yz}$	
Pr	Prandtl Number
Re_L	Reynolds Number Based on a Reference Length L
∞	Subscript Referring to a Freestream or Reference Condition

To solve these equations, various parameters need to be specified. In nozzle flow cases, where the freestream conditions are stagnation conditions, another point

needs to be chosen for the reference location. The point chosen for these calculations is where the Mach number is one, or the nozzle throat in a one-dimensional analysis. The input to the program is the stagnation pressure, stagnation temperature, and stagnation density which can be converted to values at the throat using isentropic relations. Also necessary are the Reynolds number at the reference location, Prandtl number, reference length, reference Mach number (1.0 for these cases), and the freestream velocity components (0.0 for both cases since freestream is stagnation). The value used for the reference length is 1.0 so this variable drops out of the non-dimensionalization of the Navier-Stokes equations. The input geometry is also non-dimensionalized by this value so the input coordinates need not be changed. The inputs used for both Mach 2.4 nozzles are given below:

Stagnation Pressure	689480 Pa
Stagnation Temperature	300 ^{o}K
Stagnation Density	8.0079 kg/m^3
Reference Mach Number	1.0
Reference Length	1.0 m
Reynolds Number	1.0439 x 10^8
Prandtl Number	0.72
Ratio of Specific Heats	1.4

Given these parameters, the Navier-Stokes equations could then be solved for the dependent variables ρ, ρu, ρv, ρw, and E_t. This is done using a cell centered, central differencing scheme in space and a five-stage Runge-Kutta algorithm to advance the scheme in time. Techniques to accelerate convergence to steady-state are also included. These are implicit residual smoothing and multigrid acceleration. Each of these will be discussed in the next section. Two assumptions are also made for these computations. First, laminar flow is assumed for the entire flow. Since the flow should be laminar at the bleed slot lip, corresponding to the initial location of the calculation, this is the correct assumption until transition, which is the location that is being sought. To save calculation time and computer storage, it is also assumed that all the viscous terms containing derivatives in the streamwise direction are neglected. This is known as the "thin-layer" approximation to the Navier-Stokes equations. Since the viscous terms should be relatively small in the streamwise direction and the grid spacing is relatively large in this direction, dropping these terms should not affect the final

solution.

2.2.2 Numerical Algorithm

The space discretization begins by assuming that all the dependent variables are known at the center of all the grid cells. The flux vectors are then evaluated by finding the average values at each cell face. Finally, the total flux through any individual cell can be evaluated. This technique is described in more detail in references [57] and [58]. These schemes reduce to second order central difference schemes on smooth Cartesian meshes.

The equations are advanced in time by the use of a five-stage Runge-Kutta scheme. This approach is shown completely in reference [59]. The dependent variables at the (q+1) stage is given by

$$W^{(q+1)} = W^{(0)} - \alpha_{q+1} \frac{\Delta t}{\Omega} \left[Q\left(W^{(q)}\right) - \sum_{r=0}^{q} \gamma_{qr} D\left(W^{(r)}\right) \right] \qquad (11)$$

$$Q\left(W^{(q)}\right) = Q_c\left(W^{(q)}\right) + Q_d\left(W^{(0)}\right)$$

where

$W^{(0)}$	Solution at time level n
α_{q+1}	Tunge-Kutta Coefficients
Δt	Time Step
γ_{qr}	Weighing Factors for the Artificial Dissipation
Ω	Cell Volume
$Q_c(W^{(q)})$	Convective Fluxes at time step q
$Q_d(W^{(0)})$	Dissipative Fluxes at time level n
$D(W^{(r)})$	Artificial Dissipation

For a five-stage scheme, the variable q varies from zero to four. When q+1 is five, this corresponds to the new time level n+1. The coefficient alpha has been determined such that the scheme has the largest hyperbolic stability limit. The coefficients used for these cases are

$$\alpha_1 = 1/4 \qquad \alpha_2 = 1/6 \qquad \alpha_3 = 3/8 \qquad \alpha_4 = 1/2 \qquad \alpha_5 = 1$$

This scheme exhibits the good high-frequency damping that is required for a rapidly convergent multigrid method [59]. It should be noted that the dissipative fluxes are only evaluated on the first stage and appear not to have an affect on the scheme stability [59]. This allows for a significant reduction in computational effort for the scheme. For a good parabolic stability, the artificial dissipation terms are evaluated on the first, third, and fifth stages. The weighing factors for the dissipation terms must satisfy the condition

$$\sum \gamma_{qr} = 1 \tag{12}$$

The individual factors are defined in reference [59]. The maximum CFL number allowed by stability for this scheme is 3.75, which is about 30 percent larger than for the fourth-order Runge-Kutta scheme with one evaluation of the artificial dissipation. Finally, the steady-state solution is independent of the time step, and therefore, convergence acceleration techniques are easily employed in this method.

Three methods are used to accelerate convergence of the basic scheme. These consist of local time stepping, implicit residual smoothing, and multigrid. The smallest time step computed in a computational domain is used for all cells in a global time stepping method to advance the calculation in time. However, this method is inefficient in the cells where a larger time step would be allowed by stability. Local time stepping is therefore applied to march the solution to steady-state using the maximum time step allowed by stability in each individual cell. Using this method, steady-state will be reached in some cells more quickly than by using a global time stepping method. Therefore, steady-state solutions will be available for flux calculations in cells with smaller stability limits, allowing for faster overall convergence. Both convection and diffusion stability limits are included in the calculation of the time step in any cell.

Implicit residual smoothing is used to extend the stability range of the basic scheme. The residual is defined by

$$R^{(m)} = \alpha_m \frac{\Delta t}{\Omega} \left[Q\left(W^{(m-1)}\right) - D^{(m-1)} \right] \tag{13}$$

where m is the Runge-Kutta stage and D(m) is the total artificial dissipation at stage m.

Since the residual is only dependent on the neighboring cells in an explicit scheme, information at one cell may take many time steps to reach another cell. The speed at which this information would normally travel limits the maximum time step allowed by the scheme. Therefore, implicitly averaging the residuals makes the solution at any point partially dependent on the solution at all the other points. This increases the stability of the scheme and allows for larger time steps to be taken than would be allowed in the basic scheme. This method typically allows for a factor of two increase in the CFL number for the basic scheme, making the CFL number 7.5 for the scheme described. A further discussion of this method can be found in reference [60].

The main difficulty in finding a steady-state solution to the Navier-Stokes equations is the elimination of the unsteady acoustic waves generated during the initialization. The hardest waves to eliminate are the ones that have wavelengths that are the same order of magnitude as the grid spacing, or longer. To help eliminate these waves, multigrid methods have been developed. The purpose of multigrid is to change the number of grid points in an orderly manner so that waves with long wavelengths on the fine grids will have short wavelengths on the coarse grids. In this manner, waves that ordinarily would have taken many iterations to eliminate could then be eliminated in fewer iterations.

Coarser meshes are obtained in the multigrid method by the elimination of every other mesh line in each coordinate direction. The solution is then transferred to the coarser mesh by a rule that conserves mass, momentum, and energy. Residuals are transferred to the coarser meshes by summation and are used as a forcing function to represent the fine grid solution on the coarse mesh. These strategies are discussed in more detail in references [61] and [62]. This process is repeated until the coarsest mesh is reached. Then the corrections are transferred to the next finer mesh by bilinear interpolation. As stated in reference [59], the coarse grid corrections are smoothed using the implicit residual smoothing scheme discussed before, with constant coefficients, before they are passed to the next finer grid. Using this technique allows the multigrid method to be effective for a wider range of flows.

A fixed W-cycle multigrid technique, with a full multigrid method, (FMG), is used to provide a well-conditioned starting solution for the finest mesh. These multigrid strategies are shown in figures 10 and 11 below. The implementation of the W-cycle in this code consists of a single sweep through the domain at each grid level. One complete multigrid cycle begins at point 1 in figure 10 and finishes at point 2. In the initial stages of the full multigrid method, shown in figure 11, 100 multigrid cycles

Finest Grid Level ①   ②

Coarsest Grid Level
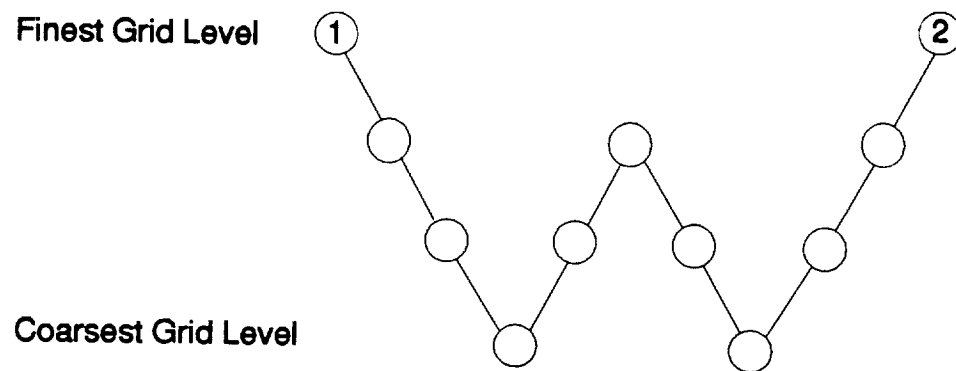
Figure 10-W-cycle Implementation for Multigrid

Finest Grid Level   ④

                                                    ③

                                    ②

Coarsest Grid Level ①——◯
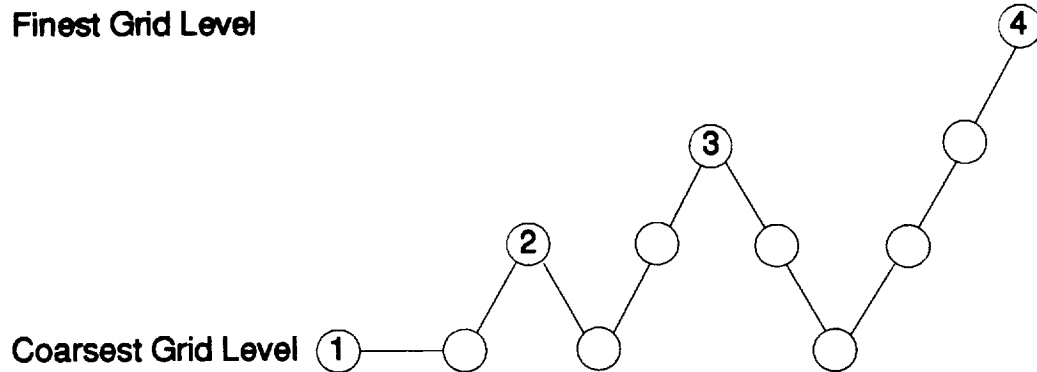
Figure 11-FMG Implementation Method

are completed at each of the coarse levels shown as points 1, 2, and 3. Point 4 signifies the beginning of the W-cycle for the calculation. By using this approach, acoustic waves with long wavelengths can be damped in the coarse levels to provide a good

initial solution to the finest grid level.

Artificial viscosity is necessary in central differencing schemes for maintaining numerical stability. This viscosity will suppress high-frequency waves that are not damped by central differencing schemes and will dampen oscillations from capturing shock waves. Scalar dissipation models typically work well with most problems, but are not accurate enough for laminar flow problems. In this study, scalar dissipation is replaced with a matrix dissipation. This then gives the appropriate amount of artificial viscosity to each individual wave. This technique is fully described in reference [63].

The artificial dissipation technique used is similar to that originally developed by Jameson, Schmidt, and Turkel [57]. The total artificial viscosity consists of a blend of second and fourth differences in each coordinate direction. The purpose of the second difference term is to add an entropy-like condition to suppress oscillations near shock waves. Therefore, this term will be small in smooth regions of the flow field. The fourth difference is added to damp high-frequency waves and allow convergence to steady-state. The fourth difference, however, causes oscillations in the neighborhood of shocks. A shock detector, consisting of a pressure sensor, is used to turn off the fourth difference near shocks so only the second difference is operative. The pressure sensor used is given in reference [63].

Finally, initial conditions and boundary conditions for the scheme must be addressed. The inflow and outflow boundary conditions employ point boundary conditions based on characteristic theory. For the subsonic inflow of the nozzles, four of the dependent variables are set from a one-dimensional analysis and the fifth is determined from the solution inside the domain. Zeroth-order extrapolation is done for the supersonic outflow boundary. The no-slip boundary condition is imposed at the solid walls. It is also assumed that the walls are adiabatic so the temperature is computed from the reduced energy equation

$$\frac{\partial T}{\partial \eta} = 0 \qquad (14)$$

where η is the direction normal to the surface. The wall pressure is calculated by setting the normal pressure gradient to zero at the wall. The initial conditions were set using simple one-dimensional area ratios. Using this technique, the pressure, density, temperature, and total velocity could be set at every point. The velocity components were then found by assuming that the velocity at every point was tangent to the local

grid. This technique gives a reasonable initial approximation to the final solution.

2.2.3 Crossflow Determination

After the Navier-Stokes calculations on the nozzles were completed, the boundary-layer crossflow needed to be calculated from the solution files. Since the flow is symmetric around both the centerplane and the diagonal, the crossflow only needed to be determined on one wall. The wall chosen for this is the one perpendicular to the z-direction. At each constant x and constant y location from the center of the nozzle to the edge of the boundary-layer on the wall that is perpendicular to the y-direction, z is varied from the wall to the edge of the boundary-layer to find the location of the maximum crossflow velocity (W_{MAX}) and the distance between the wall and the location where the crossflow velocity becomes 10 percent of its maximum value (δ_{10}).

To calculate the crossflow, the unit vector in the crossflow direction must be determined. Since the crossflow must be perpendicular to the wall normal vector and the local inviscid flow, the dot product of the crossflow vector with both the wall unit normal and the local inviscid flow vector must be zero. This is given by

$$q_1 n_1 + q_2 n_2 + q_3 n_3 = 0 \qquad (15)$$

$$q_1 u_e + q_2 v_e + q_3 w_e = 0 \qquad (16)$$

where

q_m = component in the crossflow direction

n_m = component locally normal to the wall

u_e, v_e, w_e = component of the local edge velocity

A discussion of the effects of the boundary-layer edge definition on the calculation of the crossflow can be found in the next chapter. To solve for q_1, q_2, and q_3 uniquely, a normalization equation is needed. Assuming that most of the crossflow will be parallel to the wall and perpendicular to the x-direction, q_2 is first chosen to be one. Solving the equations 15 and 16 with this assumption gives

$$q_1 = \frac{-v_e - q_3 w_e}{u_e} \qquad (17)$$

$$q_2 = 1 \tag{18}$$

$$q_3 = \frac{v_e n_1 - u_e n_2}{u_e n_3 - w_e n_1} \tag{19}$$

The solutions to the above equations are then normalized to obtain a unit vector in the crossflow direction.

This technique can also be used to determine the streamwise direction. Since this direction is perpendicular to the wall normal and the crossflow direction, the dot products are taken with these vectors and set to zero. Choosing s_1 to be one, since most of the streamwise profile is in the x-direction, the components of the streamwise direction becomes

$$s_1 = 1 \tag{20}$$

$$s_2 = \frac{-q_1 - q_3 s_3}{q_2} \tag{21}$$

$$s_3 = \frac{q_1 n_2 - q_2 n_1}{q_2 n_3 - q_3 n_2} \tag{22}$$

These equations are also normalized to obtain the unit vector in the streamwise direction.

The wall normal needs to be found at every computational plane that makes up the z-wall. Since a vector is normal to a plane if it is normal to two lines in that plane that are not parallel, only two lines in each computational plane need to be known. The two lines that are chosen for this are

$$\hat{l}_1 = x_\xi \hat{i} + y_\xi \hat{j} + z_\xi \hat{k} \tag{23}$$

$$\hat{l}_2 = x_\eta \hat{i} + y_\eta \hat{j} + z_\eta \hat{k} \tag{24}$$

Specifically, these two lines represent the vectors that pass through the points i,j,k and i+1,j,k and i,j,k and i,j+1,k respectively. The i counter changes in the streamwise direction and j in the direction parallel to the wall on which the crossflow is being calculated. Taking the dot product of both these lines with the wall unit normal gives two equations:

$$x_\xi n_1 + y_\xi n_2 + z_\xi n_3 = 0 \tag{25}$$

$$x_\eta n_1 + y_\eta n_2 + z_\eta n_3 = 0 \qquad (26)$$

Here again one more equation is needed to solve for n_1, n_2, and n_3 uniquely. Arbitrarily taking n_3 equal to one, solving the set of equations, and normalizing them to obtain the wall unit normal gives

$$n_1 = \frac{y_\eta z_\xi - y_\xi z_\eta}{\left[\left(y_\eta z_\xi - y_\xi z_\eta\right)^2 + \left(x_\eta z_\xi - x_\xi z_\eta\right)^2 + \left(x_\xi y_\eta - x_\eta y_\xi\right)^2\right]^{\frac{1}{2}}} \qquad (27)$$

$$n_2 = \frac{-\left(x_\eta z_\xi - x_\xi z_\eta\right)}{\left[\left(y_\eta z_\xi - y_\xi z_\eta\right)^2 + \left(x_\eta z_\xi - x_\xi z_\eta\right)^2 + \left(x_\xi y_\eta - x_\eta y_\xi\right)^2\right]^{\frac{1}{2}}} \qquad (28)$$

$$n_3 = \frac{-\left(x_\xi y_\eta - x_\eta y_\xi\right)}{\left[\left(y_\eta z_\xi - y_\xi z_\eta\right)^2 + \left(x_\eta z_\xi - x_\xi z_\eta\right)^2 + \left(x_\xi y_\eta - x_\eta y_\xi\right)^2\right]^{\frac{1}{2}}} \qquad (29)$$

where

$$x_\xi = x_{i+1,j,k} - x_{i,j,k}$$
$$y_\xi = y_{i+1,j,k} - y_{i,j,k}$$
$$z_\xi = z_{i+1,j,k} - z_{i,j,k}$$
$$x_\eta = x_{i,j+1,k} - x_{i,j,k}$$
$$y_\eta = y_{i,j+1,k} - y_{i,j,k}$$
$$z_\eta = z_{i,j+1,k} - z_{i,j,k}$$

x, y, z = streamwise and two normal-to-wall nozzle coordinates
ξ, η, ζ = streamwise and two normal-to-wall computational coordinates

After the wall unit normal is known, the crossflow and streamwise directions can be calculated assuming the edge parameters are known. Finally, knowing the crossflow and streamwise directions, the magnitude of the crossflow and streamwise

profiles can be found at every point inside the boundary-layer by taking the dot products of the crossflow and streamwise directions with the local velocity vector. The magnitude of the crossflow can then be used to calculate the various crossflow Reynolds numbers used in this investigation.

The procedure used for calculating the standard crossflow Reynolds number is straightforward. First, the crossflow magnitudes are searched to find the maximum crossflow velocity in any profile. After this point is found, the furthest distance from the wall, inside the boundary-layer, where the crossflow becomes 10 percent of the maximum is determined. Then, since the edge parameters are known, the crossflow Reynolds number can be calculated from equation 2. A region of s-shaped profiles existed in both nozzles that complicated the calculation of the parameter, however. If the above definition is used for all the parameters, the crossflow Reynolds number can still be calculated but a discontinuity occurs in the solution. This will be discussed further in the results for this parameter. Stability is determined at any point for this method by equation 30 developed by Godil and Bertelrud [40].

$$R_{cf_{tr}} = 200\left[1 + \frac{\gamma-1}{2}M_e^2\right] \tag{30}$$

where

$R_{cf_{tr}}$ Transition Crossflow Reynolds Number

M_e Local Edge Mach Number

After the standard crossflow Reynolds number is known, Reed and Haynes crossflow Reynolds number can be calculated by the addition of the corrections for a cooled wall and compressibility as shown in equation 4. These corrections are

$$H = \frac{\zeta(\delta_{10})}{\int_0^{\zeta(\delta_{10})}\left(\frac{T}{T_e}\right)d\zeta} \tag{31}$$

$$L = \frac{\left(\dfrac{C^*}{C^*_{ad}}\right)^{\frac{1}{2}}\left(3.279 + 1.721\left[\dfrac{T_w}{T_{ad}}\right][1+A] + 0.664A\right)}{(5 + 2.385A)} \qquad (32)$$

where

$$A = \frac{Pr^{1/2}(\gamma - 1)M_e^2}{2}$$

$$C^* = \frac{\left(T^*/T_e\right)^{1/2}\left(1 + 110.4/T_e\right)}{T^*/T_e + 110.4/T_e}$$

$$C^*_{ad} = \frac{\left(T^*_{ad}/T_e\right)^{1/2}\left(1 + 110.4/T_e\right)}{T^*_{ad}/T_e + 110.4/T_e} \qquad (33)$$

$$\frac{T^*}{T_e} = 0.5 + \frac{0.5T_w}{T_e} + \frac{A}{6}$$

$$\frac{T^*_{ad}}{T_e} = 0.5 + 0.5*(1+A) + \frac{A}{6}$$

M_e	Local edge Mach number
Pr	Prandtl number
$\zeta(\delta_{10})$	Distance along wall normal from wall to location of δ_{10}
T_w	Local wall temperature
T/T_e	Local temperature divided by local edge temperature
H	Correction for compressibility effects
L	Correction for wall cooling effects

Since the wall and edge parameters are known at any point, the correction for wall cooling is easily calculated. The integral of T/T_e is calculated using a trapezoidal integration method across the boundary-layer, along the wall normal. The compressibility correction can then be calculated by dividing the distance from the wall to the edge of the boundary-layer by the integrated boundary-layer temperature. Multiplying these two corrections with the standard crossflow Reynolds number gives the Reed and Haynes crossflow Reynolds number. Stability for this method is determined by the equation

$$R = \frac{R_{cfR\&H}}{W_{MAX}/U_e} \tag{34}$$

where W_{MAX}/U_e is in percentages. Stability is then predicted for R less than or equal to 44.0 for quiet flows. This method is limited, however, to the range 2% < W_{MAX}/U_e < 8% corresponding to the range of data that was investigated when defining the parameter R.

The crossflow Reynolds number developed by Beasley can be calculated by integrating the crossflow magnitude from the wall to the edge of the boundary-layer, along the wall normal, using a trapezoidal integration technique. This result is then divided by the kinematic viscosity at the edge as in equation 3 to get the solution. Also of interest is the streamwise shape factor (H_{shp}) for stability analysis. First, both the displacement thickness (δ^*) and the momentum thickness (θ) are found by integrating the streamwise velocity profile across the boundary-layer using the compressible formula [21]. The integration is again done using a trapezoidal integration technique. Finally, the shape factor is calculated by dividing the displacement thickness by the momentum thickness. The stability limits of the solution is then set by equation 35 which is valid for the range 2.3 < H_{shp} < 2.7.

$$Cl = \frac{300}{\pi} \tan^{-1}\left[\frac{0.106}{\left(H_{shp} - 2.3\right)^{2.05}}\right] \tag{35}$$

A computer program has been written following these procedures to determine the crossflow in both Mach 2.4 nozzles. A listing of the program can be found in appendix B, a brief description of the methods follows. The program reads in two

binary files consisting of the geometry file created by the grid generation program and the solution file of dependent variables created by the Navier-Stokes solver. The program writes four files. First, DIFFP is the difference in pressure between the corner and the center of a wall. This data is used to compare with the original design data. Second is the file titled CROSSFLOW and contains the data for contour plots of the crossflow Reynolds numbers and the stability criterion. Third is a file entitled CORNER which creates a cornerplane cut of the data for plotting Mach contours. Finally, CROSSFLOWMAG contains line plots of the crossflow magnitude in the boundary-layer at various locations.

After the data is read in and manipulated, the edge of the boundary-layer on the wall perpendicular to the y-direction is found on the centerline. This is the outer limit for the calculation of the crossflow so the corner would not be included in the calculation. Then, at each point, the wall normal is calculated and a check is made to make sure it is inside the computed domain. The program then marches along the wall normal and saves the velocity every time the normal vector crosses a grid line. This procedure continues until the boundary-layer edge is crossed. After the edge is found, the streamwise and crossflow directions can be calculated. The program again marches through the boundary-layer to calculate the streamwise and crossflow magnitudes, find W_{MAX} and δ_{10}, and integrate to find the compressibility correction, displacement thickness, and momentum thickness. Finally, the crossflow Reynolds numbers and the stability criterion are calculated and the program ends. The data is then plotted and analyzed to get an estimate of the boundary-layer stability.

CHAPTER III   RESULTS AND DISCUSSION

The flow fields in both Mach 2.4 nozzles were simulated with the 3D Navier-Stokes solver LARCK. The approximate memory and run-time requirements to converge the solutions by four orders of magnitude, starting from the first FMG level, on NASA Langley's CRAY-YMP are given below:

Table #2 - Computational Requirements

Grid	Hours	Memory (Megawords)
137x41x41	12	15
201x65x65	30	48
305x97x97	142	158

Increasing the number of grid points has a linear effect on the amount of memory required. The time necessary for convergence, however, is not linear. This is most likely due to the increase in cell aspect ratios in the finer grids. The convergence behavior for these solutions is shown in figures 12-15. Figure 12 is the convergence history for the short Mach 2.4 nozzle using the coarse grid, figure 13 is the medium grid, and figure 14 is the fine grid. Finally, figure 15 is the convergence history for the long nozzle using the 201x65x65 grid. The discontinuities in each of these figures occurs with the addition of another level to the FMG cycle. When a new level is added, an interpolation of the solution to the new level must be performed. This interpolation introduces round-off error into the solution, causing the jump in the residual. The
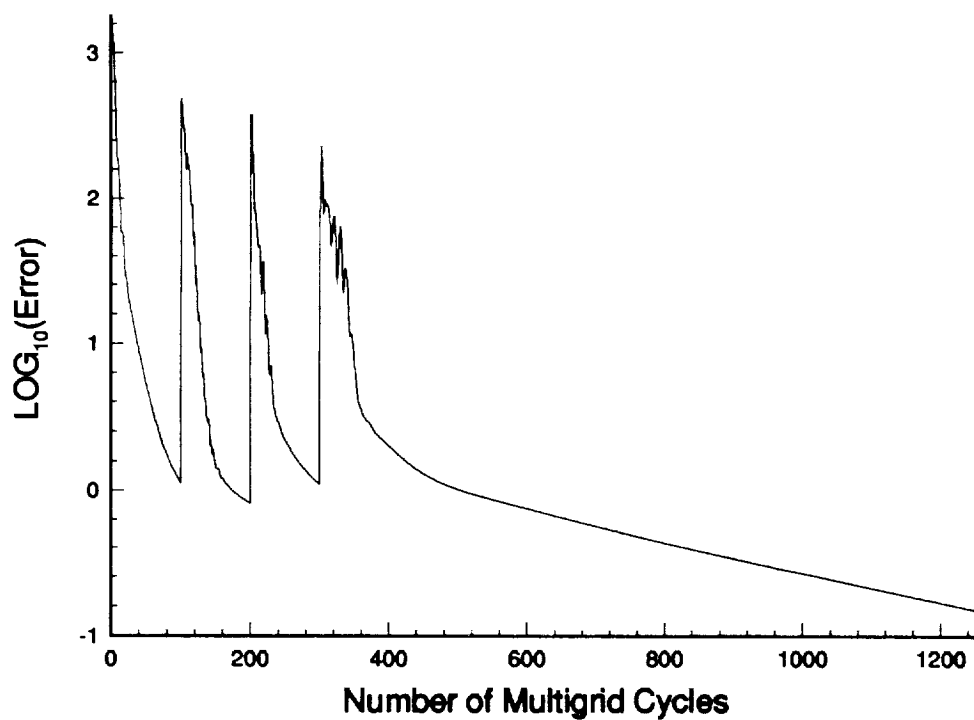
Figure 12-Residual History for the Short Mach 2.4 Nozzle, 137x41x41 Grid
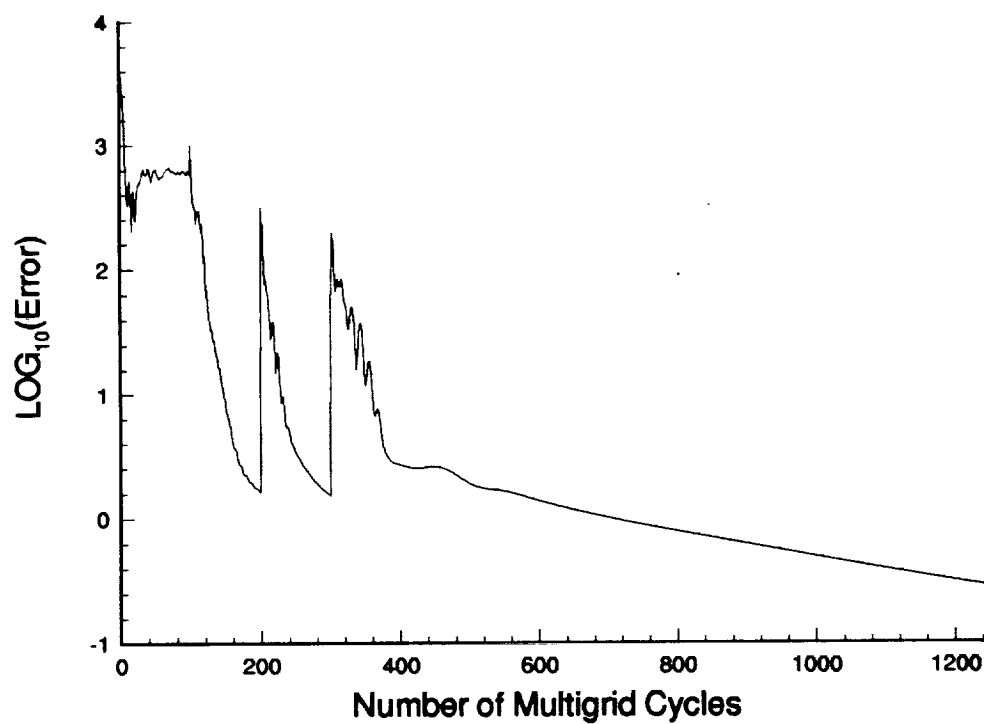
Figure 13-Residual History for the Short Mach 2.4 Nozzle, 201x65x65 Grid
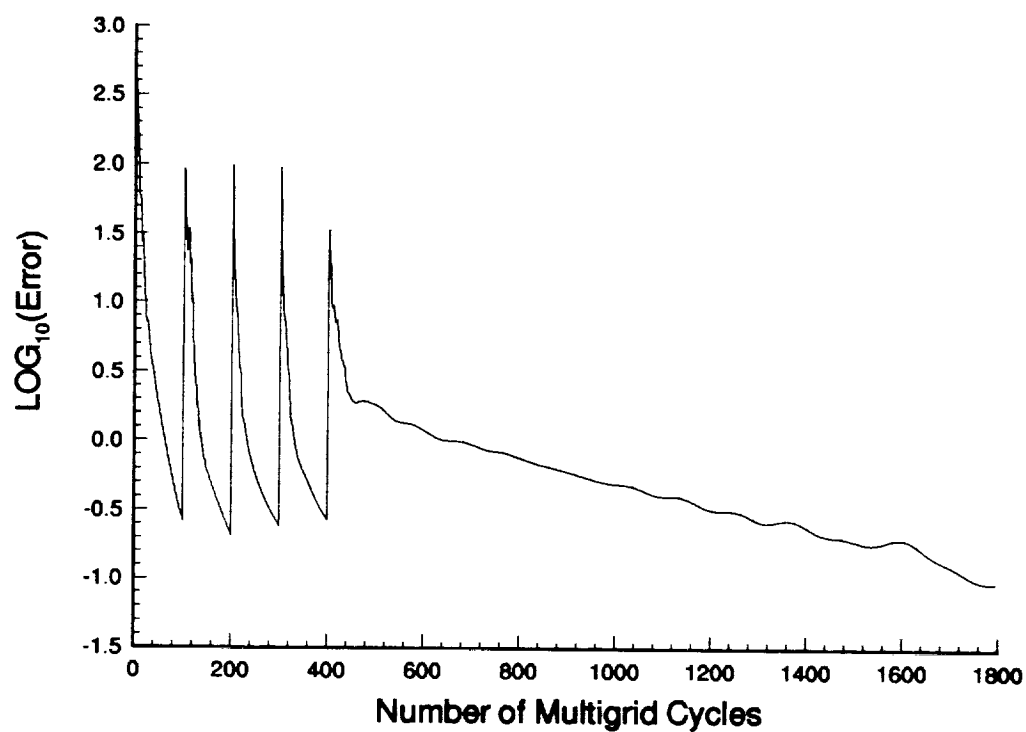
Figure 14-Residual History for the Short Mach 2.4 Nozzle, 305x97x97 Grid
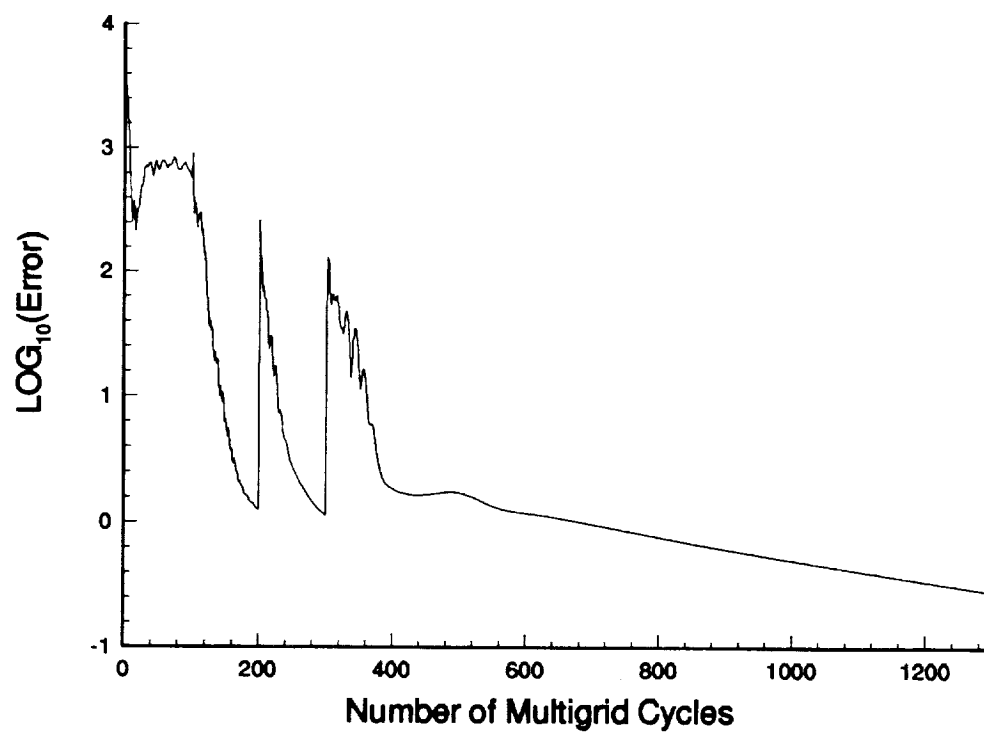
Figure 15-Residual History for the Long Mach 2.4 Nozzle

round-off error is, however, eliminated in approximately 50 multigrid cycles after the introduction of a new level. Also note that four orders of magnitude reduction in the residual was not achieved in the fine grid calculation. The poor convergence rate for this grid made it too expensive to complete. This was most likely due to the high aspect ratios of the grid, along with the possibility of poor damping at the inlet of the nozzle. It was felt that the 3 to 3.5 orders of magnitude that was achieved made the solution adequate for comparison with the other grids.

3.1 Boundary-Layer Edge Definition

The first step in analyzing the data was to determine how the boundary-layer edge definition effected the calculation of the boundary-layer parameters. Since this definition effects the calculation of the crossflow Reynolds numbers, the definition is important. The boundary-layer edge definition analysis was done using the results from the medium resolution grid on the short Mach 2.4 nozzle.

Since the streamwise velocity in the 'inviscid' flow region need not be constant at any streamwise location, the edge location is relatively arbitrary in a Navier-Stokes calculation. However, in shock-free nozzle flow, the total pressure must remain constant outside the boundary-layer. Therefore, this parameter can be used to determine the boundary-layer edge. The question then becomes how much of a total pressure drop must exist before the edge is reached. For a three-dimensional nozzle with no experimental results to verify analysis (like those presented here), this question becomes even more difficult.

To investigate how the velocity and total pressure change through the boundary-layer, the u-component of the velocity was plotted along with the total pressure divided by the freestream total pressure near the wall. This can be seen in figure 16. Note that these values are taken from the centerplane of the nozzle at the exit. At this location, the wall normal is perpendicular to the x-direction and therefore, the u-component of the velocity should be equal to the total velocity in the streamwise direction. Therefore, by using this location, the analysis is greatly simplified. In this figure, the u-velocity appears to reach the edge at a y-location between 0.107m and 0.109m. These locations correspond to the values of P_o/P_{oFS} of between 1.0 and 0.9, respectively.

Two edge locations, $P_o = 0.90 \, P_{oFS}$ and $0.98 \, P_{oFS}$, were then chosen to further analyze the crossflow Reynolds number data. The data for W_{MAX}/U_e in percentages
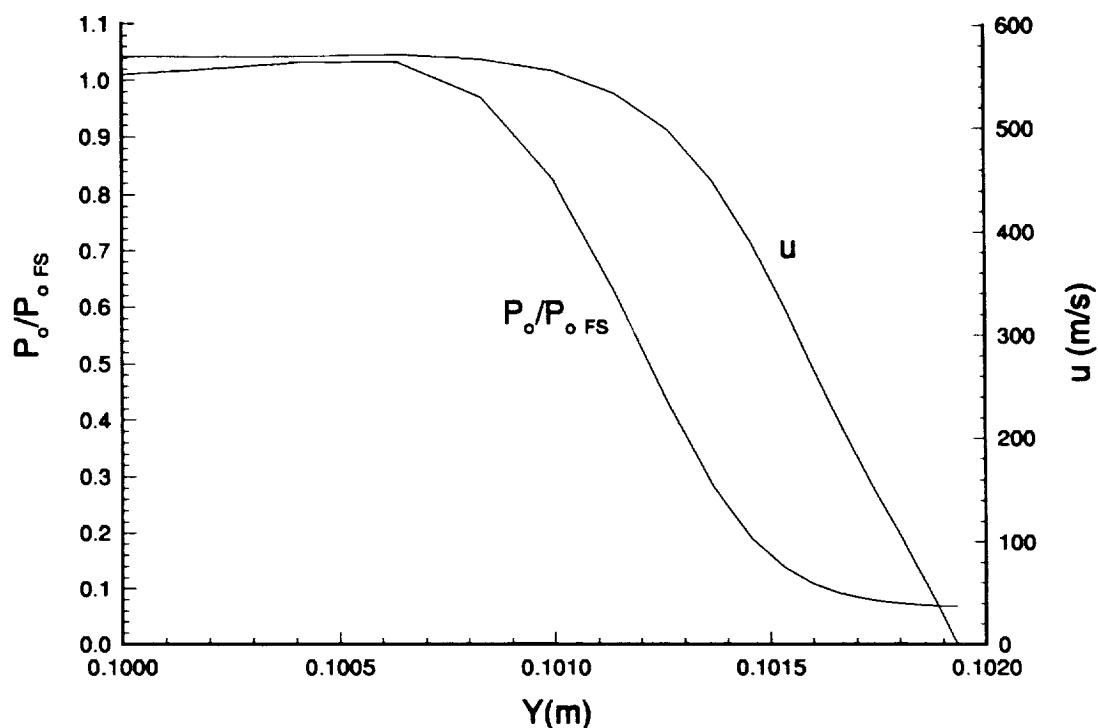
Figure 16-Total Pressure Ratio and U-Velocity Component in the
Boundary-Layer Region

along half of the z-wall for both edge definitions is plotted in figure 17. Note the line approximately 0.4m downstream of the throat that is unlabeled. This line is the interpolated location where the crossflow changes direction from positive, or towards the corner, to negative, or away from the corner. The direction change causes a jump in both the standard and the Reed and Haynes crossflow Reynolds numbers, as can be seen in figures 18 and 19 respectively. Further analysis of the flow characteristics in this region are presented in the next section.

Investigation of figure 17 shows that the edge definition in the nozzle throat region has a significant affect on the calculation of the maximum crossflow, while little difference is seen near the exit. The differences in the throat are most likely due to the differences in the edge velocity for each definition. Since the boundary-layer at the throat is relatively thin, the streamwise velocity changes rapidly over a small distance. Therefore, large differences can occur in the calculated edge velocity for each edge definition. In the exit, however, the boundary-layer is much thicker, and therefore, should have much smaller differences between edge velocities for each edge definition.
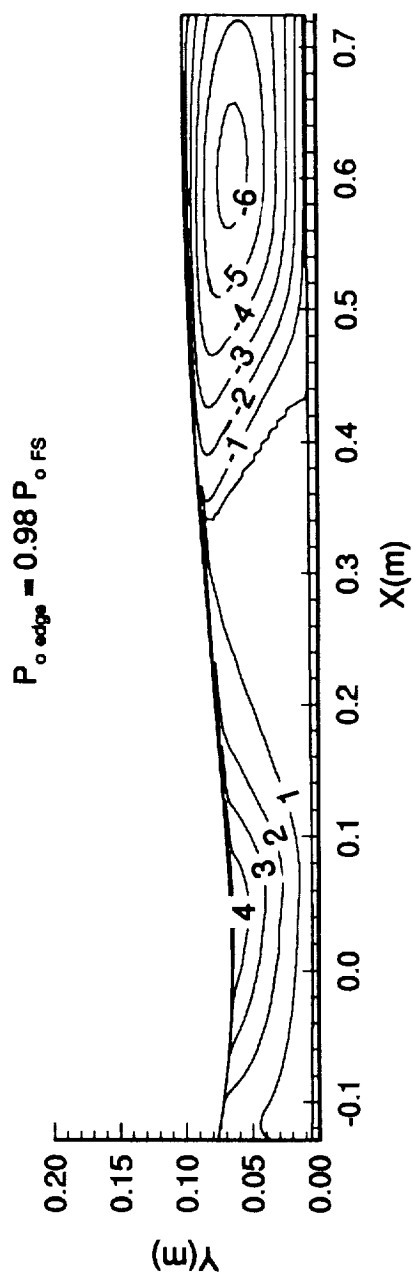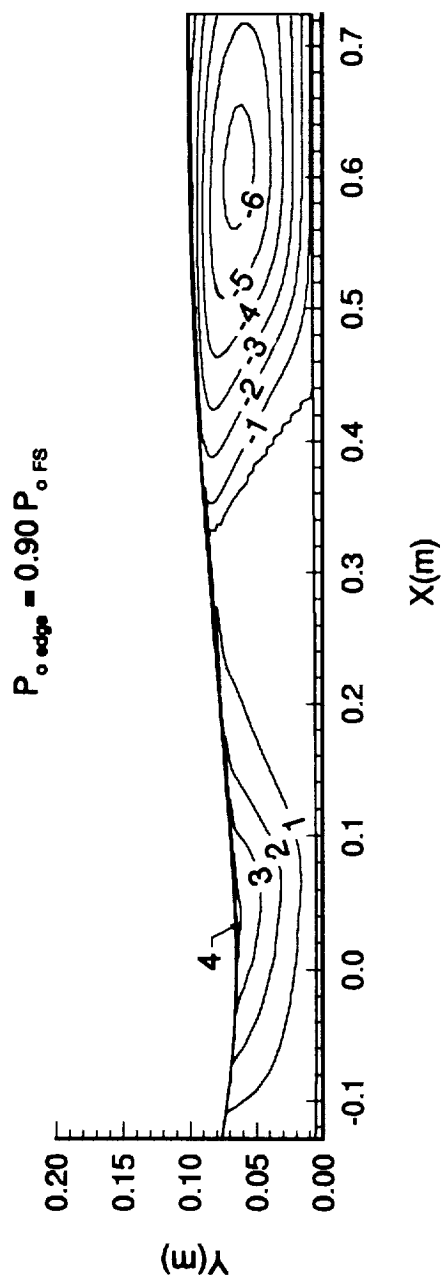
Figure 17-W_{MAX}/U_e in Percentages for Two Boundary-Layer Edge Definitions
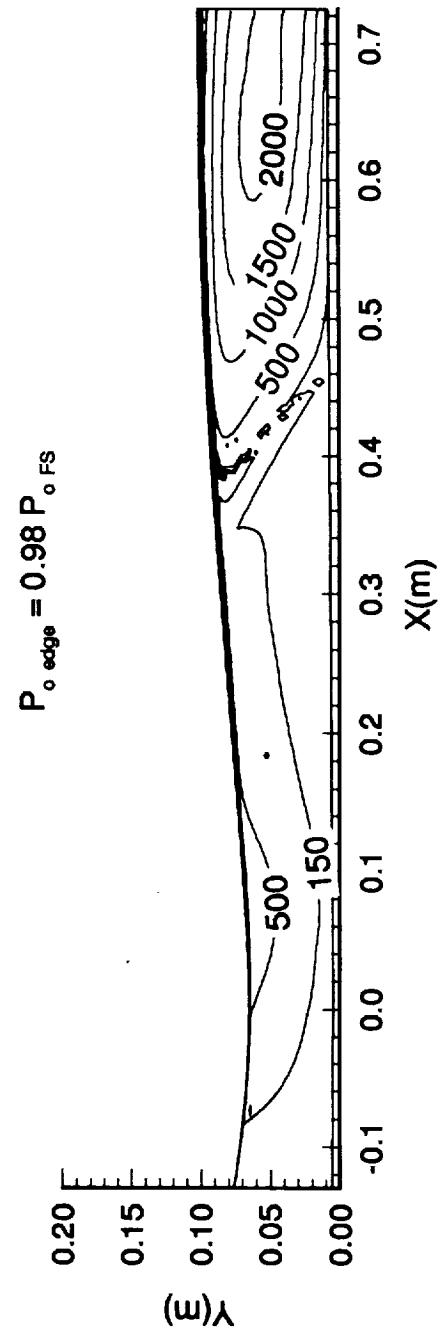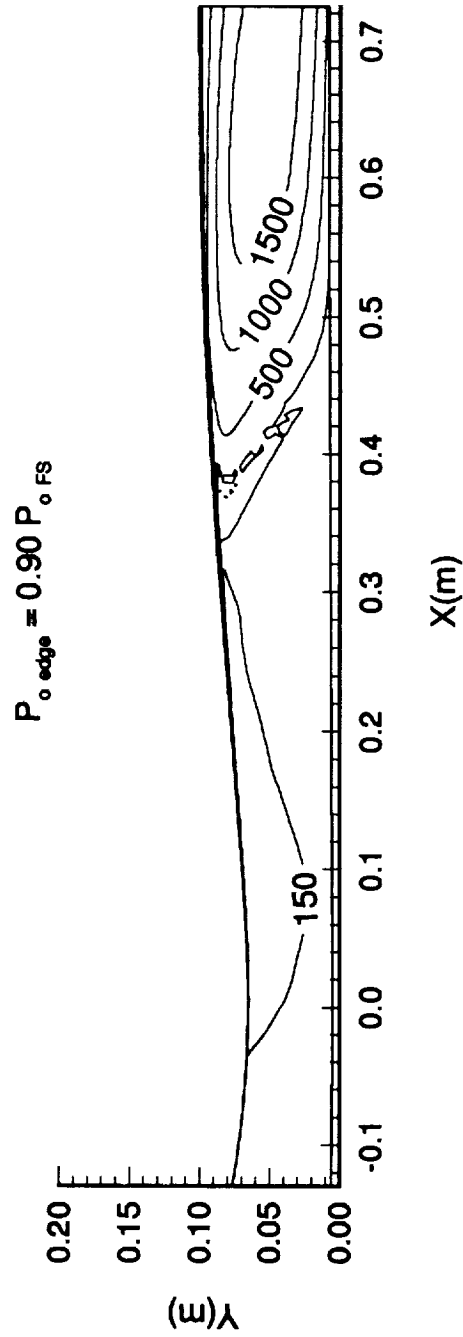
Figure 18-Standard Crossflow Reynolds Number for Two Boundary-Layer Edge Definition
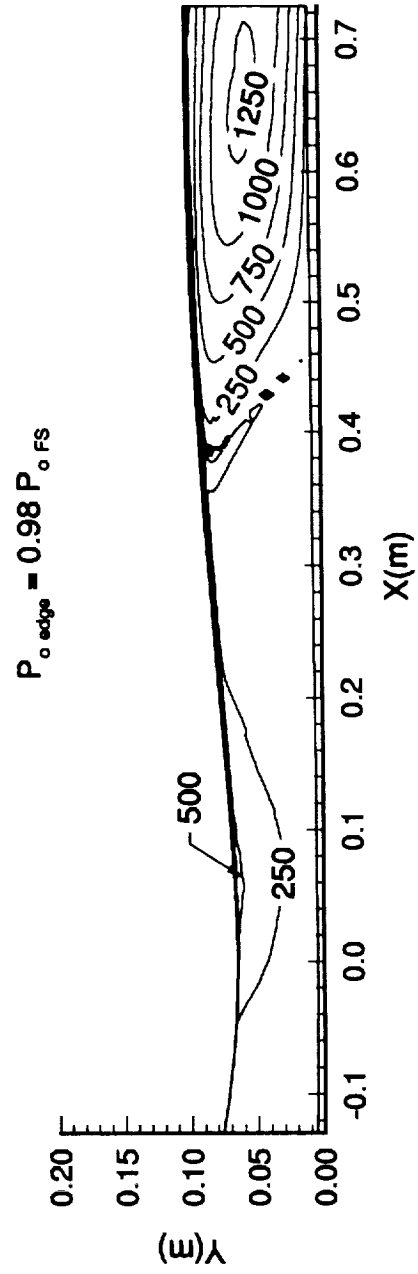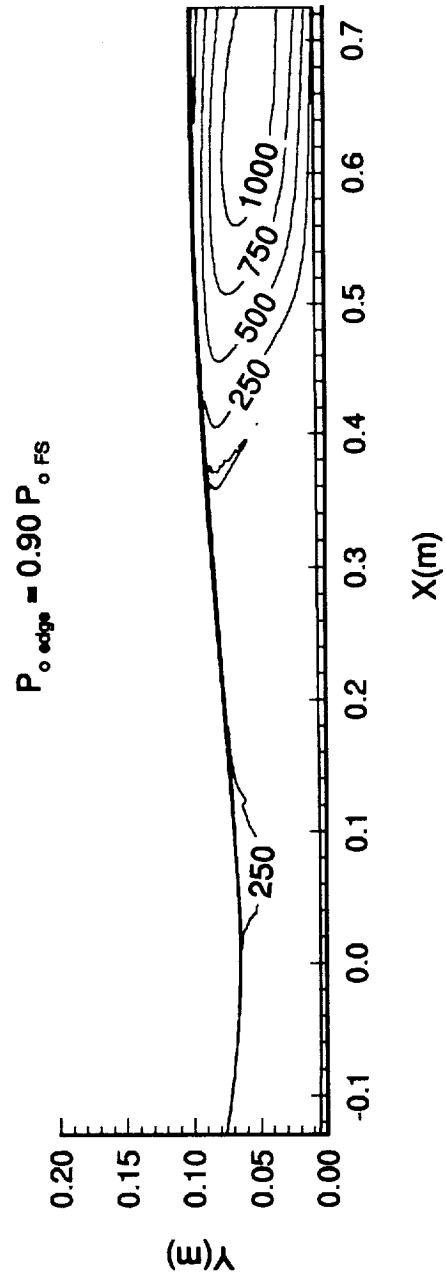
Figure 19-Reed and Haynes Crossflow Reynolds Number for Two Boundary-Layer Edge Definitions
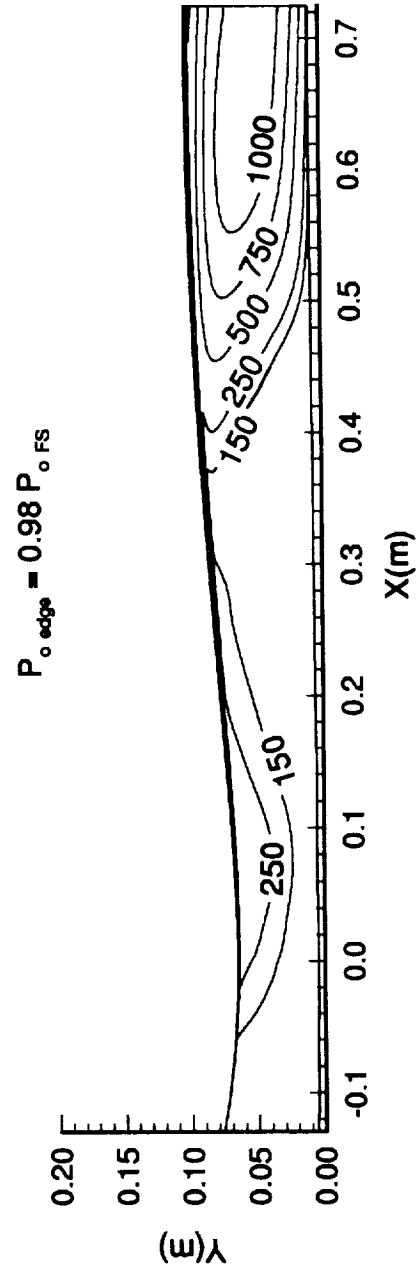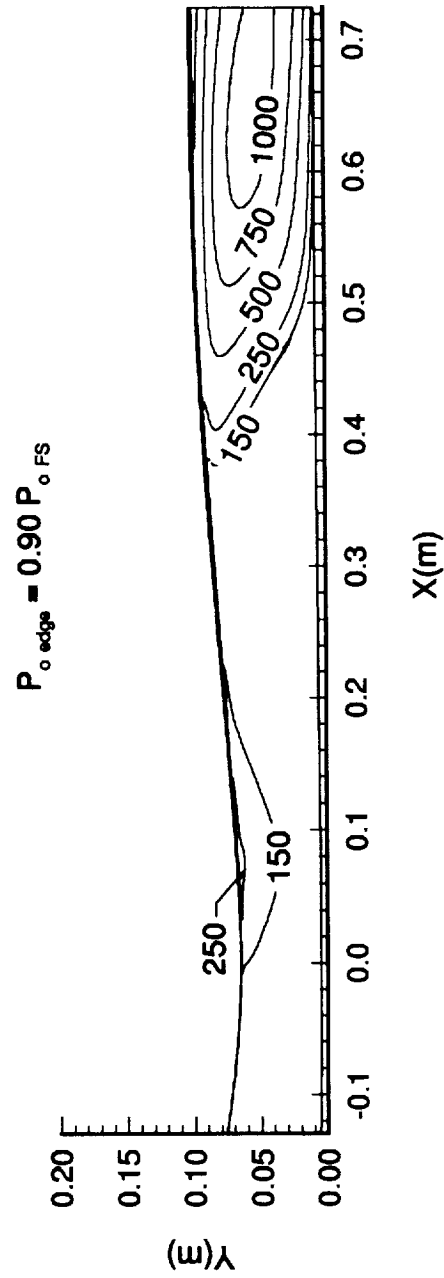
Figure 20-Crossflow Reynolds Number by Beasley for Two Boundary-Layer Edge Definitions
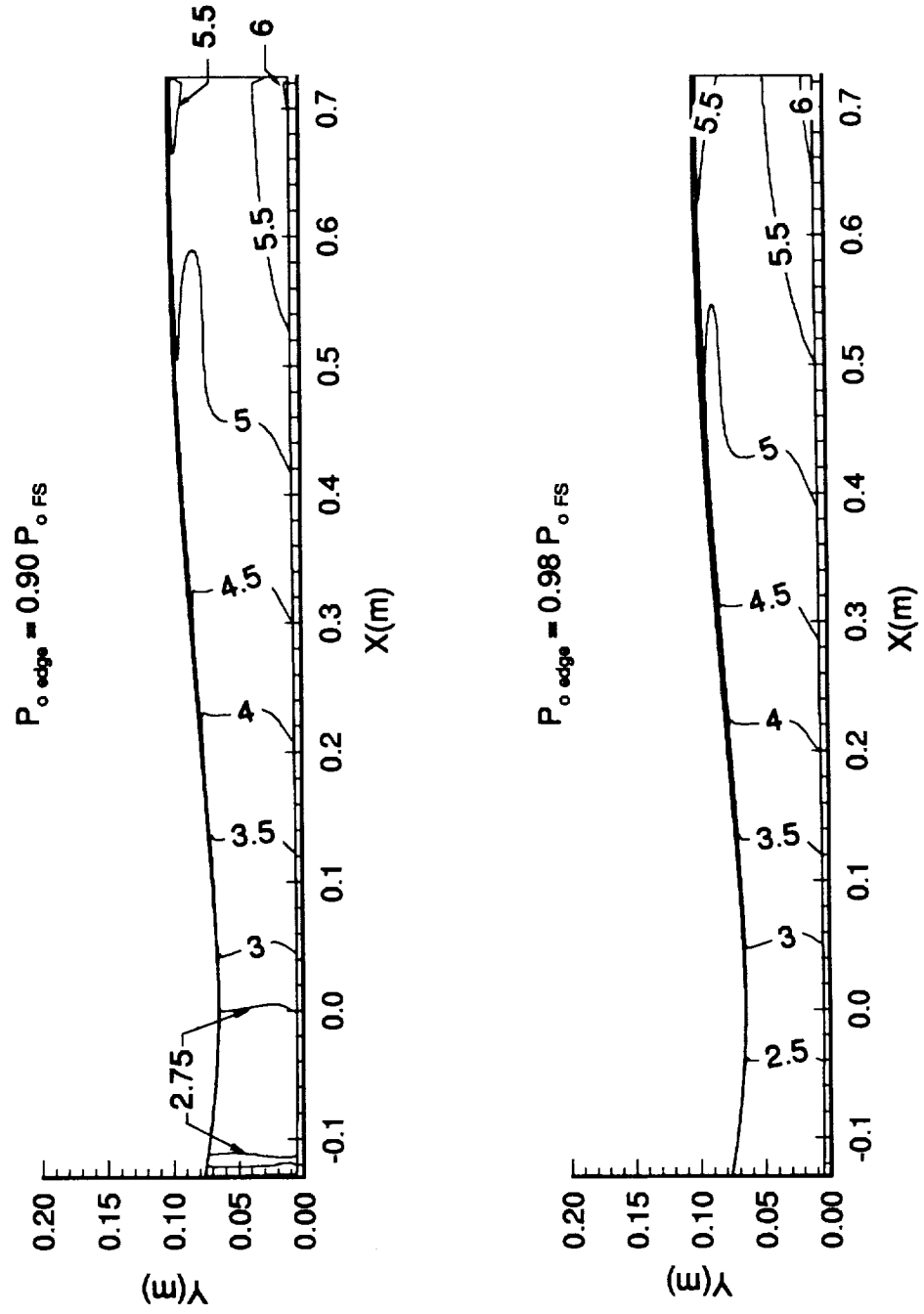
Figure 21-Streamwise Shape Factor for Two Boundary-Layer Edge Definitions

This leads to smaller differences in the calculated crossflow, which was observed in figure 17.

The various crossflow Reynolds numbers have been plotted in figures 18-20 for both of the boundary-layer edge definitions. Figure 18 shows the standard crossflow Reynolds number. As in figure 17, the standard crossflow Reynolds number is significantly affected by the change of edge definitions the in the throat region. However, near the exit, change in the crossflow Reynolds number between the two definitions is much smaller than in the throat. Assuming that the edge definition does not affect the kinematic viscosity very much, the changes seen in the throat are due to the changes in the maximum crossflow velocity. The differences in W_{MAX} affect δ_{10} in this calculation as well. Figure 19 shows Reed and Haynes crossflow Reynolds number for both edge definitions. This figure shows the same trends that were seen in the standard crossflow Reynolds number. Therefore, the edge definition does not seem to significantly affect the corrections for compressibility or wall cooling in Reed and Haynes correlation. Finally, figure 20 shows the crossflow Reynolds number developed by Beasley, shown in equation 3, for both edge definitions. Since this parameter depends on the integral of the crossflow velocity profile, the effect of the edge definition on the crossflow direction can be better estimated from these results than from the previous two crossflow Reynolds numbers. This is assuming, however, that the edge definition does not affect the kinematic viscosity very much at the boundary-layer edge. Near the throat, Beasley's crossflow Reynolds number seems to be severely affected when the edge definition is changed. However, near the exit, the change in the edge definition affects the results much less than in the throat region. There appears to be more of a change in this parameter near the exit than in the other crossflow Reynolds numbers, however. This signifies that the change in the edge definition may affect the crossflow calculation more than was apparent from the previous results.

The streamwise shape factor is plotted for both edge definitions in figure 21. This figure shows that only in the throat region does the edge definition seem to affect the streamwise shape factor. Downstream of where the streamwise shape factor is 3.0, the two calculations are almost identical. However, the throat region is the region of interest for this parameter since the C1 prediction criteria is only valid for $2.3 < H_{shp} < 2.7$.

Obviously, the boundary-layer edge definition chosen for a Navier-Stokes calculation can significantly change crossflow Reynolds number results. Although it has been shown that the boundary-layer edge definition is important in calculating the

crossflow Reynolds number and estimating transition, the results presented do not help determine which edge definition is the most suitable. King [17] has previously performed a three-dimensional Navier-Stokes calculation for a two-dimensional nozzle. This investigation found that using equation 36, below, gave excellent results compared with results from a two-dimensional boundary-layer calculation. Results were also in agreement with experiments for δ^* but were not as accurate for θ.

$$po_{edge} = 0.98po_{max} + 0.02po_{wall} \tag{36}$$

where

po_{edge} Total pressure at the boundary-layer edge

po_{max} Maximum calculated total pressure

po_{wall} Total pressure at the wall

Referring to figure 16, it can be seen that the total pressure at the wall is only about 8% of the freestream value. Substituting this into the above equation and approximating the maximum total pressure as the freestream total pressure, the edge location is found to be approximately where the total pressure is 98% of the freestream value. Therefore, this is the definition that will be used for this investigation.

3.2   Short Mach 2.4 Nozzle Results

The results for the short Mach 2.4 nozzle are separated into two sections. First, a grid resolution study was performed to ensure that the calculated results are independent of the grid spacing. The second section then presents crossflow and transition results as well as other flow properties of interest.

3.2.1   Grid Resolution

The Mach number distributions along the centerline for the short Mach 2.4 nozzle for all grids and for the initial axisymmetric design are shown in figure 22. Good agreement exists between all solutions and the initial design. Therefore, in the streamwise direction, the coarse grid distribution should be all that is required to resolve
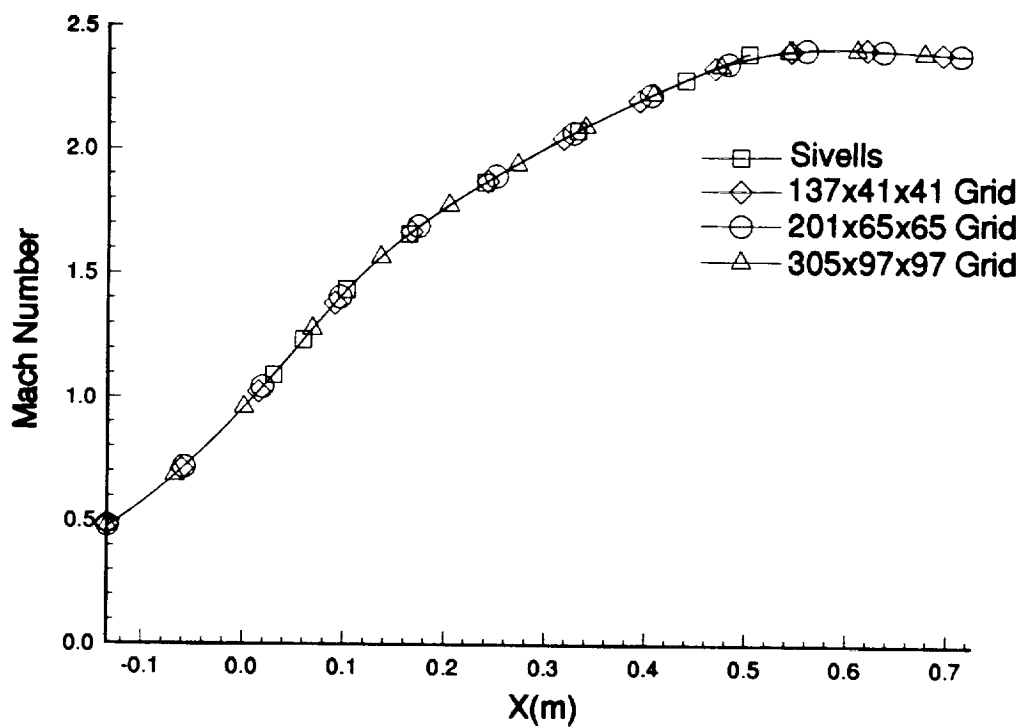
Figure 22-Mach Number Along Nozzle Centerline, All Grids and Axisymmetric Design
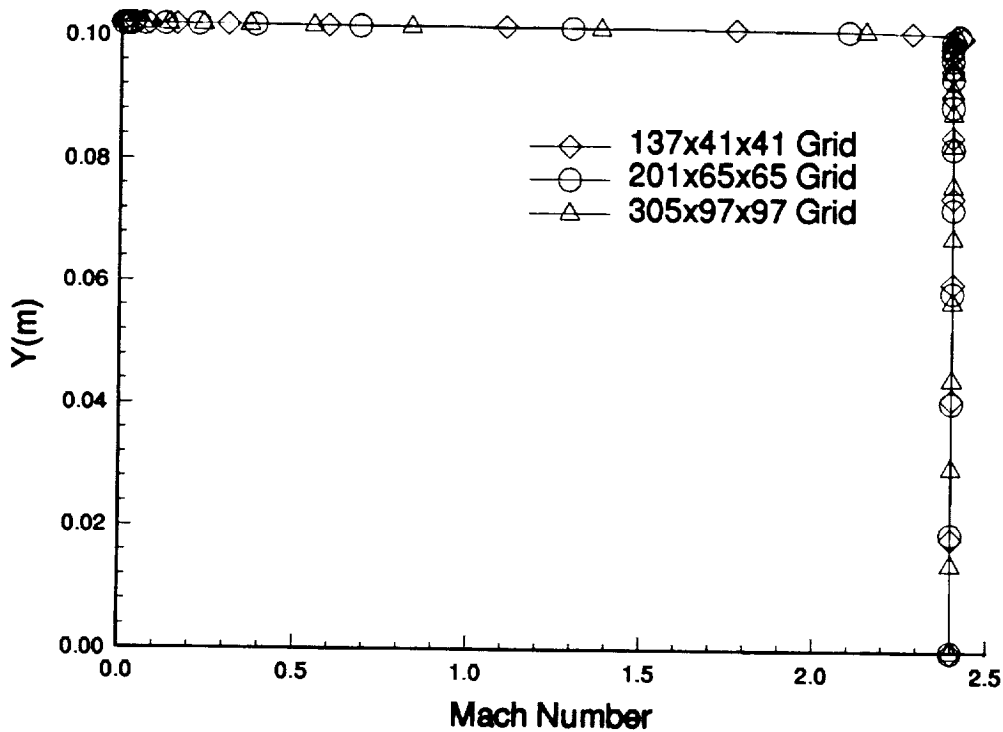
Figure 23-Mach Number Distribution at the Exit, in the Centerplane, All Grids
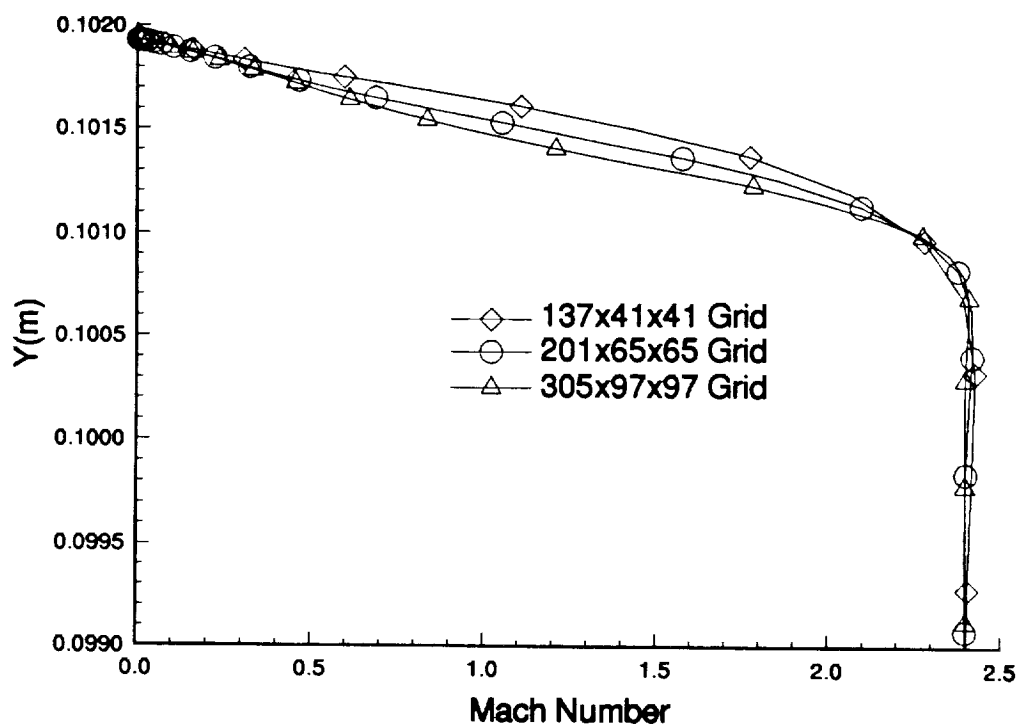
Figure 24-Mach Number Distribution Near the Wall in the Centerplane,
at the Exit, All Grids
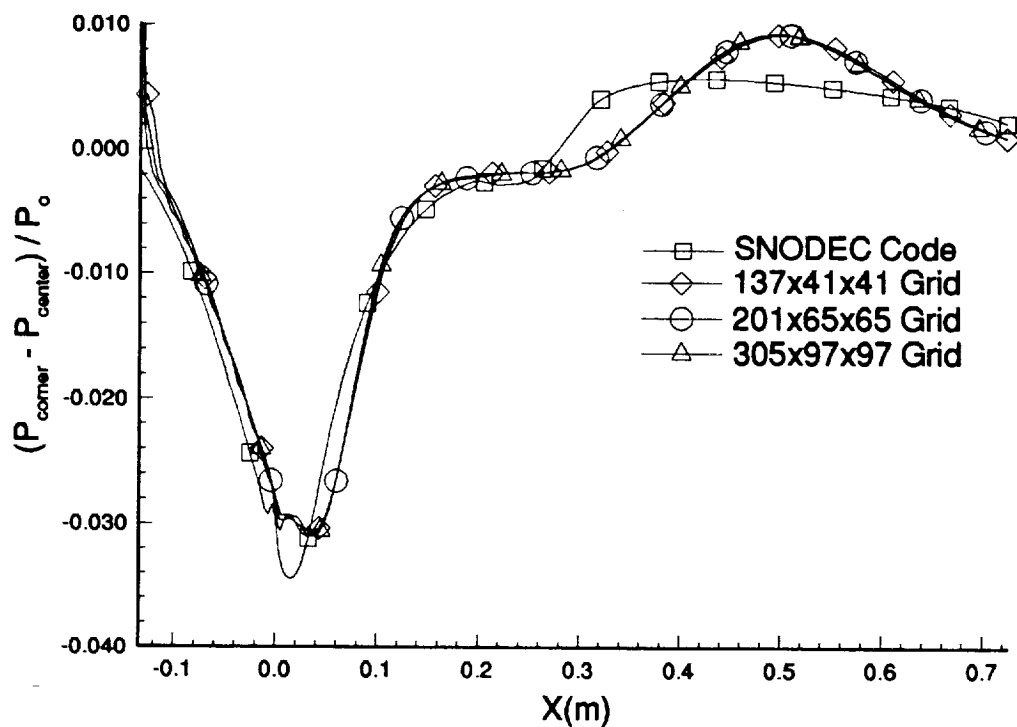
Figure 25-Pressure Difference Between the Corner and Centerplane,
All Grids and Inviscid Design

this portion of the flow. Figure 23 and 24 show the Mach number distribution at the centerplane, at the exit. In figure 23, it appears that there is good agreement between all solutions. However, figure 24 shows that in the boundary-layer region there is a discrepancy in the solutions. It can only be assumed that the fine grid gives the most accurate results, since further verification is not currently possible. Finally, in figure 25, the difference in pressure between the corner and the centerplane is shown for all three grids and the initial inviscid design. It can be seen that there is a good agreement between all three grids. However, the Navier-Stokes solutions do not agree very well with the inviscid design. This is most likely due to boundary-layer effects, such as crossflow and corner flow.

The displacement and momentum thicknesses were also computed along the centerplane, which are shown in figures 26 and 27. Both of these plots show a general agreement between the Navier-Stokes solutions up to approximately 0.5 meters downstream of the throat. At this point they diverge to a maximum difference at the exit. The table below gives the percentage difference from the finest grid for all the solutions and the two-dimensional boundary-layer results, at the exit:

Table #3 - Percent Difference in δ^* and θ from Finest Grid

	δ^*	θ
Harris Code	28.30	29.76
137x41x41	26.42	15.47
201x65x65	9.43	7.14
305x97x97	0.0	0.0

Again, it can only be assumed that the fine grid solution is the most accurate calculation. One possible reason for the differences could be variations in the resolution with which the crossflow is captured. To further investigate this, the streamwise and crossflow profiles were plotted at the exit, half-way between the centerplane and corner. These are shown in figures 28 and 29. Figure 28 shows the streamwise profiles. It can be seen that increasing the resolution makes the profile more shallow. The decrease in velocity in the streamwise direction is accompanied by an increase in crossflow as is
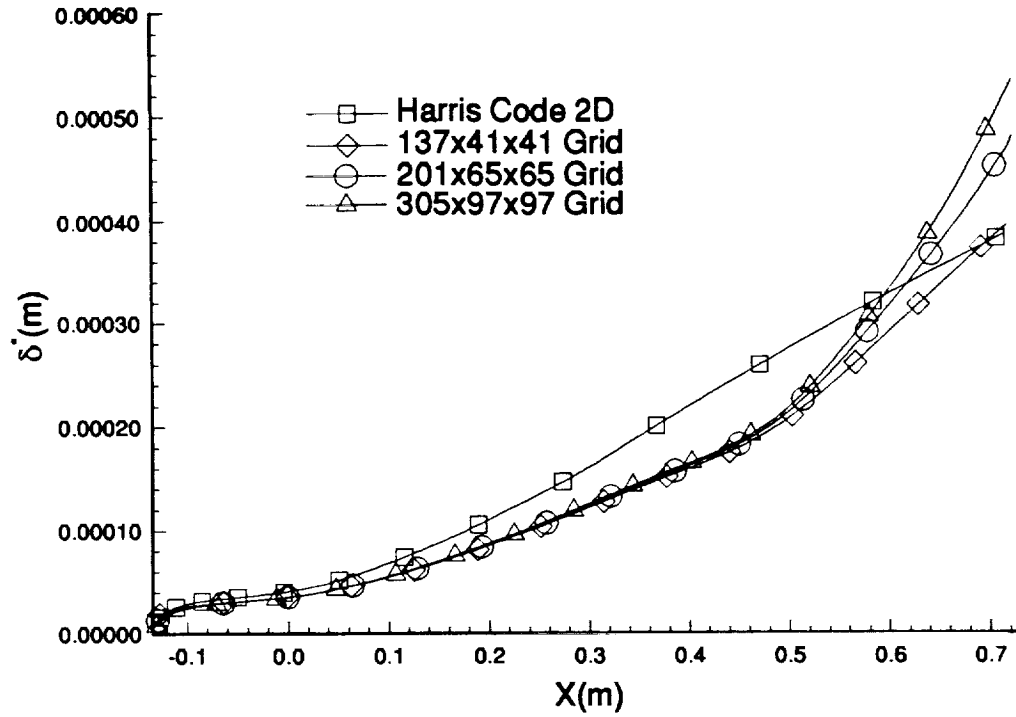
Figure 26-Displacement Thickness in the Centerplane, All Grids and
Two-Dimensional Calculation
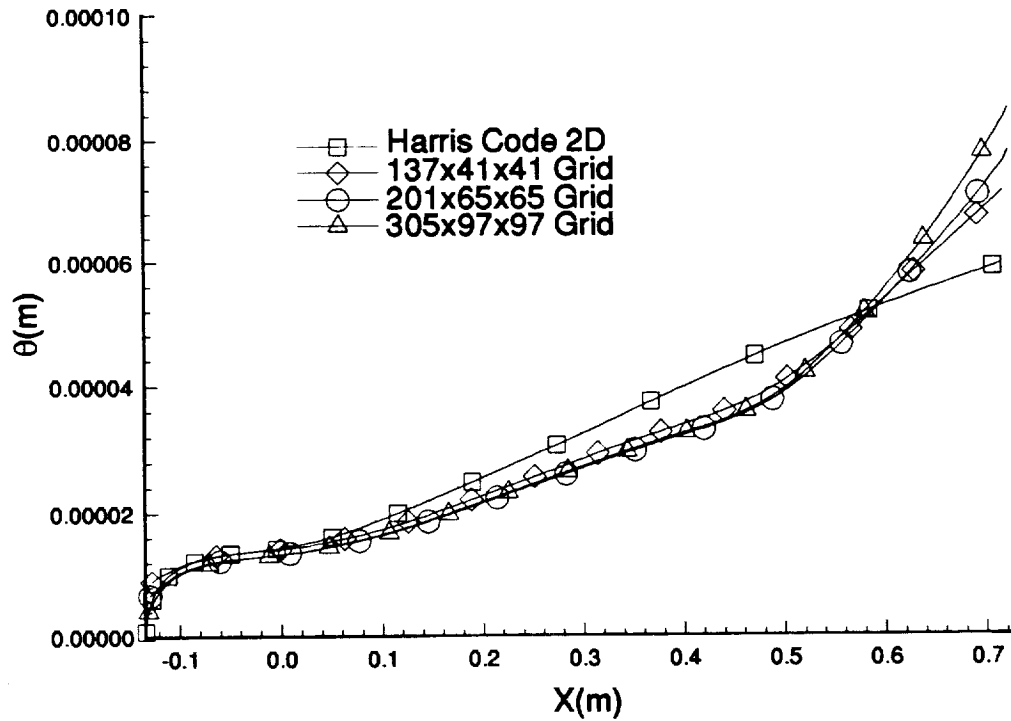
Figure 27-Momentum Thickness in the Centerplane, All Grids and
Two-Dimensional Calculation
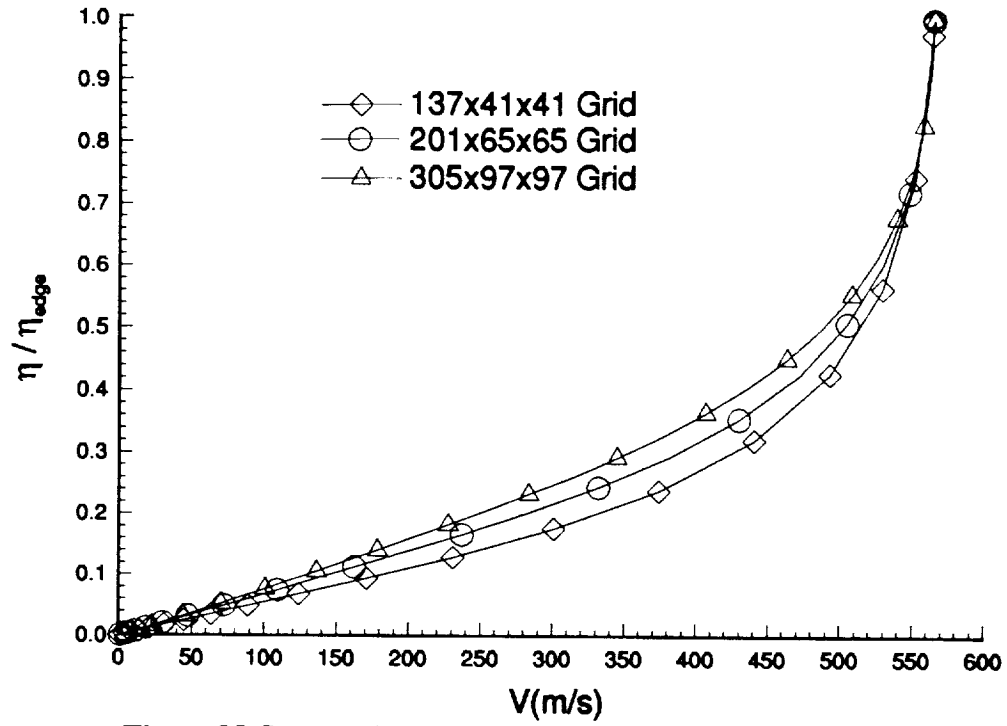
Figure 28-Streamwise Profiles at the Exit, Approximately Halfway
Between the Centerplane and the Corner, All Grids
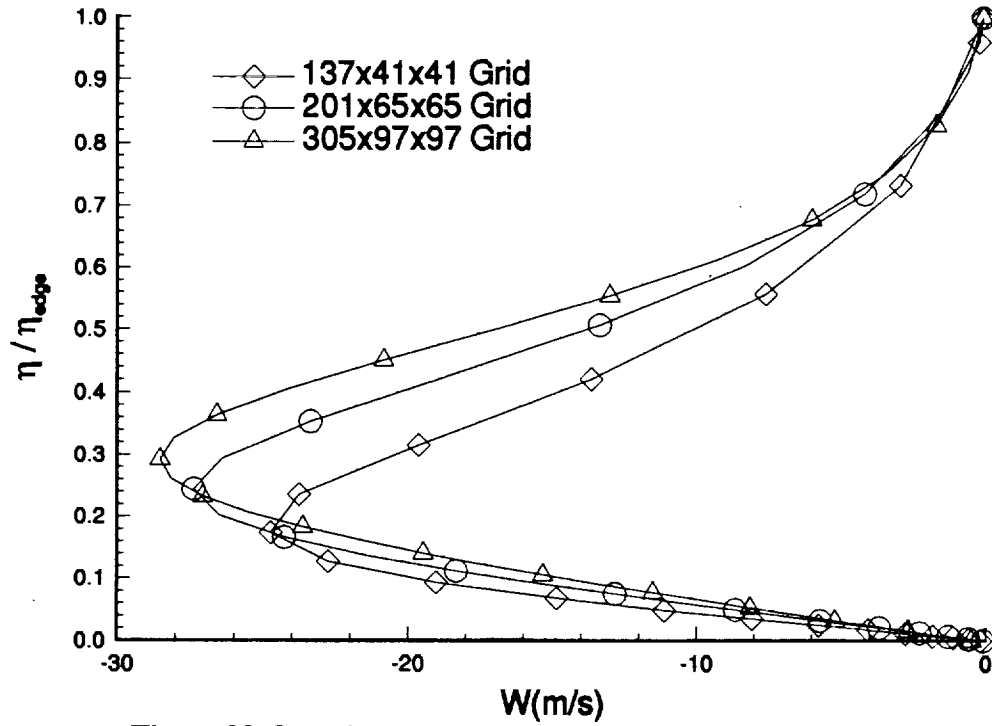
Figure 29-Crossflow Profiles at the Exit, Approximately Halfway
Between the Centerplane and the Corner, All Grids

shown in figure 29. This increase in crossflow will also increase the mass and momentum transfer from this location towards the centerline. Therefore, as the resolution is increased, the increase in mass and momentum transfer towards the centerline causes the higher displacement and momentum thicknesses seen in figures 26 and 27. It should also be noted that the differences in figures 28 and 29 correspond to the differences in Mach number near the wall that was shown in figure 24.

Two other points should be noted for figures 26 and 27. First, there is a relatively good agreement between all the grids and the two-dimensional results up to the throat region for both δ^* and θ. Using figure 30, it can be seen that crossflow plays a small role up to the throat region, and therefore, transfer of mass and momentum into the centerplane boundary-layer should be small. Therefore, the two-dimensional results should be in line with the three-dimensional results up to the throat. This signifies that using $P_o = 0.98 \, P_{oFS}$ was a good choice for the boundary-layer edge. Second, after the throat, the slopes of the lines for the computed δ^* and θ are smaller than the two-dimensional results up to x=0.5m. Since the crossflow is toward the corner in this region, mass and momentum are transferred away from the centerplane boundary-layer. This results in smaller growth rates for δ^* and θ than the two-dimensional results predict. At approximately x=0.5m downstream of the throat the slopes of these lines becomes greater than the two-dimensional results. Again using figure 30, it can be seen that this is the approximate location where the change in crossflow direction from towards the corner to away from the corner begins to effect the centerline boundary-layer. Opposite from before, mass and momentum are now being transferred into the centerline boundary-layer, causing larger growth rates for δ^* and θ than predicted by the two-dimensional results.

Figure 30 shows the maximum crossflow velocity (W_{MAX}) divided by the local edge velocity (U_e) in percentages. In each plot there is an unmarked line approximately half way between the throat and the exit. This is the interpolated location where the crossflow velocity changes sign from positive (towards the corner) to negative (away from the corner). In this region s-shaped profiles exist, which create a discontinuity in the crossflow Reynolds numbers. This will be discussed in more detail in the next section. It can also be seen that increasing the resolution increases the maximum crossflow velocity, assuming that the edge velocity is approximately constant at any given location. The medium and fine grids have approximately the same results with the major difference being the larger area in the fine grid calculation where W_{MAX}/U_e
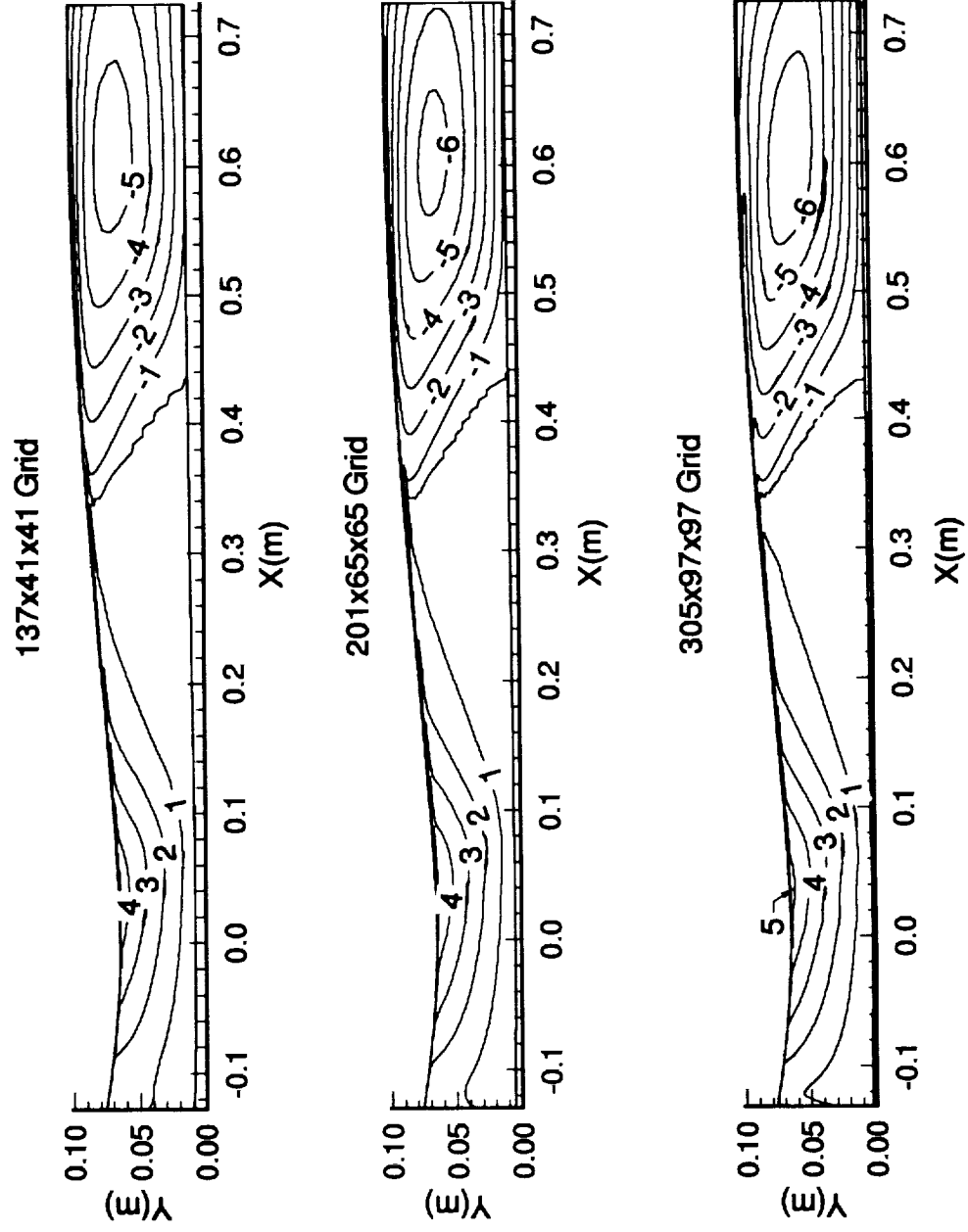
Figure 30-W_{MAX}/U_e in Percentages, All Grids
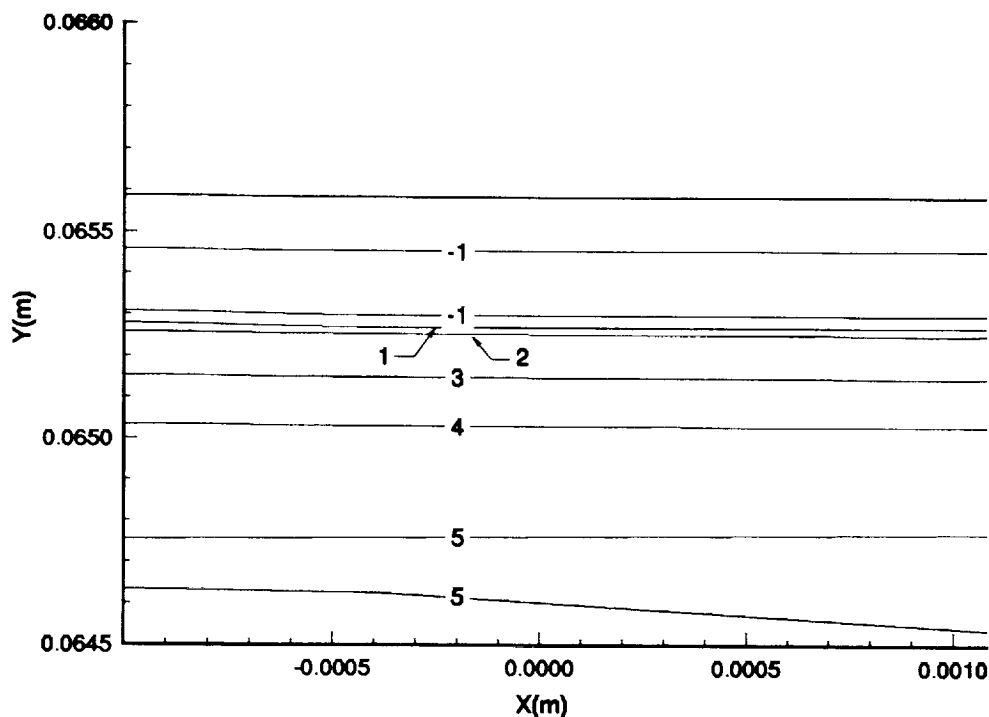
Figure 31-W$_{MAX}$/U$_e$ in Percentages Near the Corner, at the Throat

is -6%. The coarse grid, however, only reaches a maximum crossflow of -5% near the exit.

One further note should be made with respect to the throat data in figure 30. As can be seen in this figure, the crossflow appears to increase in magnitude into the corner. This should not occur, however, since the wall perpendicular to the crossflow should cause the crossflow to go to zero in the corner. To further investigate this, the contours have been magnified near the corner, in the throat region, for the medium resolution grid. This is shown in figure 31. This figure shows that the crossflow velocity does in fact decrease to zero and even reverses slightly as the corner is approached.

The various crossflow Reynolds numbers and transition estimation methods are plotted in figures 32-36. The meaning of these will be discussed in the next section and are presented here only to determine grid effectiveness in their calculation. In figure 32, it appears that increasing the resolution only increases the distinctiveness of the jump location created by the discontinuity in δ_{10}. Near the exit, the contour corresponding to

a crossflow Reynolds number of 2000 becomes more clearly defined with increasing resolution. This is most likely due to the increased resolution of WMAX seen in figure 30. The same trends are also seen for Reed and Haynes crossflow Reynolds number in figure 33. However, the values in the throat region change more rapidly than the standard crossflow Reynolds number does, and the contours also become more defined with increasing resolution. The changes near the throat for $R_{cfR\&H}$ must be due to changes in the compressibility factor since similar trends are not seen in figure 32. Finally, the crossflow Reynolds number developed by Beasley is seen in figure 34. This figure also shows the same trends that were seen in the standard crossflow Reynolds number. However, since this variable depends on the integral of the crossflow profile, the profiles seem less dependent on the resolution. Note that when the exit region is reached, the profiles becomes fuller with increasing resolution. These fuller profiles were seen in figure 29.

The transition estimation parameter R is shown in figure 35 for all grid resolutions. It can be seen in this figure that the medium and fine grids generally agree with the increase in resolution, only making the jump location more defined. However, the coarse grid does a poor job in the calculation of this parameter with respect to the other two resolutions. The streamwise shape factor is shown in figure 36 for all grid resolutions. There are discernible differences between all grids and especially between the coarse grid solution and the medium and fine grid solutions. These differences in streamwise shape factor are not surprising considering the differences in displacement thickness and momentum thickness shown in figures 26 and 27.

Since the coarse grid cannot accurately represent all parameters necessary for transition estimations, it cannot be used for these studies. The fine grid provides what are assumed to be the most accurate results, but is too costly in both memory requirements and run-time to allow repeated use. The medium grid will be used for the studies presented in this paper since the medium grid results are similar to the fine grid results. Clearly, the resolution is insufficient for stability calculations. However, the resolution seems more than sufficient for preliminary investigation using the crossflow Reynolds numbers, since they are fairly consistent.
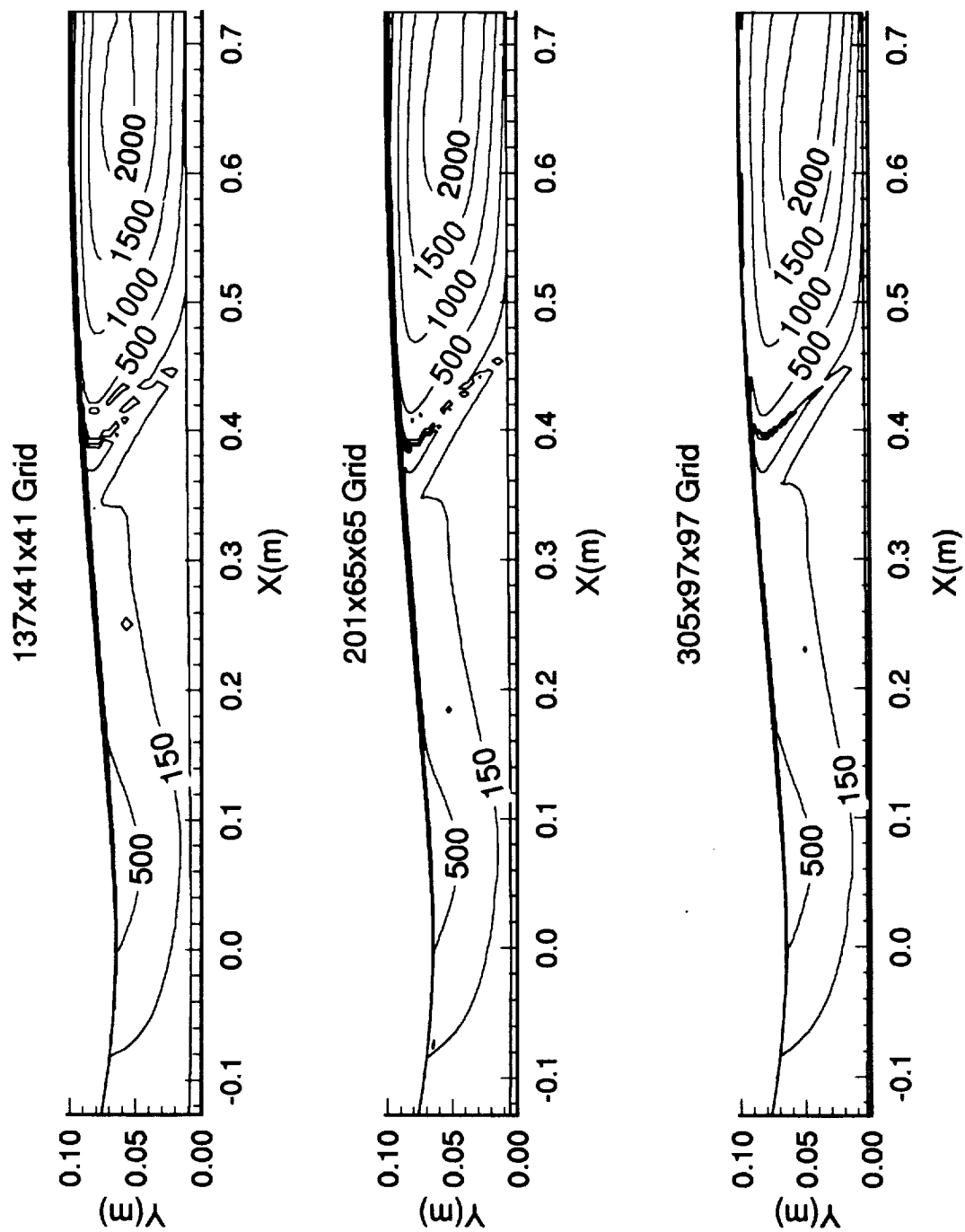
Figure 32-Standard Crossflow Reynolds Number, All Grids
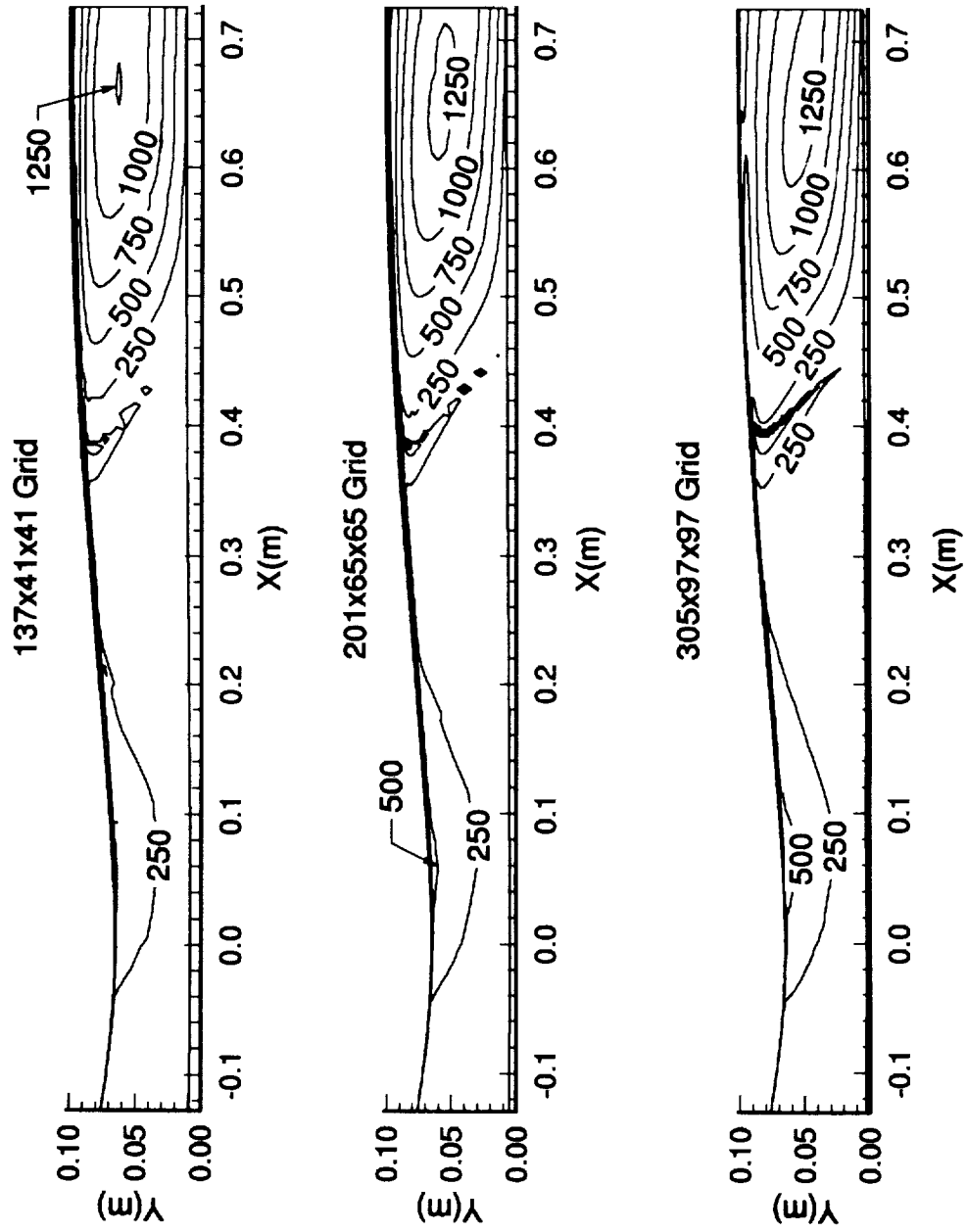
Figure 33-Reed and Haynes Crossflow Reynolds Number, All Grids
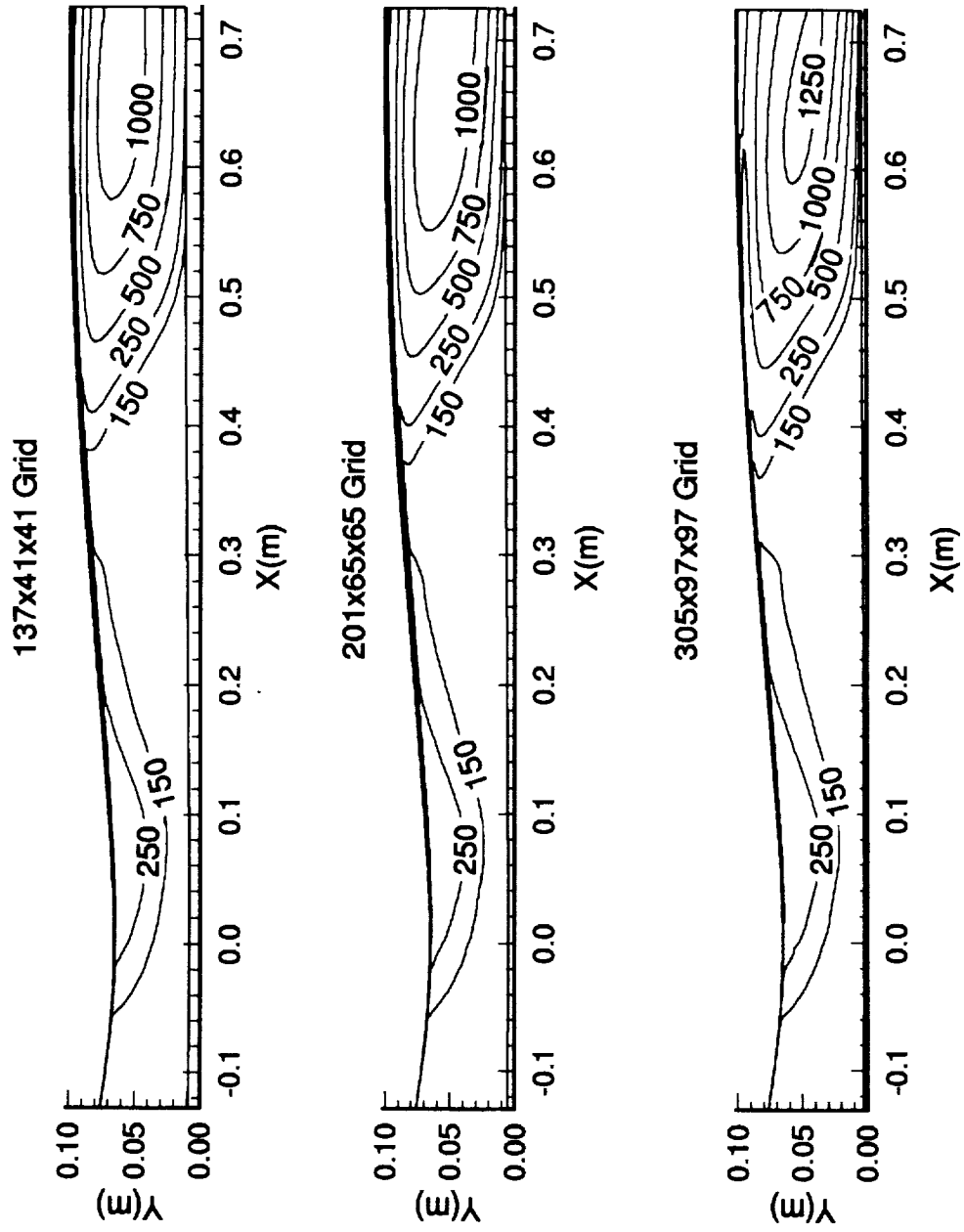
Figure 34-Crossflow Reynolds Number of Beasley, All Grids
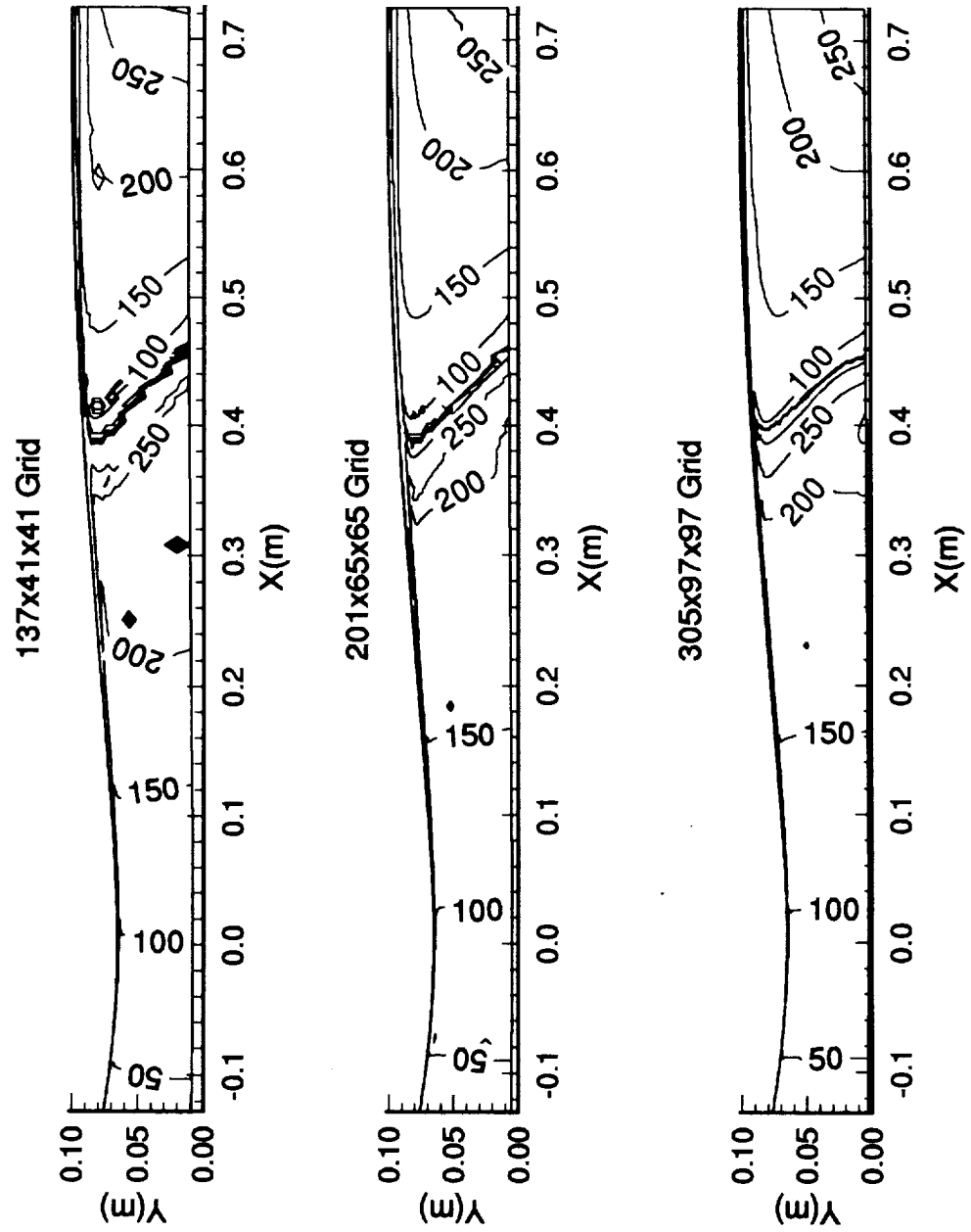
Figure 35-Reed and Haynes Transition Estimator, R, All Grids
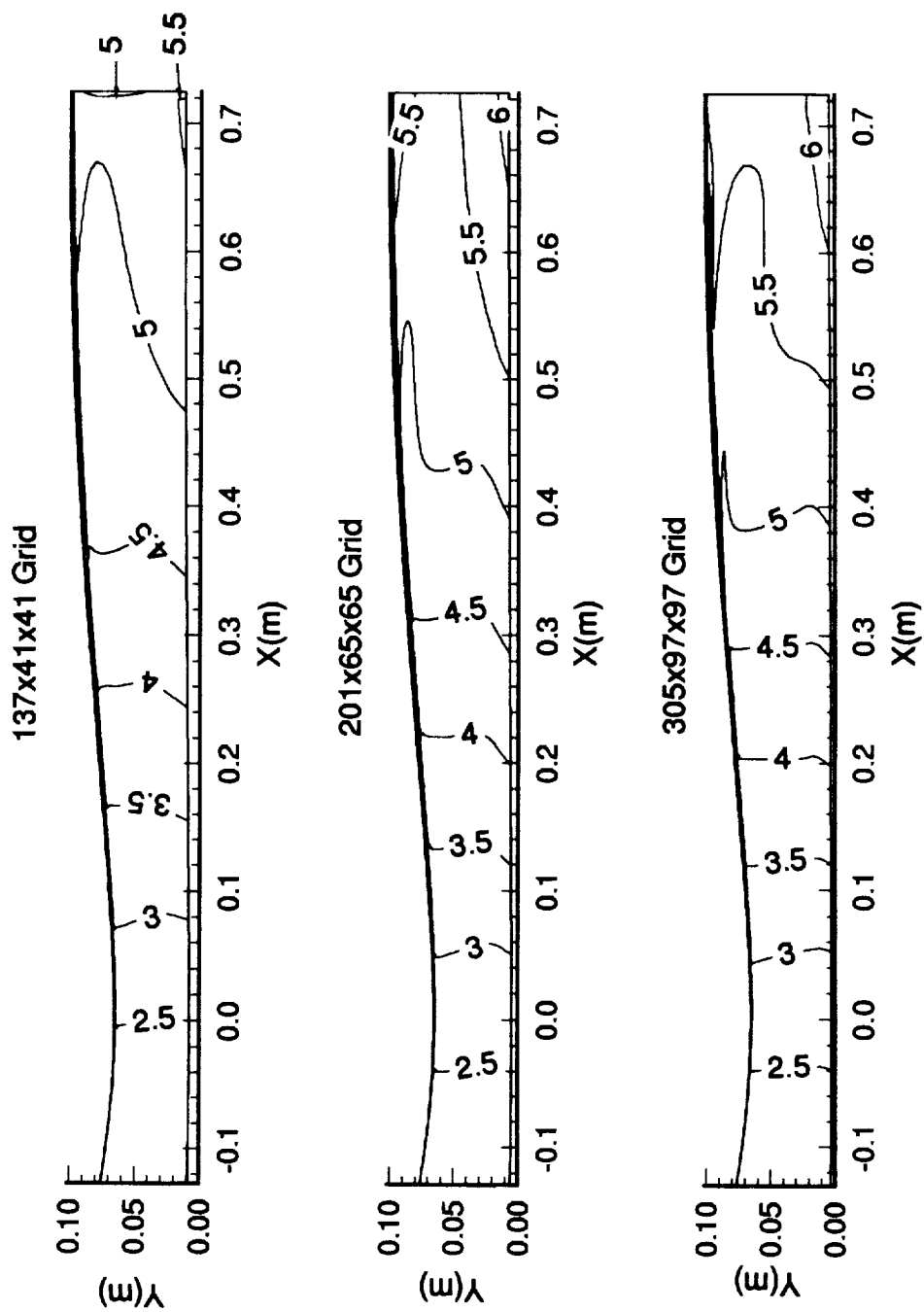
Figure 36-Streamwise Shape Factor, All Grids

3.2.2 Results

After the Navier-Stokes solution was complete, the Mach contours were plotted in both the centerplane and the cornerplane. This can be seen in figure 37. It can be seen that the test rhombus is fairly uniform with a maximum deviation of +0.017 from the test Mach number of 2.4. The Mach number in the exit plane is then plotted in figure 38. This plot shows that the Mach number at this location is also very uniform with the maximum deviations being ±0.0025 from the design Mach number of 2.4. A small corner flow region should also be noted which contains about 3% of the total wall length. Figure 39 shows the v and w velocity vectors in this corner region. As can be seen, two counter-rotating vortices are present. This is most likely the early stages of the large counter-rotating vortices that were present in the hypersonic rapid-expansion nozzles investigated in reference 47. It is possible that these vortices will cause transition near the corner of the nozzle. However, because of their relatively small size and the fact that the maximum velocity is only around 1% of the u-component of the velocity, these vortices are not likely to dominate the transition.

Flow in the corner of these nozzles is complex and three-dimensional, and the crossflow Reynolds number techniques are not applicable. Therefore, the physical limits for using the crossflow Reynolds numbers must be set before a quantitative analysis can be completed. To accomplish this, the boundary-layer thickness has been plotted from the centerplane into the corner at both the throat and the exit. These are shown in figures 40 and 42. Figure 40 shows that in the nozzle throat, the boundary-layer remains fairly constant up to about 0.0013m from the wall. The thickness suddenly jumps after this point. A close-up of just the jump region is shown in figure 41. This plot shows that there is a distinct increase in the boundary-layer thickness at y=0.0014m from the corner. At this point, the corner flow region is entered and the crossflow data is no longer useful. To further see this, the boundary-layer in the exit plane is shown in figure 42. The figure shows that the boundary-layer at the exit grows until a jump again occurs where the boundary-layer becomes much thicker. Figure 43 shows a close-up of this region where it can be seen that the boundary-layer thickness increases by approximately an order of magnitude when the corner region is entered. To show that this jump is created by the flow in the corner, figure 44 shows total pressure contours near the corner region. As can be seen, the boundary-layer is found to be approximately constant up to the point labeled "jump location". After this point, the corner flow properties take-over and the crossflow Reynolds numbers are no longer valid. Note that the point labeled "jump location" is at approximately 0.0035m from the

Figure 37-Mach Contours in the Centerplane and Cornerplane
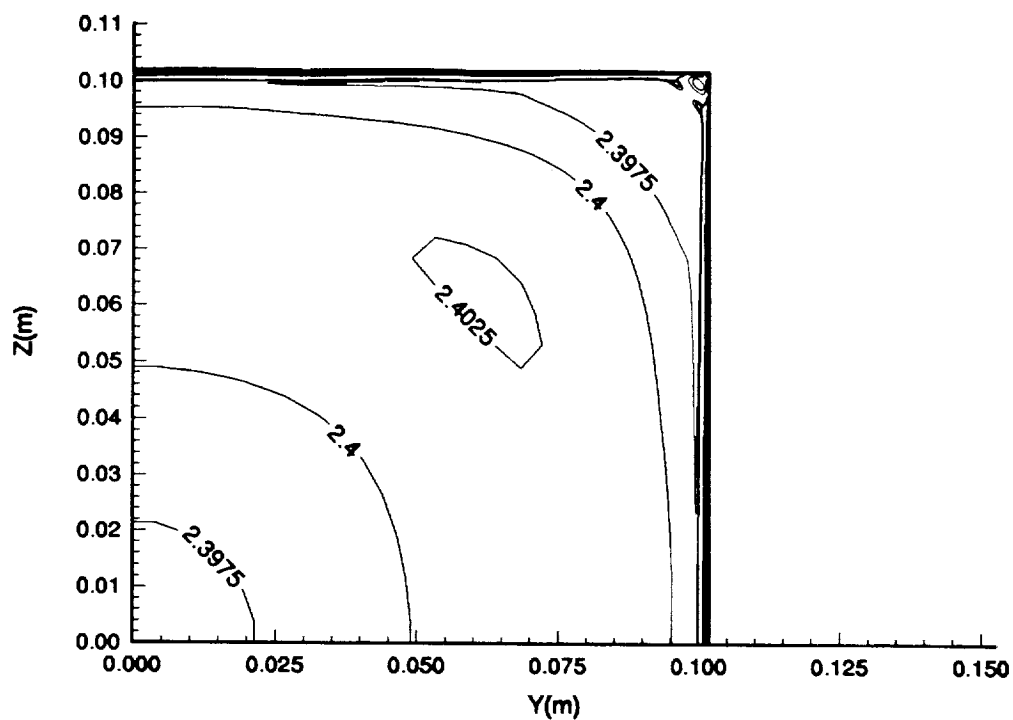
Figure 38-Mach Contours at the Exit
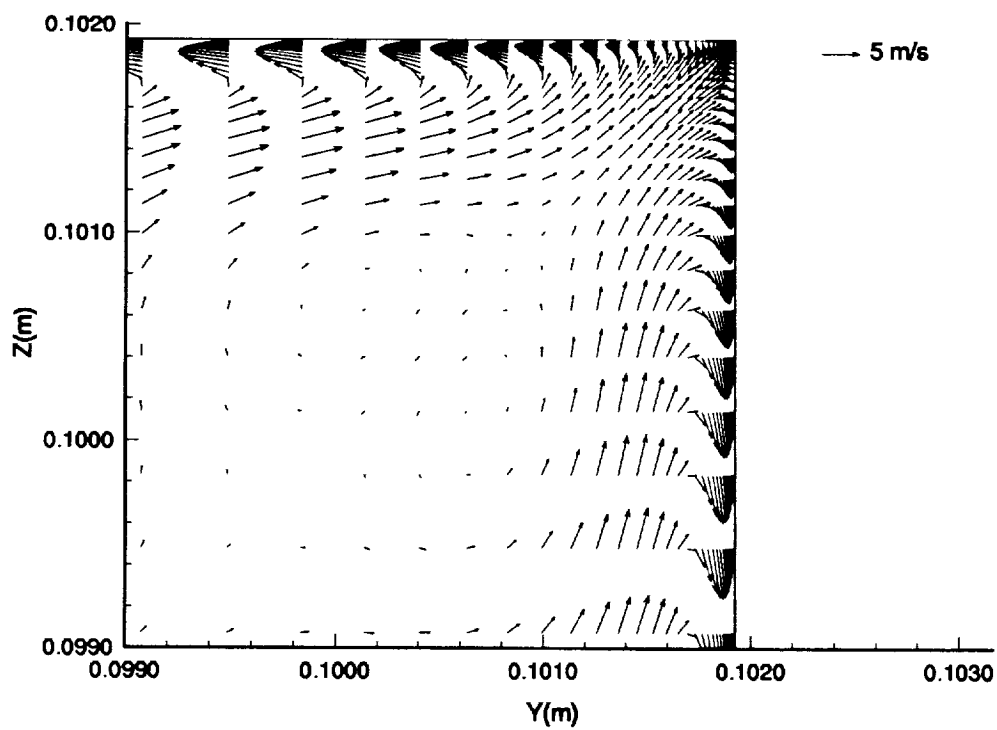
Figure 39-V and W Velocity Vectors in the Corner at the Exit
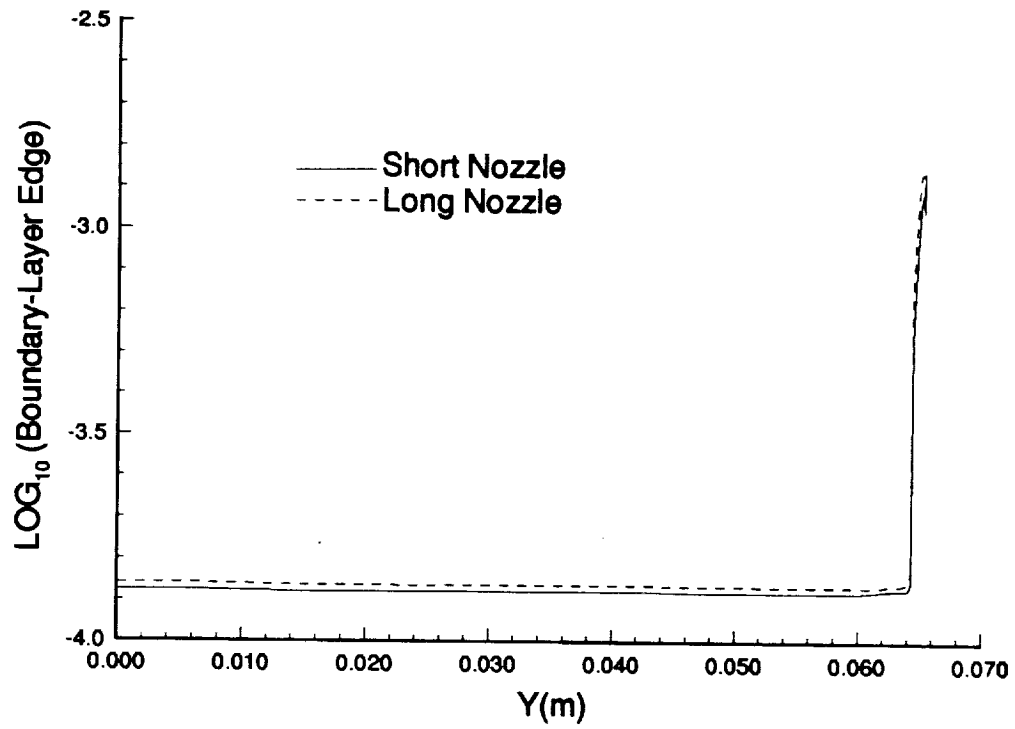
Figure 40-Boundary-Layer Edge, Across the Throat
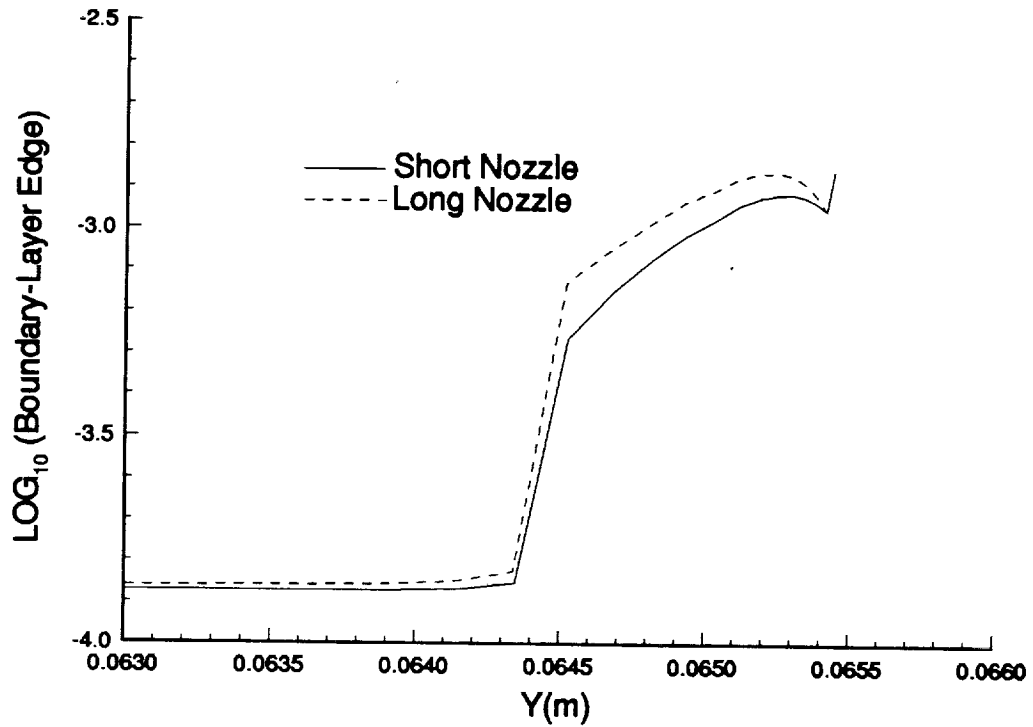
Figure 41-Boundary-Layer Edge in the Throat, Near the Corner

C-2
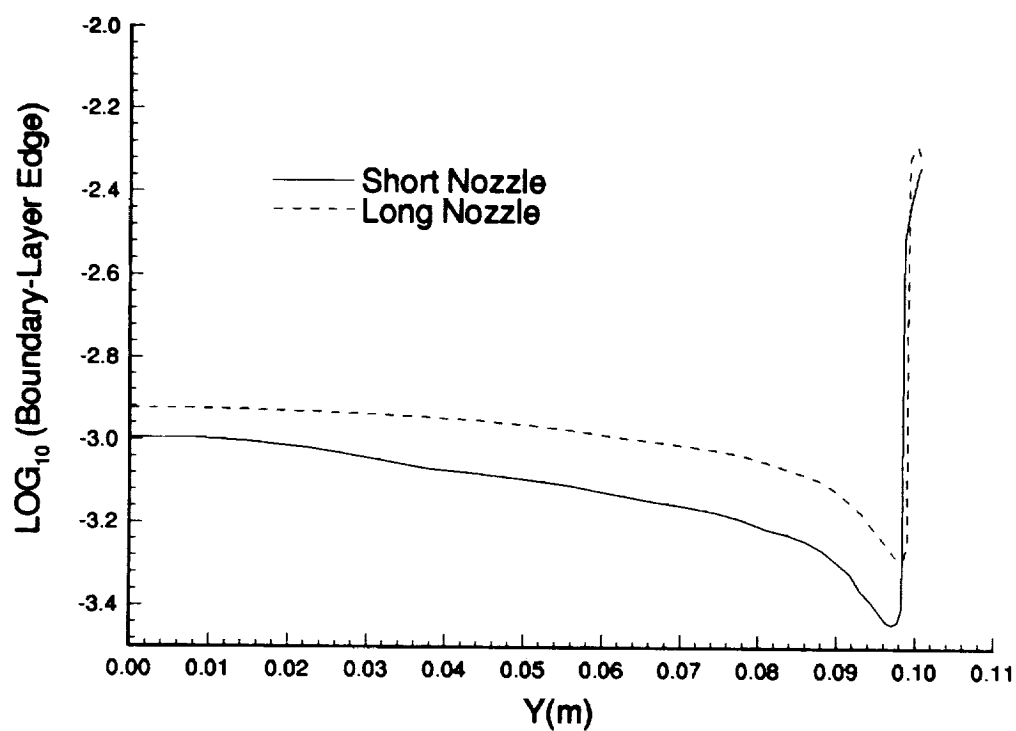
Figure 42-Boundary-Layer Edge, Across Exit
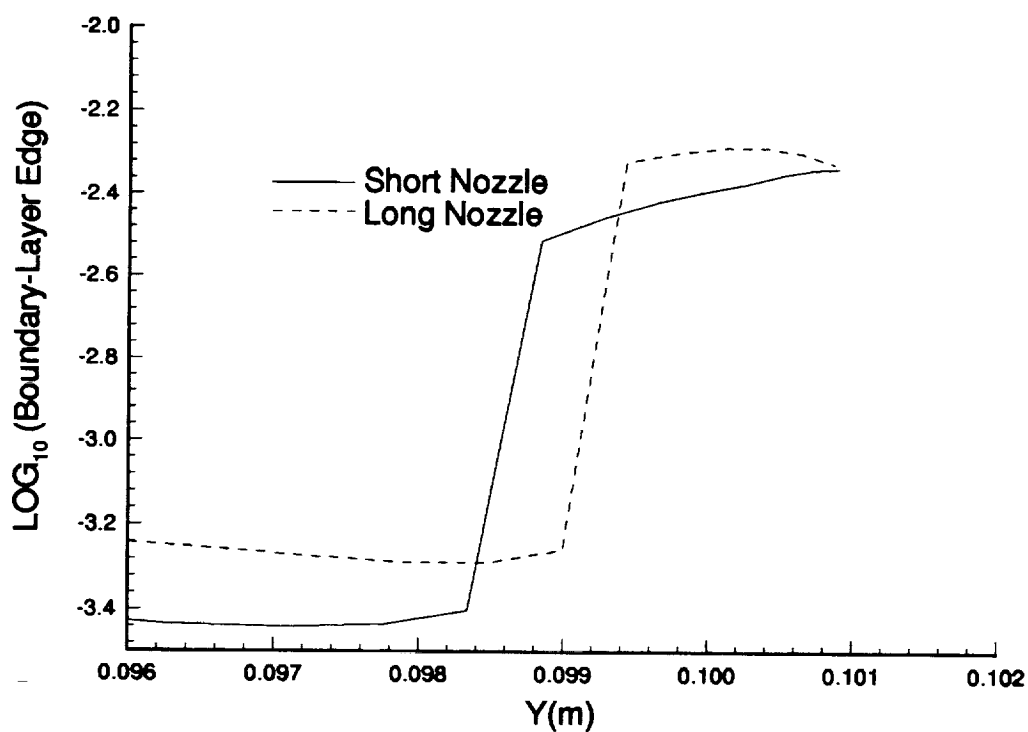
Figure 43-Boundary-Layer Edge at the Exit, Near the Corner
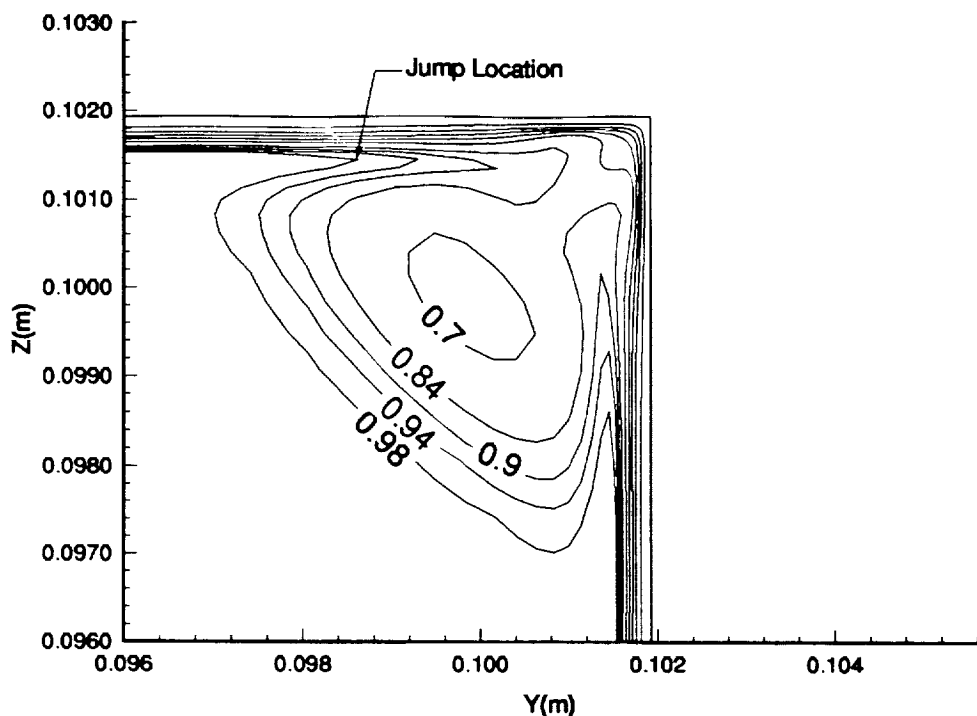
Figure 44-Total Pressure Contours at the Exit, in the Corner

corner, the same location where the discontinuity occurs in the data of figure 43. The limits for the crossflow calculations in the short Mach 2.4 nozzle were taken to be 0.0014m from the corner in the throat and 0.0035m from the corner at the exit.

As mentioned in the previous section, there exists a region in these nozzles where the crossflow changes sign from positive to negative. Figures 45 and 46 show streamwise and crossflow profiles from x=-0.927 into the nozzle exit, along with the line along which the profiles were taken. It can be seen in figure 45 that the streamwise profiles generally increase in magnitude until approximately 0.4 meters downstream of the throat. At this location, the streamwise velocity becomes approximately constant to the exit. In figure 46, it can be seen that the crossflow is positive (towards the corner) until somewhere between x=0.3 and x=0.4 meters downstream of the throat, where the profiles undergo a change in direction. To better see this, figure 47 shows the profiles through this region. Note that the profiles are plotted at intervals of $\Delta x = 0.00658$m. Since both R_{cf} and $R_{cfR\&H}$ are dependent on the maximum value of the crossflow and the location where the crossflow decreases to 10 percent of the maximum value (δ_{10}), the calculation of these parameters in this region is difficult. The following definition

has been chosen for this region: after W_{MAX} is found, the location for δ_{10} is taken to be the furthest point from the wall where the magnitude of the crossflow is 10 percent of the maximum. As can be seen in figure 47, the initial crossflow profile shown is entirely in one direction. Then, moving downstream, the crossflow begins to change direction near the wall while continuing to slow down near the edge. As this happens, W_{MAX} decreases to a minimum and then begins to increase again. Since δ_{10} is defined to be the furthest distance away from the wall, this parameter will continue to increase until the maximum value is reached at point A in figure 47. After this point, the crossflow in the top half of the s-profile is always less than 10 percent of W_{MAX}. Therefore, the distance δ_{10} will suddenly jump to point B shown on figure 47. This then causes the discontinuity seen in the crossflow Reynolds numbers.

The crossflow Reynolds number contours as well as the transition estimation criteria are shown in figures 32-36 along half of any nozzle wall. The standard crossflow Reynolds number, plotted in figure 32, shows two regions where transition may occur. The first, and most significant, is near the exit, where R_{cf} increases from approximately 150 to more than 2000 over the range of about 0.16m. The maximum crossflow Reynolds number attained is almost five times as large as the estimated critical value of 430. It is thus likely that transition will occur before the exit. The second region is that near the throat. Although a maximum of slightly more than 500 is attained in this region, the estimated transitional value of 240 is approximately 1/2 of the calculated value. Therefore, it is likely that transition will occur near the nozzle throat, according to this method.

Figures 33 and 35 show the Reed and Haynes crossflow Reynolds number and the transition estimator R. It can be seen in figure 33 that, like R_{cf}, there is a region near the exit where the values change from about 250 to about 1250 over a region of approximately 0.16m. A region of lesser values also exists in the throat, like those seen previously. The values for R shown in figure 35 give the same general conclusions as the standard crossflow Reynolds number. After the observed jump region between x=0.4m and x=0.5m, the maximum values for R increase to more than 250. This is more than 5.5 times greater than the value of 44 estimated for transition on spinning and yawed cones [39]. Again, transition appears likely before the exit. Near the throat, the values for R become 2 to 3 times as great as the estimated transitional value. However, referring back to figure 30, this method can only be used in the small region where W_{MAX}/U_e is greater than 2% to be within the lower limits for this correlation. Still, this method predicts that there is a good possibility that the flow will transition in the

Figure 45-Streamwise Profiles and Line Along Which They are Taken
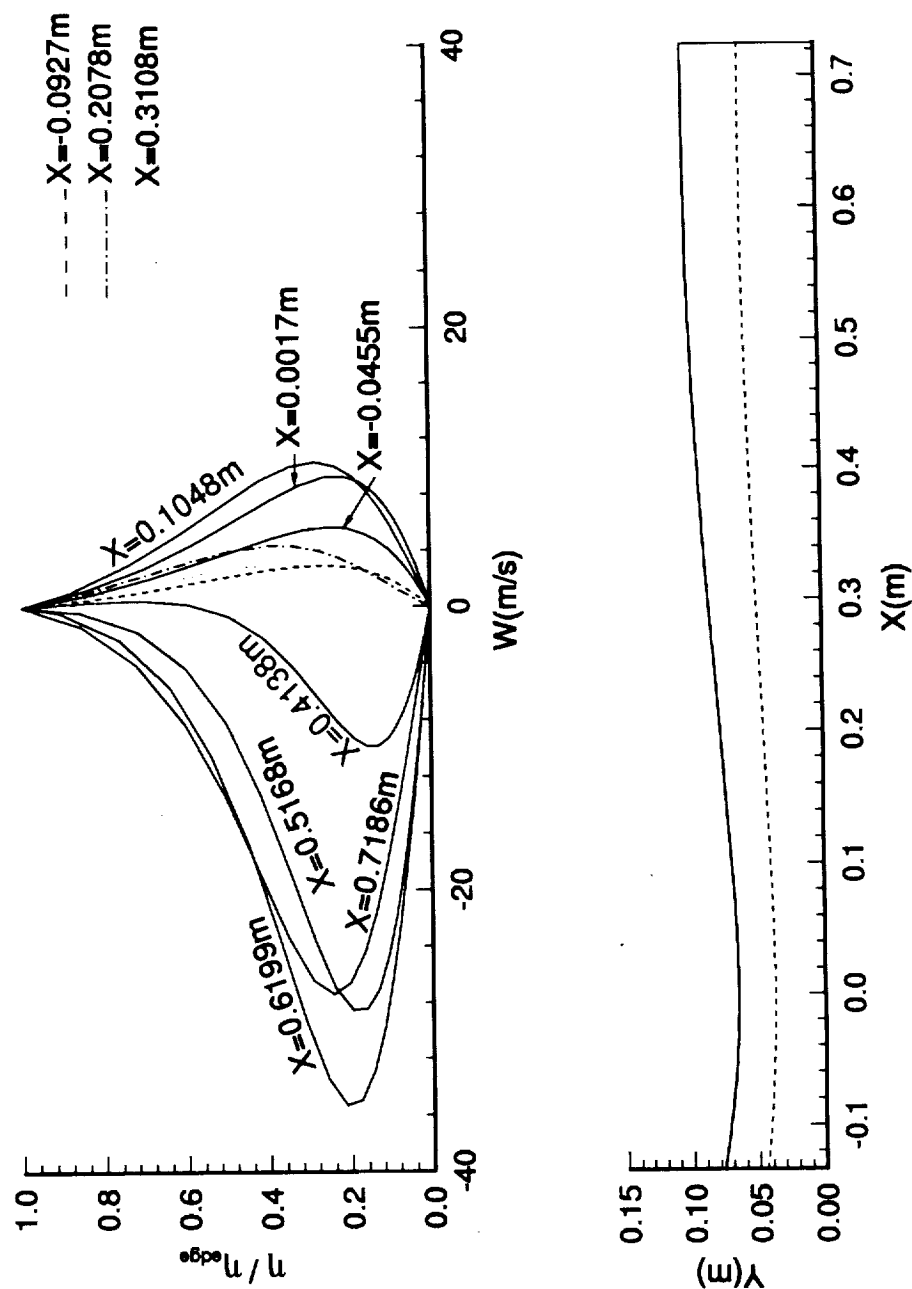
Figure 46-Crossflow Profiles and Line Along Which They are Taken
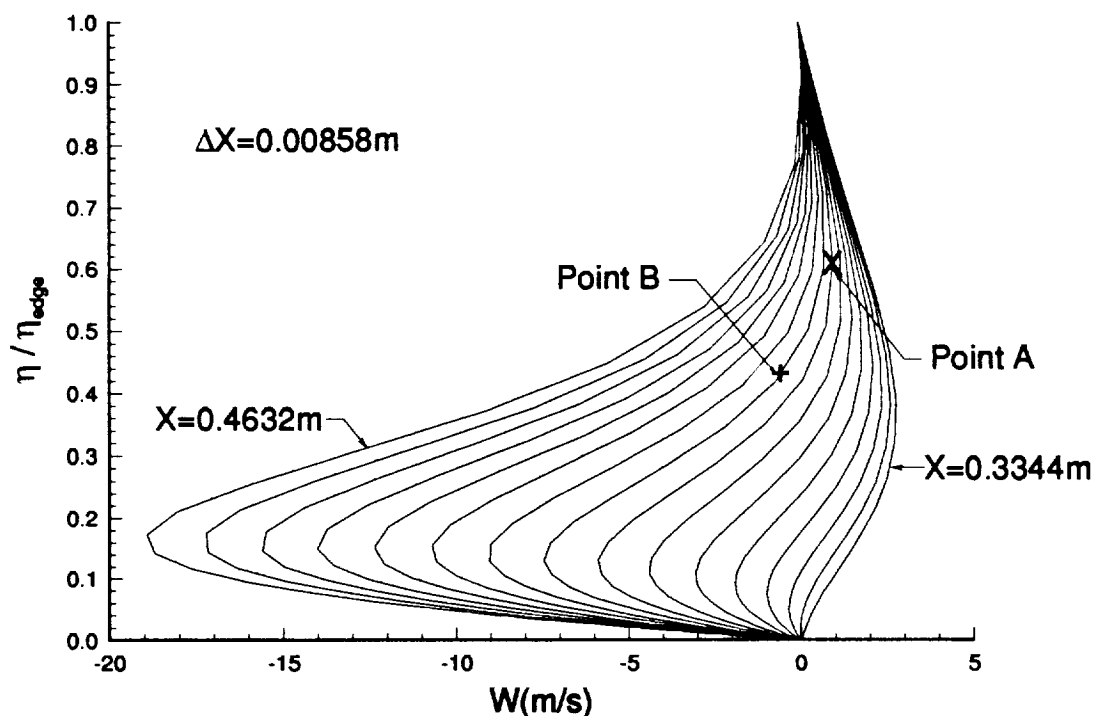
Figure 47-Crossflow Profiles Through S-Shaped Region

throat region.

Finally, figures 34 and 36 show $R_{\delta 2}$ and the streamwise shape factor respectively. Figure 34 shows the same trends that were evident in the other two crossflow Reynolds numbers. A comparison of figure 34 with figure 33 reveals that the crossflow Reynolds number developed by Beasley produces approximately the same results as Reed and Haynes crossflow Reynolds number. Examination of the streamwise shape factor shows that this method estimates transition as soon as $R_{\delta 2}$ reaches a value of 150. It is evident that transition will occur in the throat for this method. Since the limit on the streamwise shape factor is $2.3 < H_{shp} < 2.7$, this method cannot be applied anywhere downstream of the throat. Therefore, no conclusions can be drawn from this method downstream of the throat area.

Even taking into consideration the large discrepancies that may exist in these methods, there is little doubt that crossflow induced transition will occur in this nozzle. The table below shows the estimated transition location for each method both near the throat and near the exit. The transition estimates are those presented in the preceding paragraphs where the locations used are the first streamwise locations where any point

is greater than the transition estimate.

Table 4-Transition Estimates for the Short Mach 2.4 Nozzle

Method	Location Near Throat	Location Near Exit
R_{cf}	X=-0.045m	X=0.42m
$R_{cfR\&H}$	X=-0.1m	X=0.4m
$R_{\delta}2$	X=-0.05m	Inapplicable

Clearly, the first and third method approximate transition at the same location near the throat while Reed and Haynes is not as close. However, Reed and Haynes estimation was taken from the lower end of the range on W_{MAX}/U_e and therefore, may not be reliable. Near the exit, the first and second method estimate transition in about the same location while nothing can be said about the third technique. It should be noted that the transition locations reported first occur near the corner for all cases.

Even though transition is likely in the throat region, the likelihood is greater that transition will occur near the nozzle exit. If only the results near the exit are considered, a simple preliminary analysis of quiet-test length for the nozzle can be performed. Figure 37 shows the Mach contours for the short nozzle in both the centerplane and cornerplane. From this it can be seen that the test rhombus starts at approximately x=0.52m. If a characteristic is drawn beginning from the reported transition location above, in the cornerplane plot in figure 37, whose slope is equal to the average Mach number though which the characteristic travels, the quiet-test length was found to be approximately 0.17m. This then gives a quiet-test Reynolds number ($R_{\Delta x}$) of 1.2 x 10^7. This is comparable to other quiet-flow nozzles in use today [23].
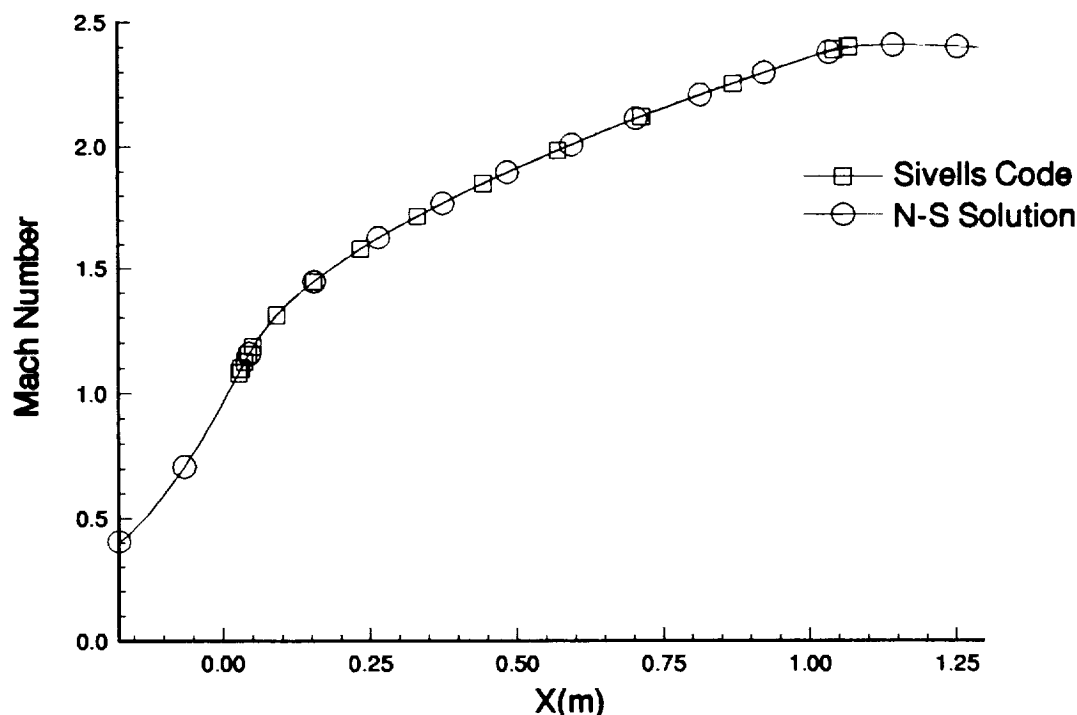
Figure 48-Mach Number Along the Centerline, Navier-Stokes Solution and Axisymmetric Design

3.3 Long Nozzle Results and Comparisons

A simulation was then performed on the long nozzle case using a 201x65x65 grid with the same stretching used in the previous case. Since the exit dimensions and throat dimensions are the same, using the same number of points and the same stretching should give reasonably accurate results normal to the streamwise direction. However, since this nozzle is almost twice as long as the previous one, using 201 points in the streamwise direction yields almost twice as much distance between grid points. This spacing is only 17 percent larger than the coarse grid in the previous example, however, which had good accuracy in the streamwise direction. Therefore, it will be assumed that this distribution is accurate enough for this investigation. To verify this assumption, the centerline Mach number is plotted for both the Navier-Stokes solution and the original design in figure 48. It can be seen that there is good agreement between the original design and the final solution signifying that this spacing is adequate. A further grid refinement study will be needed if further analysis is to be done on this design.
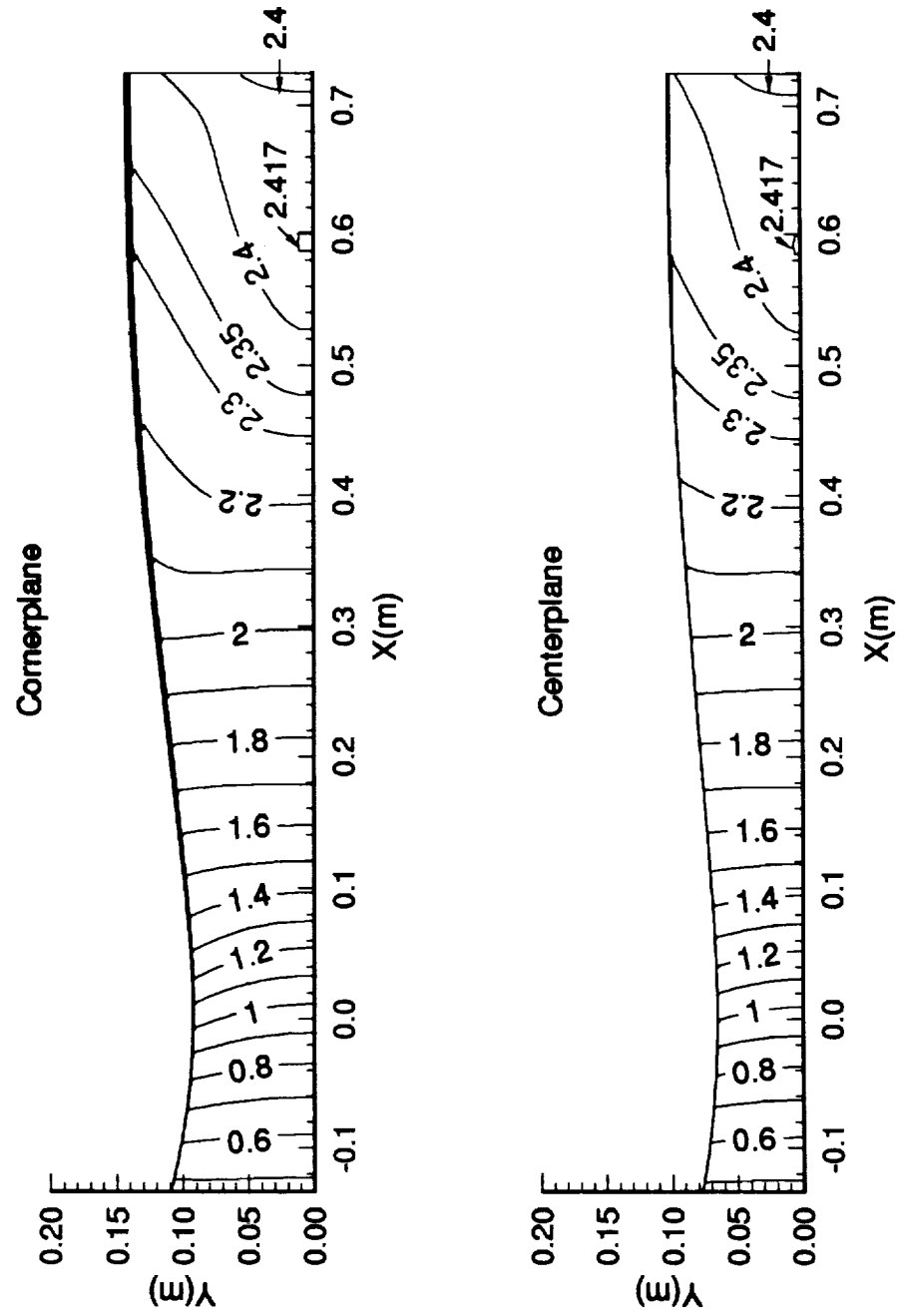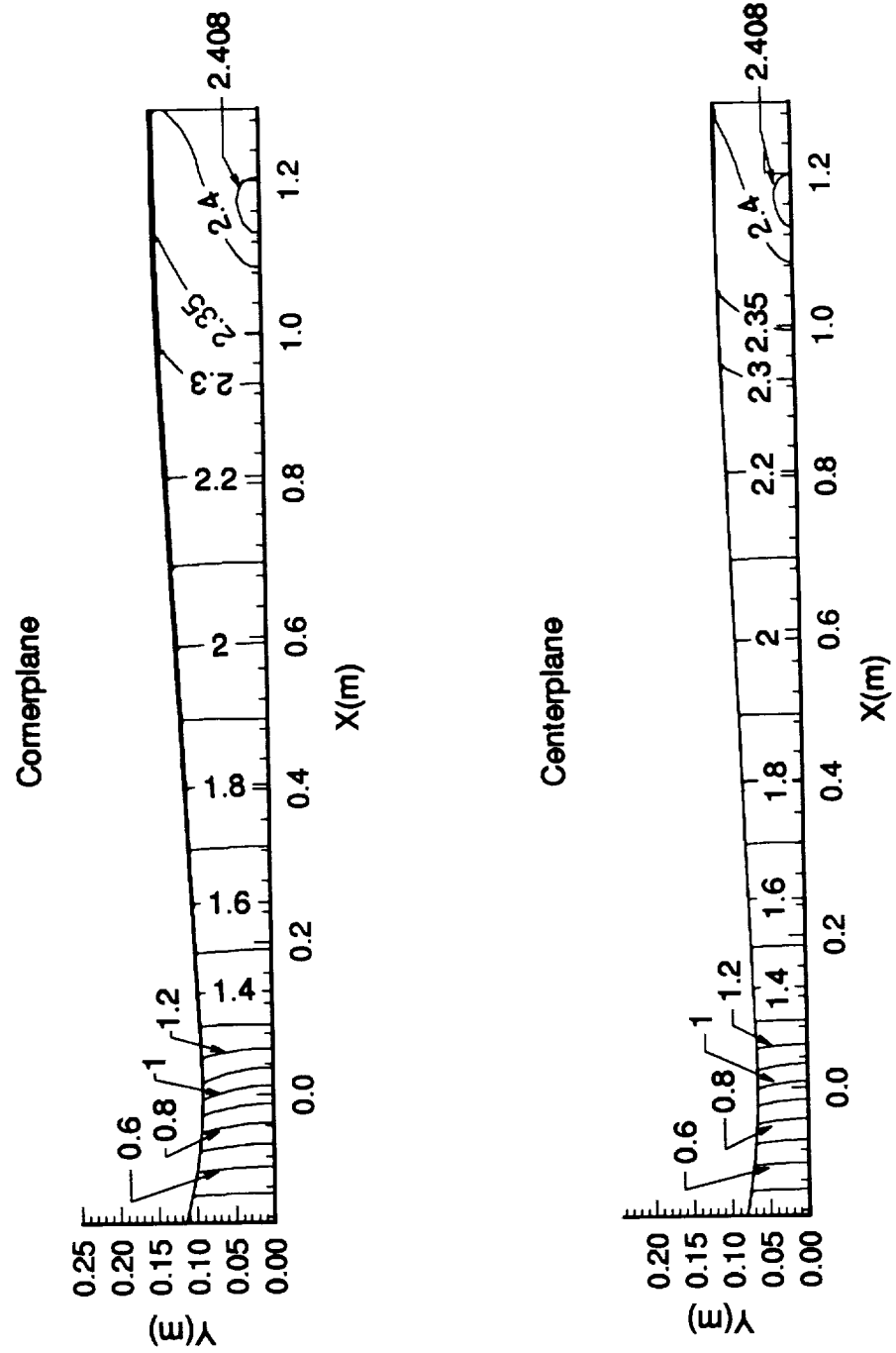
Figure 49-Mach Contours in the Centerplane and Cornerplane
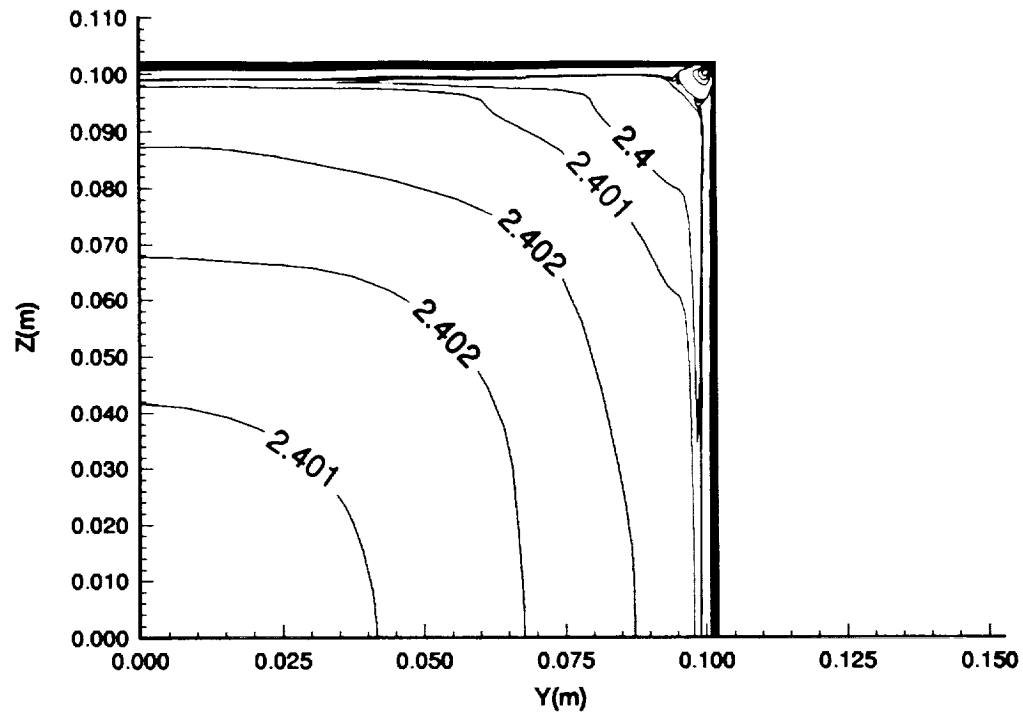
Figure 50-Mach Contours at the Exit
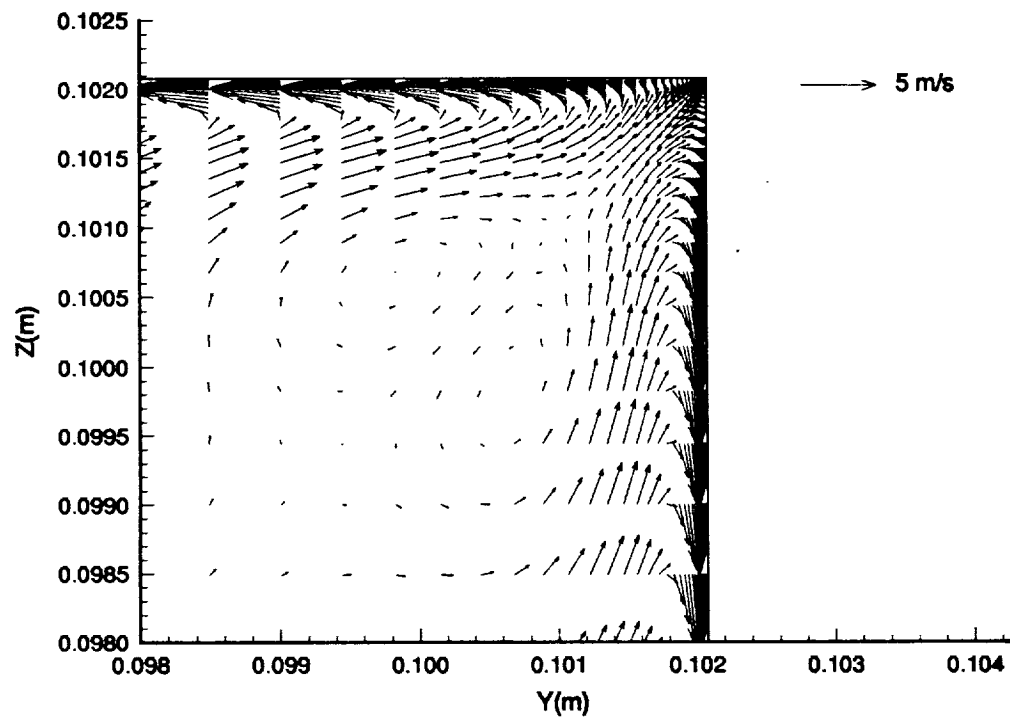
Figure 51-V and W Velocity Vectors in the Corner at the Exit
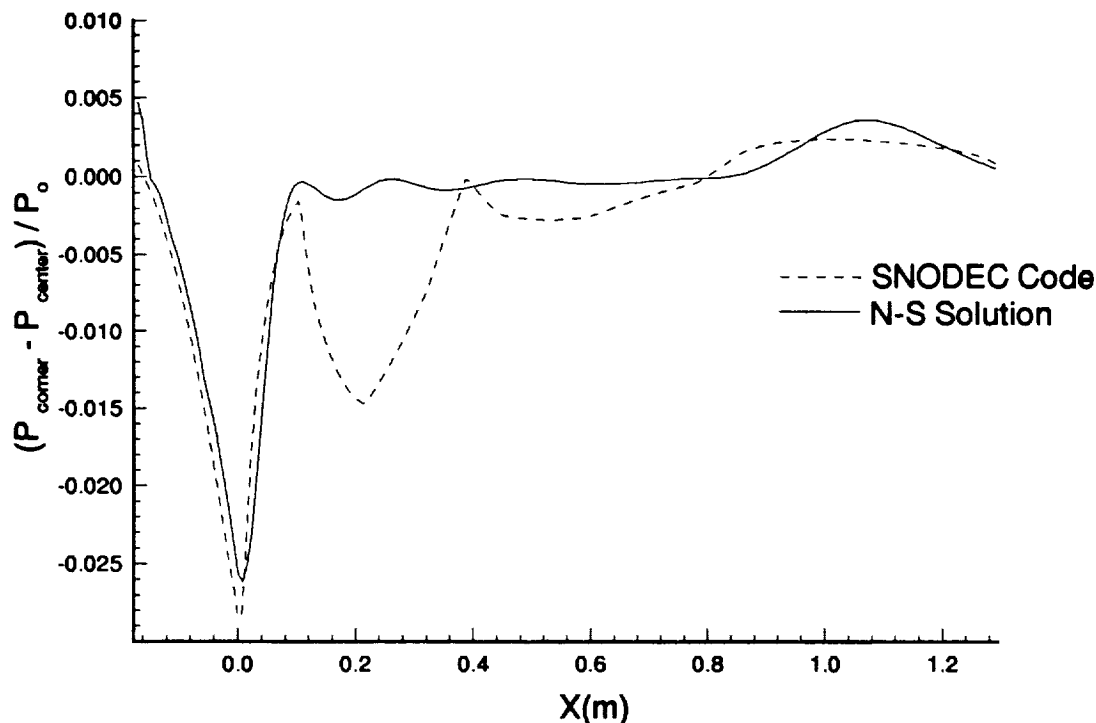
Figure 52-Pressure Difference Between the Centerplane and Corner, Navier-Stokes Results and Inviscid Design

After completing the Navier-Stokes calculation on this nozzle, the Mach contours were again plotted in both the centerplane and cornerplane. This can be seen in figure 49. This figure shows that the maximum deviation in the test rhombus is about +0.008 from the design Mach number of 2.4. This is about 50% less than in the short design signifying a more even flow in the test section. The Mach contours were then plotted at the nozzle exit plane, shown in figure 50, to investigate the uniformity. The maximum deviation at this location is +0.002 in Mach number which is in the same range as was seen in the short nozzle. Finally, figure 51 shows the v and w velocity vectors at the nozzle exit near the corner. Again, counter-rotating vortices are present like those seen in the short nozzle. However, the reference vector shows that these vortices are smaller in magnitude than those in the short nozzle. It is reasonable to conclude that a longer nozzle design will have smaller vortices near the corner. Also note that these vortices cover a region of 3% of the length of the wall and are therefore are not expected to dominate the boundary-layer transition.

The difference in pressure between the corner and centerplane on the wall is

shown in figure 52 for both the inviscid design and the Navier-Stokes solution. As in figure 25, a large dip is seen in the nozzle throat, after which, the difference goes to about zero. Also note that the Navier-Stokes results seem to agree better with the inviscid design than in the short nozzle. There are significant differences between the two however, especially after the throat, where the inviscid design predicts another significant change not seen in the Navier-Stokes results. The reason for this dip is unknown, but could be caused by the Mach number differences at the beginning of the radial flow region. Further comparisons will be presented in the next section where an attempt is made to analyze the reasons for the large gradient in the throat.

Figure 53 shows the values for W_{MAX}/U_e in percentages for the long nozzle. Comparison with the short nozzle results show that there are no significant differences in the throat region. However, near the exit there is a reduction in the maximum crossflow velocity of about 2 percent of the edge velocity, assuming that the edge velocities in the two nozzles are approximately the same at relative streamwise locations. Also evident is the more gradual build-up of crossflow in the exit region, as signified by the larger spacing between contours. Further investigation of this is shown in figures 54 and 55 where the streamwise and crossflow profiles are plotted, along with the line from which they are taken. Comparing figure 54 and figure 45, it can be seen that the profiles are approximately the same in both nozzles up to the throat. After the throat, there is a more gradual increase in the streamwise velocity in the long nozzle, as is expected in a slower expansion nozzle. Comparing figure 55 with figure 46, it is evident that the contours in the throat region are similar while those near the exit are approximately 2/3 the magnitude of those in the short nozzle. This can be expected, considering the data seen in the WMAX/Ue contours in figure 53 and 30. Finally, figure 56 shows the progression of the crossflow through the s-shaped region. Note that the profiles are taken at intervals of $\Delta x = 0.02941$m up to the dashed line and $\Delta x = 0.0147$m after the dashed line. Here again, compared to the short nozzle, these contours are much more gradual in their change from one direction to the other.

Before analyzing the crossflow Reynolds number data, the limits for which the data is useful must be known. The boundary-layer thickness is shown for the long nozzle at the throat in figure 40. It can be seen here that the boundary-layer thickness in the long nozzle is slightly thicker than in the short nozzle. This is expected since the long nozzle has a slower convergence to the throat, giving the boundary-layer more time to develop. This figure the same discontinuity in the long nozzle that was seen in the short nozzle. Figure 41 shows a closer view of the discontinuity region. From this
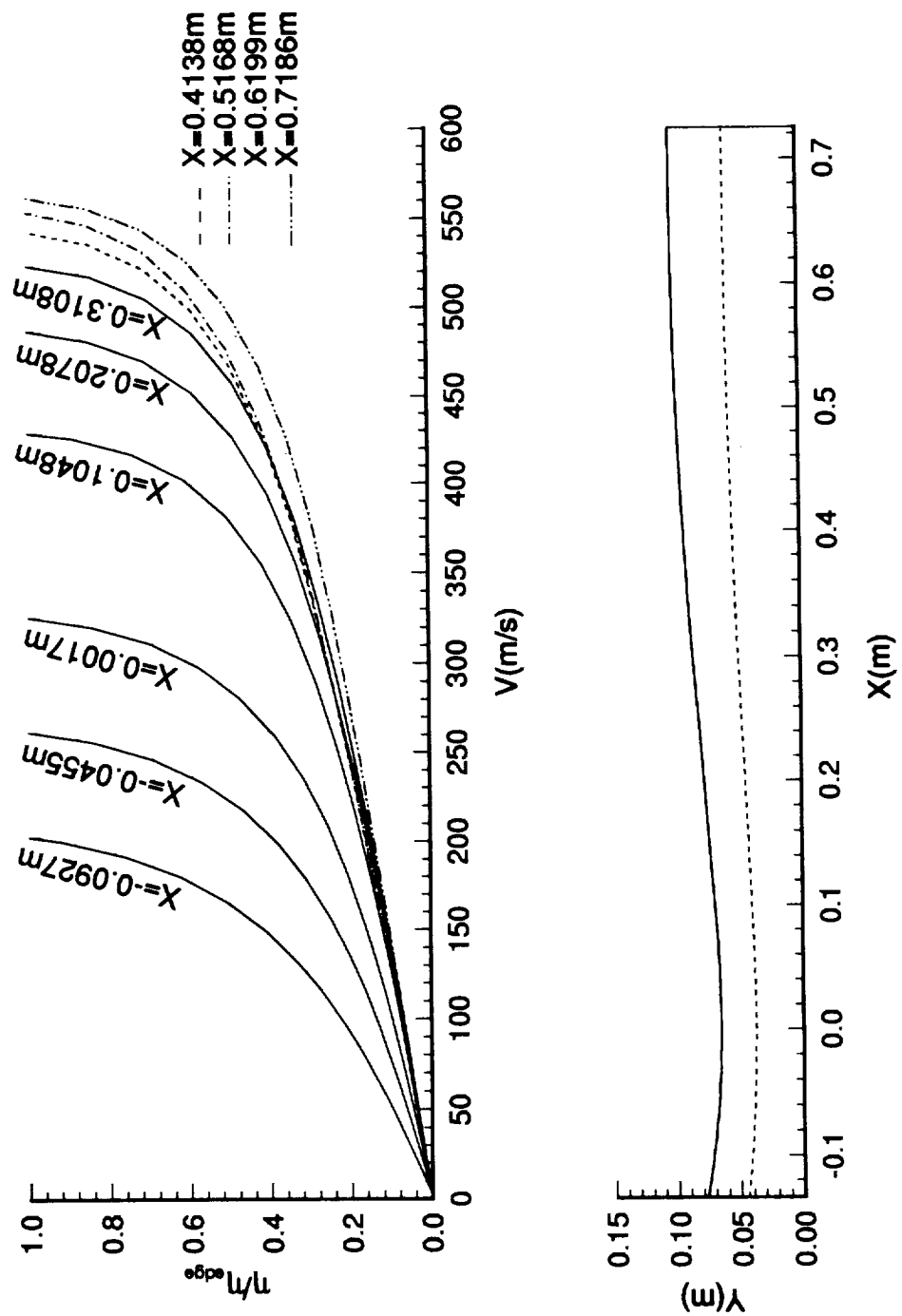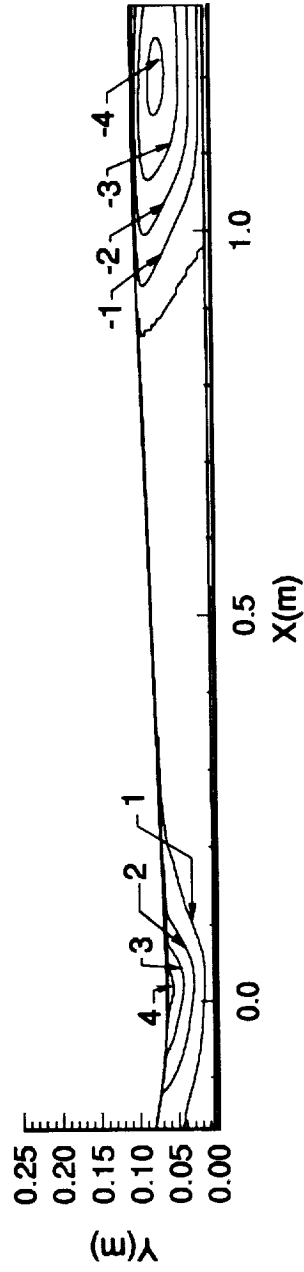
Figure 53-W$_{MAX}$/U$_e$ in Percentages
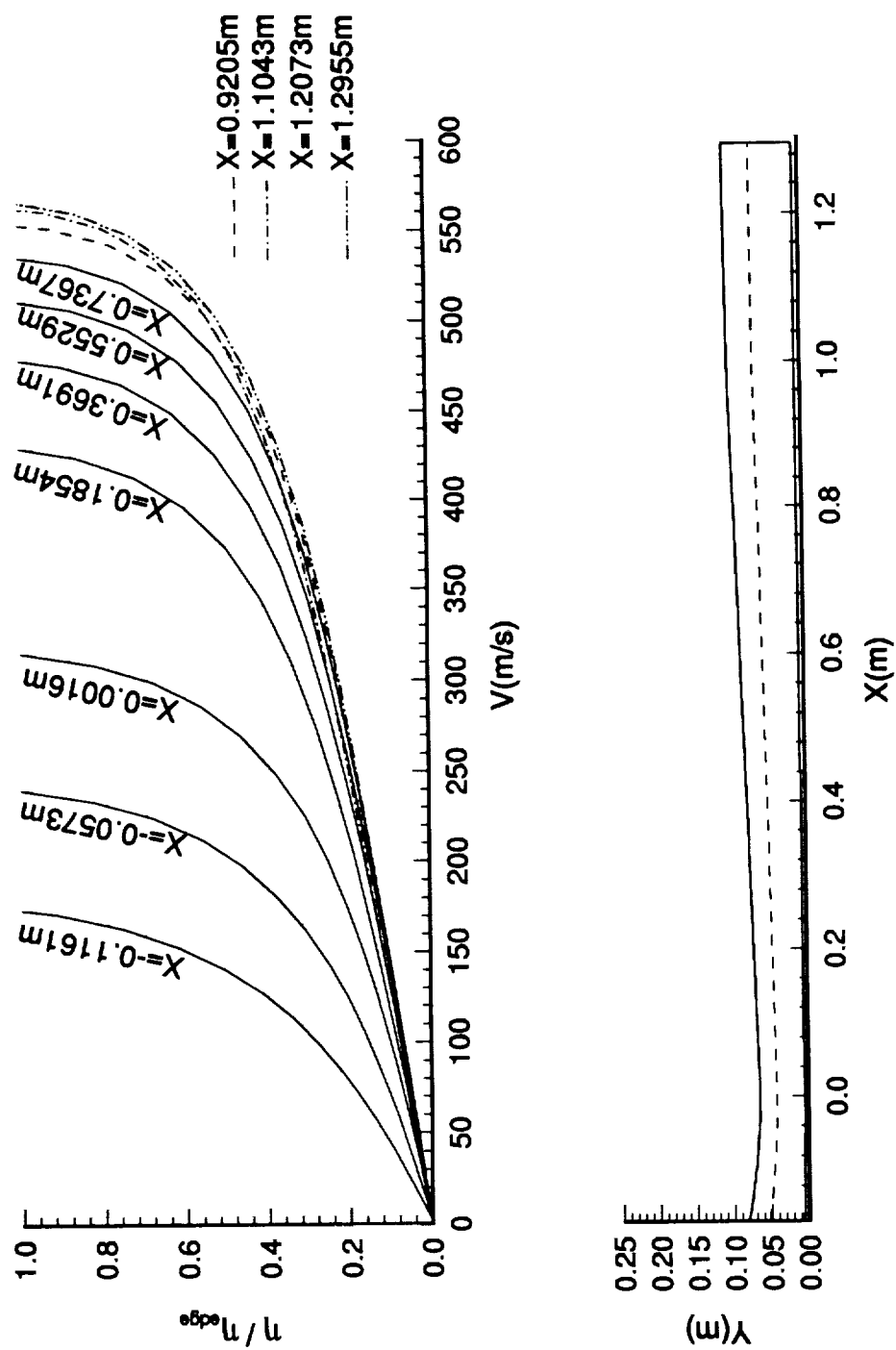
Figure 54 Streamwise Profiles and Line Along Which They are Taken
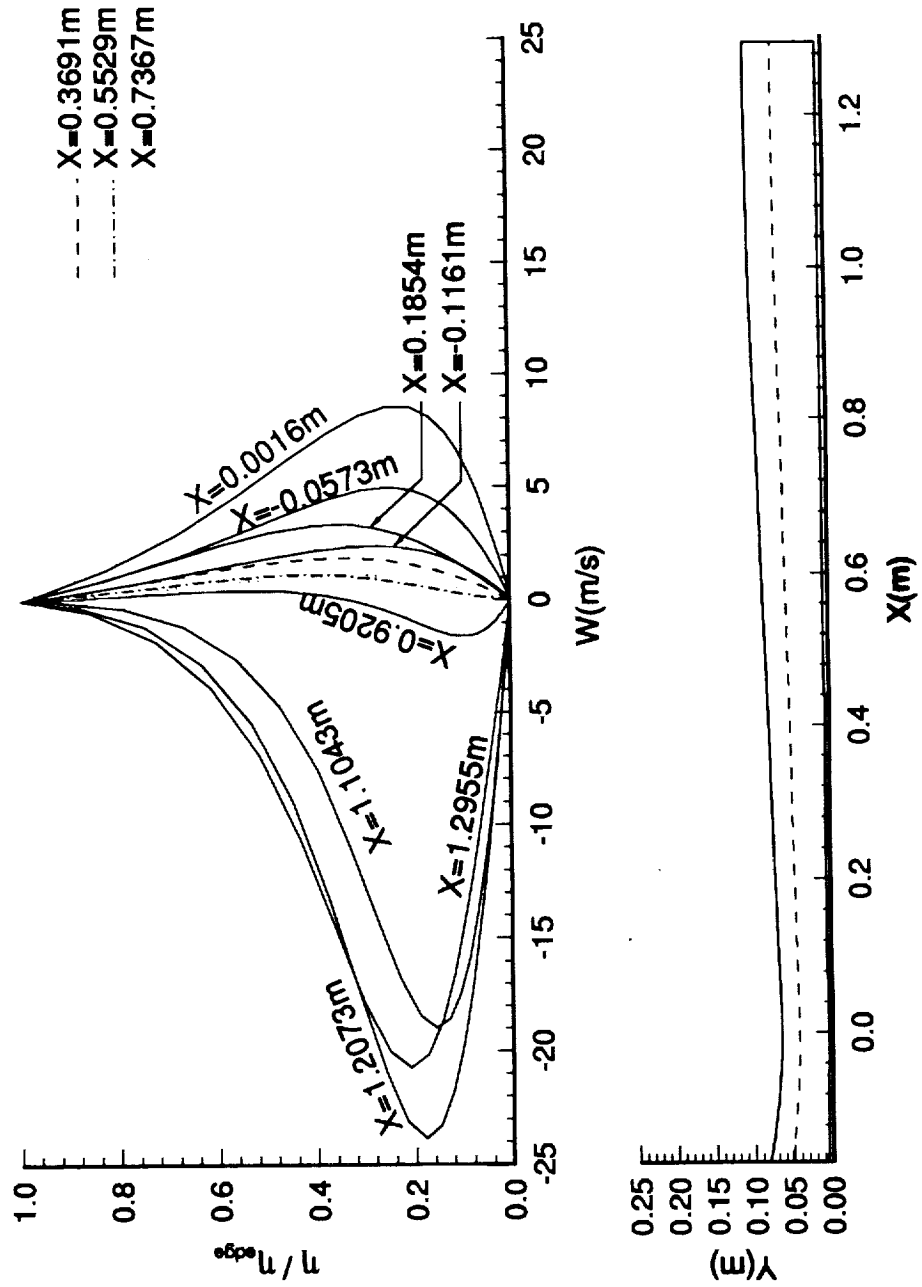
Figure 55-Crossflow Profiles and Line Along Which They are Taken
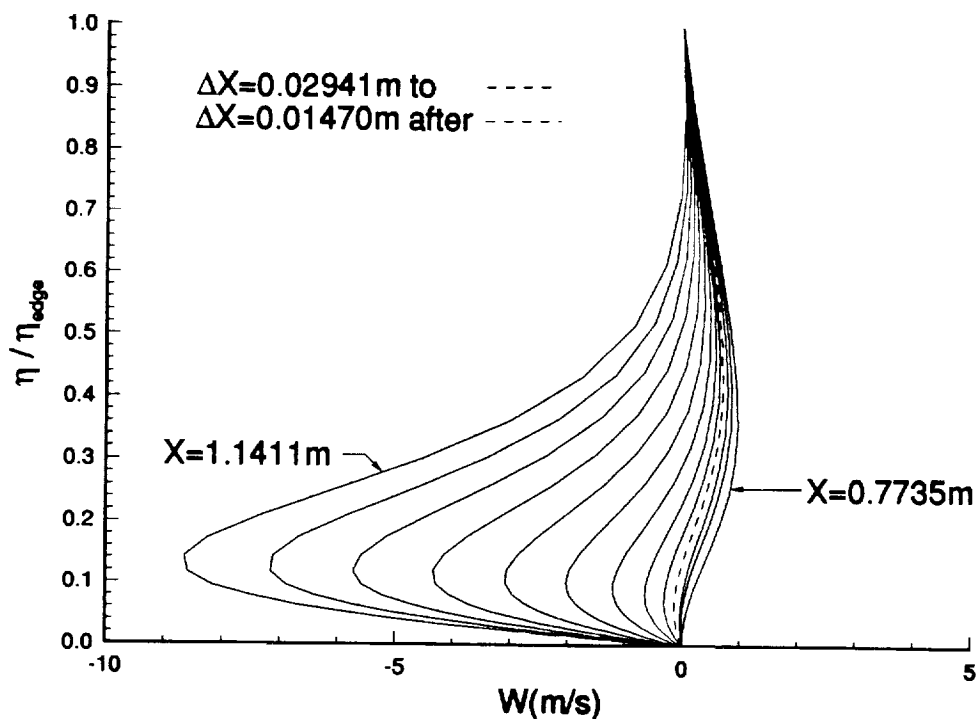
Figure 56-Crossflow Profiles Through S-Shaped Region

figure, the corner flow begins at y=0.0014m from the corner. This is the same location as in the short nozzle. The boundary-layer thickness at the exit is shown in figure 42. It can be seen that the long nozzle boundary-layer is again thicker than in the short nozzle. However, this is expected since the long nozzle boundary-layer has almost twice the length in which to develop. The discontinuity seen in figure 42 is expanded in figure 43. This figure shows that the corner region in the long nozzle begins slight closer to the corner itself, at y=0.0020m from the corner opposed to 0.0035m seen in the short nozzle.

Figures 57-59 show R_{cf}, $R_{cfR\&H}$, and $R_{\delta2}$ respectively. Comparing these to the short nozzle results, in figures 32-34 respectively, shows that the results are comparable in the throat region while the maximums are all about 25 percent smaller near the exit. This is consistent with the reduction seen in W_{MAX}/U_e for the long nozzle when compared with the short nozzle results. A similarity is again noticed between Reed and Haynes crossflow Reynolds number and Beasleys crossflow Reynolds number in figures 58 and 59 respectively.
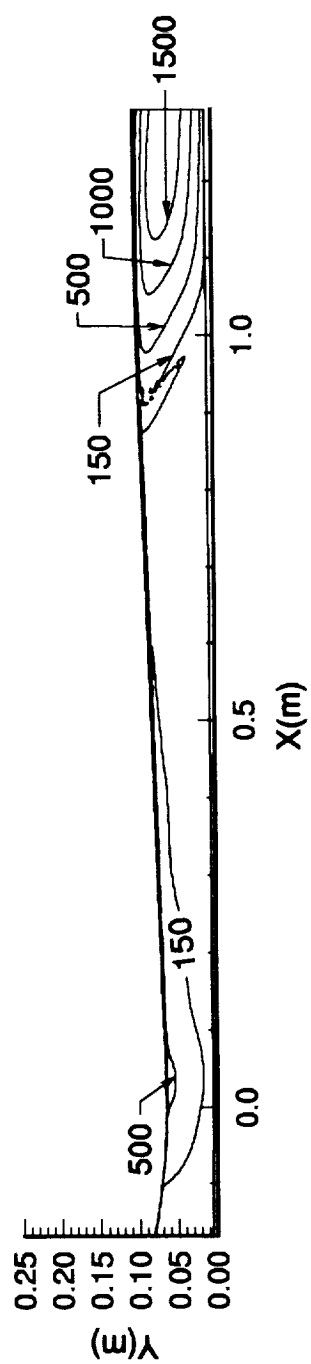
Figure 57-Standard Crossflow Reynolds Number
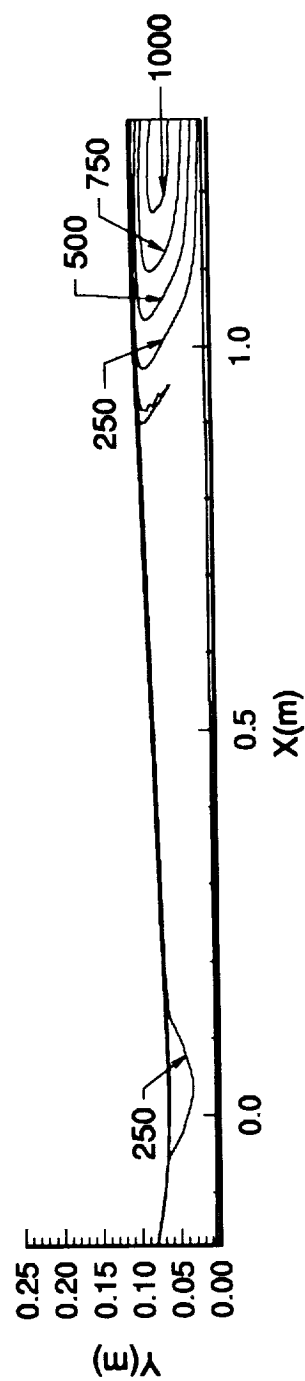
Figure 58-Reed and Haynes Crossflow Reynolds Number
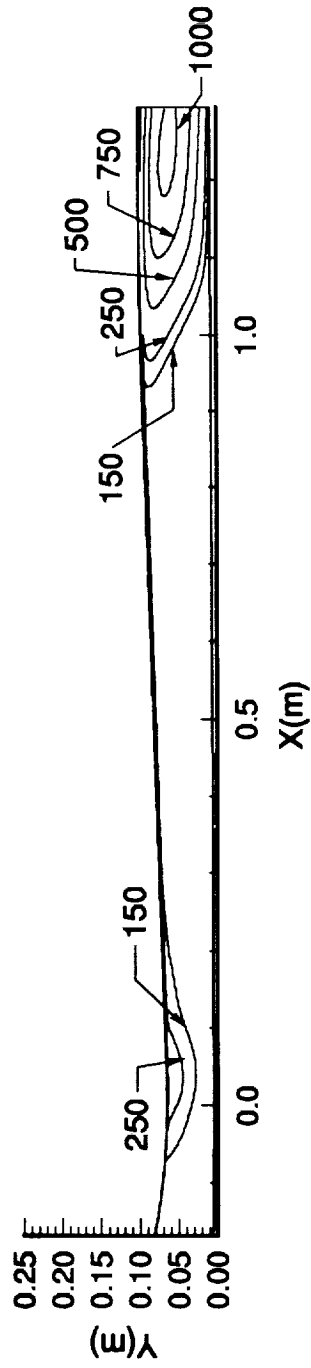
Figure 59-Crossflow Reynolds Number by Beasley
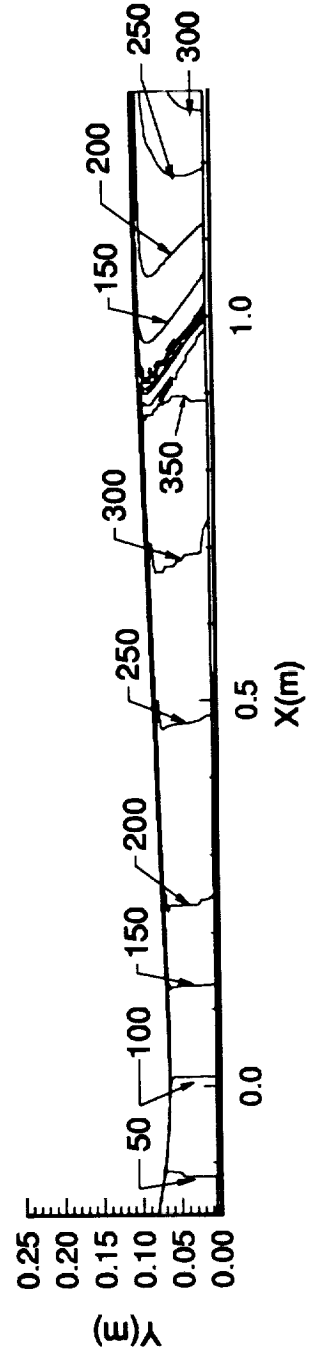
Figure 60-Reed and Haynes Transition Estimator, R

Since the long and short nozzles are designed for the same Mach number, the transition crossflow Reynolds numbers are again 240 near the throat and 430 at the exit. Figure 57 shows that there is a region in the throat where the computed crossflow Reynolds number is greater than 500, or more than two times the estimated transition criterion. In the exit, the computed crossflow Reynolds number is greater than 1500, or larger than 3.5 times the estimated transition. The transition parameter R given by Reed and Haynes is shown in figure 60. An interesting point here is that the values for this parameter are larger than in the short nozzle while the crossflow Reynolds numbers are smaller. Although most of the data for the R parameter is greater than the predicted transition value of 44.0, most of the data is out of the suggested range of 2% < W_{MAX}/U_e < 8%. Taking the data from the prescribed region, the transition parameter in the throat is 100, more than two times the estimated transition of 44.0. Near the exit, the transition parameter becomes a maximum of 300, which is almost 7 times the estimated transition value. Finally, the streamwise shape factor is shown in figure 61. Using the C1 criterion, transition should again occur as soon as $R_{\delta 2}$ becomes larger than 150. This occurs right in the nozzle throat and near the exit. However, the streamwise shape factor is only in the range of 2.3 < H_{shp} < 2.7 in the throat region. Therefore, transition can only be estimated in the nozzle throat, after which, no further conclusions can be drawn. The first occurrences of transition estimated by these various methods is shown in table 5 below

Table 5-Transition Estimates for the Long Mach 2.4 Nozzle

Method	Location Near Throat	Location Near Exit
R_{cf}	X=-0.045m	X=0.975m
$R_{cf}R\&H$	X=-0.1m	X=1.0m
$R_{\delta 2}$	X=-0.075m	Inapplicable

None of the methods have comparable results for transition near the throat. It is unclear why the differences occur in these methods near the throat. Near the exit, the
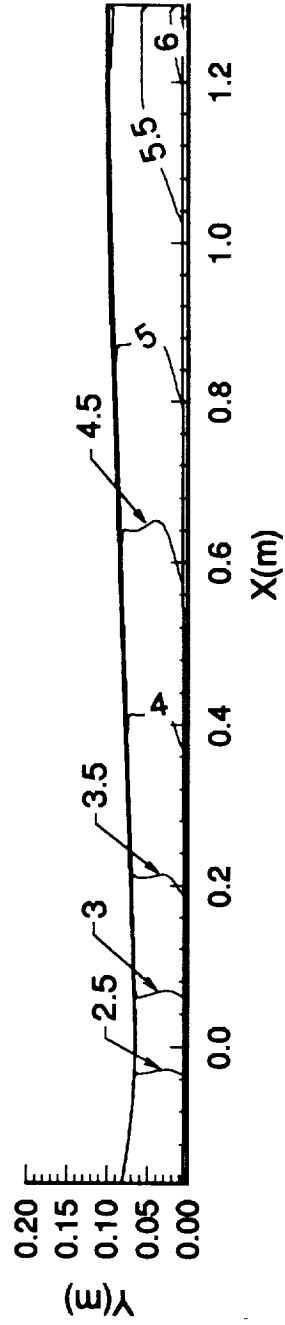
Figure 61-Streamwise Shape Factor

first and second method again estimate transition in about the same location while nothing can be said about the third technique. However, the two methods are not as close as they were for the short nozzle. Note that the transition locations also first occur near the corner which is where the above locations are reported.

Although transition is likely to occur both near the throat and the exit, it is more likely to occur near the exit plane where the crossflow Reynolds numbers are very large. Therefore, assuming that transition will not occur in the throat, a quiet-test Reynolds number can be calculated for the long nozzle. Again, sketching straight lines that approximate the characteristics that bound the test rhombus and come from the wall approximately 1.0 meter downstream of the throat, a quiet test length of approximately 0.17m is calculated. This corresponds to a quiet-test Reynolds number ($R_{\Delta x}$) of 1.2 x 10^7. Although lengthening the nozzle reduces the amount of crossflow apparent in the boundary-layer, the relative locations of transition appears to be the same regardless of the length. However, these computations of quiet-flow length are very preliminary.

Although it has been assumed that transition may not occur in the nozzle throat, recent computational results [64] suggest that this is not the case. A linear stability analysis was performed on the long nozzle geometry using a unit Reynolds number of 1.0 x 10^7 ft^{-1}. The results of this analysis state that at 75% of the distance from the centerplane to the corner, the N-factor was about 4 or 5 in the throat, 8 at about 0.3 ft, and about 9 at 1.0 feet downstream of the throat. In general, the N-factors rise rapidly thorough the throat region and then level-off. The results also state that at 89% of the way to the corner, the N-factor was 10 at 0.5 ft downstream of the throat. Since N-factors greater than 9 usually result in transition, it is very likely that transition will occur slightly downstream of the throat in the long nozzle. Although the crossflow Reynolds numbers were not accurate in estimating the exact location of transition, the data still suggested that transition would occur in the throat region. Therefore, the crossflow Reynolds number techniques were helpful in determining the applicability of these nozzles for quiet-test nozzles.

3.4 Reduction of Crossflow Pressure Gradient in Nozzle Throat

The two Mach 2.4 nozzle designs provided quiet-test Reynolds numbers that are comparable to those in quiet-flow nozzles used today. However, to obtain these results, the possibility of transition in the nozzle throat had to be neglected. The linear stability

analysis by Malik showed that transition will most likely occur in the throat of the long nozzle. Since the crossflow results in the short nozzle are similiar to those in the long nozzle, it is reasonable to assume that transition will occur in this nozzle as well. Therefore, to design a square nozzle which will not experience transition near the nozzle throat, a method must be developed to minimize the crossflow in this region. This is the purpose of this section.

Before new designs can be developed with smaller crossflow in the throat region, the reasons for the crossflow must be known. As discussed in the introduction, crossflow is created by a pressure gradient that is perpendicular to the freestream direction. Therefore, to reduce the crossflow in the nozzle, the pressure gradient between the nozzle centerplane and corner must be reduced. In the inviscid design, this can be done through the relation

$$\frac{P}{P_O} = \left[1 + \frac{\gamma - 1}{2} M^2 \right]^{-\frac{\gamma}{\gamma - 1}} \tag{37}$$

where γ Ratio of Specific Heats

           P   Pressure

           P_O Total Pressure

           M   Mach Number

Therefore, the crossflow pressure gradient can be determined as long as the Mach numbers are known at the centerplane and the corner.

Figure 62 shows the Mach number contours at the throat for the Navier-Stokes solution in the short nozzle design. As can be seen, the Mach number increases radially towards the corner, with the Mach number at the wall in the centerplane being smaller than in the corner. Also note that the Mach number at the centerplane and the corner is slightly greater than 1.0. This data can then be taken into account by setting the Mach number at the corner to be 1.0+ε, where ε is small. This can then be substituted into the above equation, and an approximate solution is found assuming that all terms ε^2 and smaller are neglected. The solution is then found to be
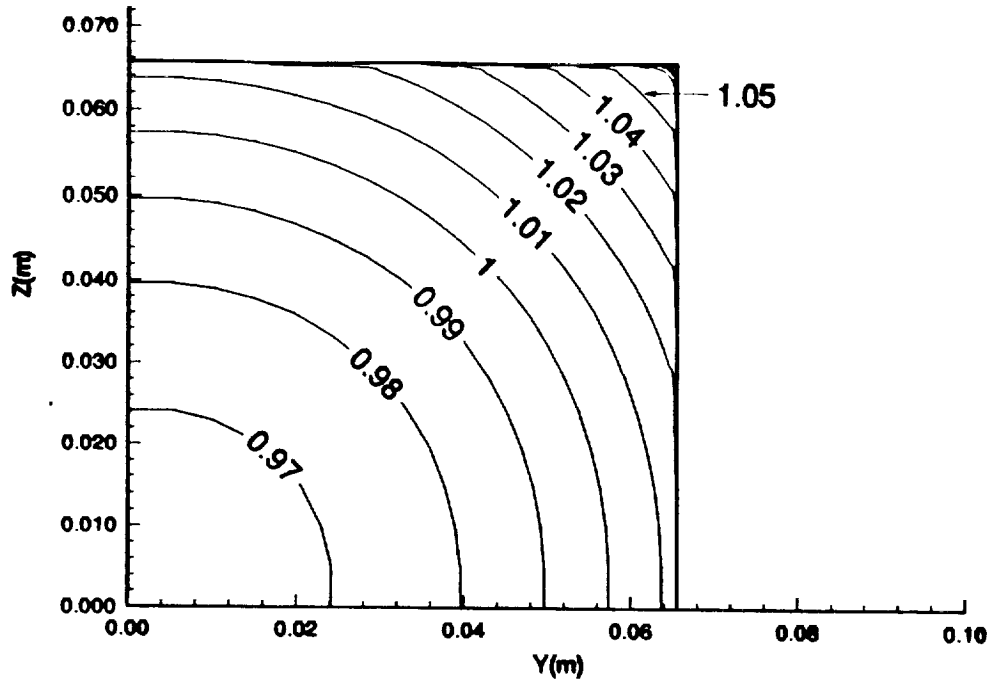
Figure 62-Mach Contours in the Short Nozzle Throat

$$\frac{P}{P_o}\bigg|_{corner} \approx \left[\frac{\gamma+1}{2}\right]^{-\frac{\gamma}{\gamma-1}}\left[1-\left(\frac{2\gamma}{\gamma+1}\right)\varepsilon\right] \tag{38}$$

This technique can also be applied in the centerplane of the nozzle by letting $M = 1.0 +$ β where β is small and $\varepsilon > \beta$. The solution in the centerplane is then found to be

$$\frac{P}{P_o}\bigg|_{center} \approx \left[\frac{\gamma+1}{2}\right]^{-\frac{\gamma}{\gamma-1}}\left[1-\left(\frac{2\gamma}{\gamma+1}\right)\beta\right] \tag{39}$$

Subtracting these two equations gives the approximate pressure gradient between the corner and center of the nozzle

$$\frac{P}{P_o}\bigg|_{corner} - \frac{P}{P_o}\bigg|_{center} \approx \left[\frac{\gamma+1}{2}\right]^{-\frac{\gamma}{\gamma-1}}\left[-\left(\frac{2\gamma}{\gamma+1}\right)(\varepsilon-\beta)\right] \tag{40}$$

where

ε M_{corner} - 1.0 and is $\ll 1.0$

β M_{center} - 1.0 and is $\ll 1.0$

$\varepsilon > \beta$

Now, to make this pressure gradient as small as possible, $\varepsilon - \beta$ should go to zero. This can be accomplished by making the Mach contours as close to the one-dimensional approximation as possible. This means that in the nozzle throat, the sonic line must be as vertical as possible.

This can be analyzed using the relations of Hopkins and Hill [50] that are used for the transonic portion of the nozzle design. The equations used in this portion of the analysis can be found in detail in reference 52. Referring to figure 63 (figure 1 in Hopkins and Hill) the sonic line begins on the axis where $x = 0.0$. It is also stated that on the reference line $x = \xi$, and $\eta = 0$. Therefore, the location of the sonic point is coincident with the location where $x = \xi = 0$. Substituting this into H_r and its derivatives and M_r and its derivatives, shown in reference 52, give the following relations on the reference line

$$H_r = 1$$
$$H_r' = 0$$
$$H_r'' = \frac{1}{R_s}$$
$$H_r''' = 0$$
$$H_r'''' = -\frac{3}{R_s^2 C_1}$$

$$M_r = 1$$
$$M_r' = \sqrt{\frac{\gamma+1}{2R_s}}$$
$$M_r'' = -\frac{(\gamma-3)(\gamma-1)}{2(\gamma+1)} \frac{1}{R_s}$$

$$(41)$$

where

$$R_s = (0.9322 + 0.0565\gamma)\left[0.6173e^{\left(0.48C_1^{-0.189}\right)} + R_a\left(1.1234 + 0.00771C_1 - 0.000163C_1^2\right) - R_a^2\left(0.0182 + 0.00111C_1 - 0.0000201C_1^2\right)\right]$$

$$(42)$$
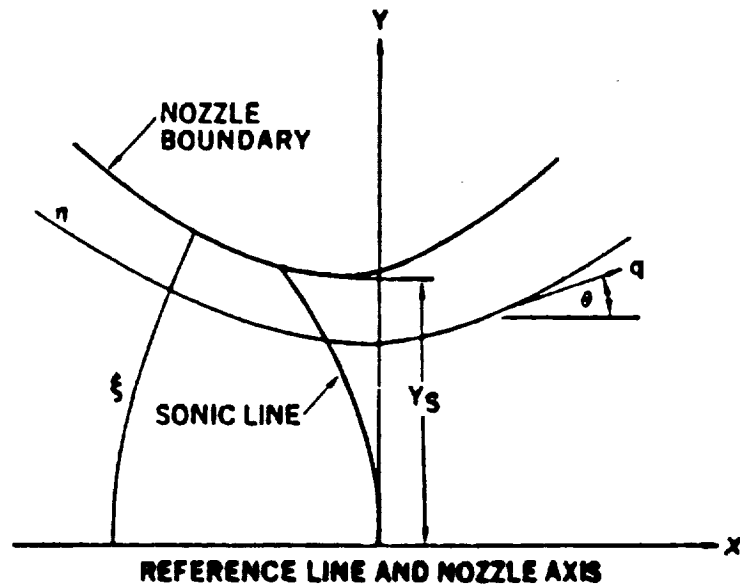
Figure 63-Hopkins and Hill [50] Geometry

$$C_1 = \left[\frac{\arctan\left[\dfrac{\ln\theta_a}{\ln 15000 - \ln R_a}\right]}{19.55 + 1.25(\gamma - 1.4)}\right]^{\dfrac{1}{[0.1277 - 0.0355(\gamma - 1.4)]}}$$

(43)

R_a Radius of Curvature

θ_a Approach Angle

γ Ratio of Specific Heats

These relations can then be substituted into equation (17d) in Hopkins and Hill to get the ratio of dimensionless velocity inside the domain to the dimensionless velocity on the reference line,

$$\frac{M^*}{M_r^*} = 1 + \left(\frac{1}{2R_s}\right)\eta^2 + \left\{\frac{1}{2R_s^2}\left[1 - \frac{1}{2(\gamma + 1)}\right]\right\}\eta^4.$$

(44)

This equation can then be evaluated at two locations, $\eta = 1.0$ corresponding to the square corner, and $\eta = 1/\sqrt{2}$ corresponding to the centerplane. Note that on the reference line, $M_r^* = M_r = 1.0$, simplifying the above equation. The final equations at each location are shown below

$$M^*\Big|_{corner} = 1 + \frac{1}{2R_s} + \frac{1}{2R_s^2}\Phi, \tag{45}$$

and

$$M^*\Big|_{center} = 1 + \frac{1}{4R_s} + \frac{1}{8R_s^2}\Phi, \tag{46}$$

where

$$\Phi = \left[1 - \frac{1}{2(\gamma+1)}\right]. \tag{47}$$

These two equations can be related to the Mach number using the equation

$$M^2 = \frac{2M^{*2}}{\left(\gamma + 1 - (\gamma-1)M^{*2}\right)}. \tag{48}$$

Substitution of equations 45 and 46 into equation 48 gives the Mach number at the corner and the wall in the centerplane in terms of the design parameters R_a and θ_a.

$$M_{corner} = 1.0 + \varepsilon = \left[\frac{2\left(1 + \frac{1}{2R_s} + \frac{1}{2R_s^2}\Phi\right)^2}{\left(\gamma + 1 - (\gamma-1)\left(1 + \frac{1}{2R_s} + \frac{1}{2R_s^2}\Phi\right)^2\right)}\right]^{\frac{1}{2}} \tag{49}$$

$$M_{center} = 1.0 + \beta = \left(\frac{2\left(1 + \frac{1}{4R_s} + \frac{1}{8R_s^2}\Phi\right)^2}{\left(\gamma + 1 - (\gamma - 1)\left(1 + \frac{1}{4R_s} + \frac{1}{8R_s^2}\Phi\right)\right)^2} \right)^{\frac{1}{2}} \tag{50}$$

These two equations can then be solved for ϵ and β and substituted back into equation 37 to give the crossflow pressure gradient in terms of the design variables R_a and θ_a. This final equation is shown below

$$\left.\frac{P}{P_o}\right|_{corner} - \left.\frac{P}{P_o}\right|_{center} \approx \left[\frac{\gamma+1}{2}\right]^{-\frac{\gamma}{\gamma-1}}\left[-\left(\frac{2\gamma}{\gamma+1}\right)(B_0 - B_1)\right] \tag{51}$$

where

$$B_0 = \left(\frac{2\left(1 + \frac{1}{2R_s} + \frac{1}{2R_s^2}\Phi\right)^2}{\left(\gamma + 1 - (\gamma - 1)\left(1 + \frac{1}{2R_s} + \frac{1}{2R_s^2}\Phi\right)\right)^2} \right)^{\frac{1}{2}}$$

$$B_1 = \left(\frac{2\left(1 + \frac{1}{4R_s} + \frac{1}{8R_s^2}\Phi\right)^2}{\left(\gamma + 1 - (\gamma - 1)\left(1 + \frac{1}{4R_s} + \frac{1}{8R_s^2}\Phi\right)\right)^2} \right)^{\frac{1}{2}}$$

For $(P/P_o)_{corner} - (P/P_o)_{center}$ in equation 51 to go to zero, the variable R_s must go to infinity. Referring to equation 42, R_s can only go to infinity if R_a goes to infinity or if C_1 goes to zero or infinity. However, equation 43 shows that C_1 is bounded to be a

finite value by the inverse tangent function. Therefore, the pressure gradient only goes to zero if the radius of curvature goes to infinity or the variable C_1 goes to zero.

By assuming that $\gamma = 1.4$, the above equation can be solved for many different non-dimensional radii of curvature and approach angles. The results are shown in figure 64. For a radius of curvature ratio of less than 2, small changes in the radius of curvature have a large effect on the crossflow pressure gradient. After this point, however, the change is much more gradual. It should also be noted that the maximum radius of curvature used in this analysis is 11.0. After this point, the equations for R_s and C_1 break down since they are curve fits initially developed using radii of curvature less than 11.

Figure 65 shows the radii of curvature from 5 to 10. From this it can be seen that doubling the radius of curvature gives a savings of less than half in the pressure gradient. To verify equation 51, the pressure gradient is estimated from figure 65 at the short and long nozzle radii of curvature. For a radius of curvature of 5, like that in the short nozzle, the pressure gradient is estimated to be approximately -0.036. This is the same result at the throat in figure 25 given by the SNODEC code. For a radius of curvature of 6.6 as in the long nozzle, this approximation gives a pressure differential of -0.029, the same results as seen in figure 52 given by the SNODEC code. From these two results, it seems reasonable to assume that the analysis presented is correct.

The results from the Navier-Stokes solution, however, are not the same as the inviscid design. This could be due to the corner flow or other viscous effects not taken into consideration in the inviscid design. Figure 25 shows that the viscous results have a smaller pressure differential in the throat region. In fact, the pressure differential is approximately 11% smaller than the inviscid design predicted. Figure 52 shows that the viscous results also have a smaller differential in the long nozzle. However, the difference is slightly less than 9%. Since the difference in pressure gradient declines as the radius of curvature increases, it would seem reasonable to assume that as the radius of curvature becomes larger, the inviscid approximation becomes closer to the viscous results. However, two points of data are not enough to verify this assumption. Further analysis is necessary to determine the relation between the crossflow pressure gradient in the inviscid design and the viscous results.

Finally, analysis of how the crossflow pressure gradient affects the crossflow itself would be useful for the nozzle design. This cannot be done explicitly, however, since no correlations exist relating crossflow to the crossflow pressure gradient. The viscous boundary-layer growth is much harder to estimate. The results that have been
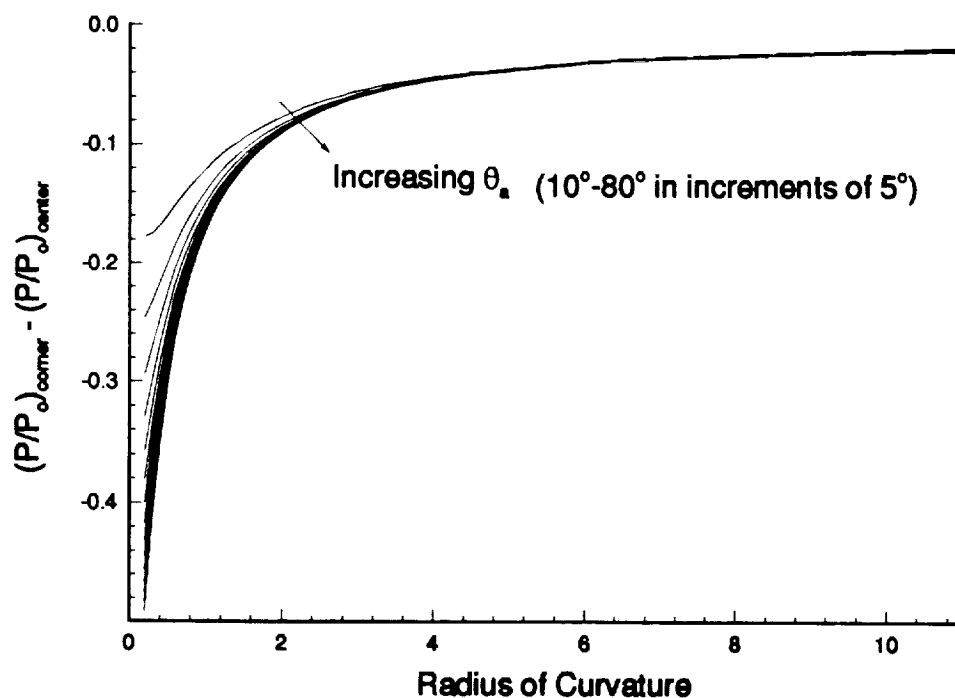
Figure 64-Pressure Difference Between the Centerplane and the Corner for Various Approach Angles and Radii of Curvature
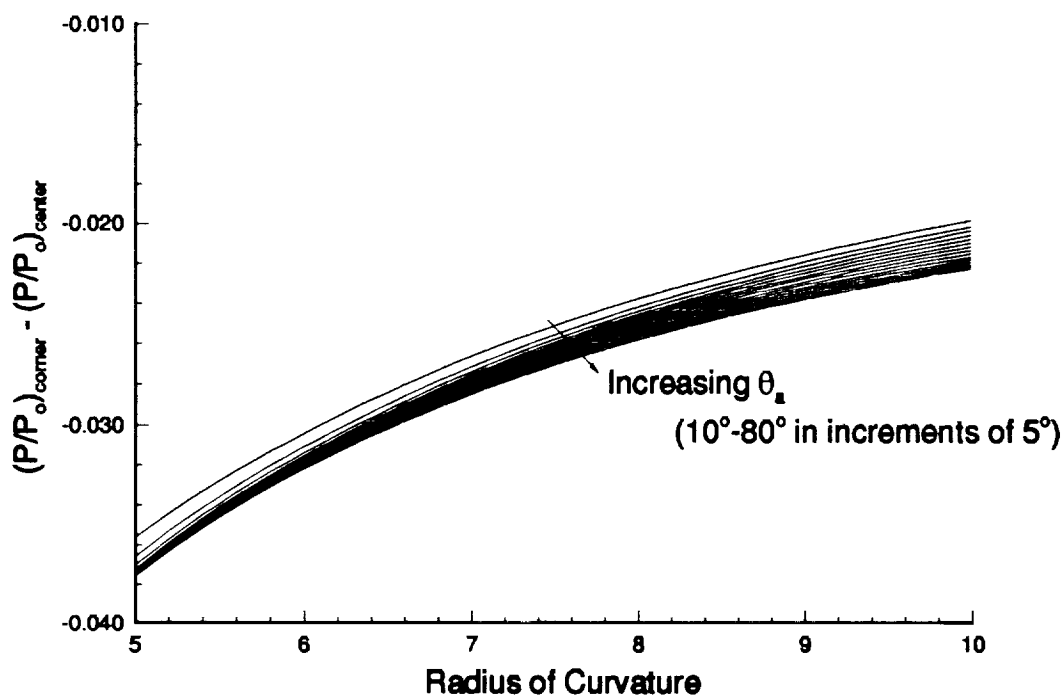
Figure 65-Pressure Difference Between the Centerplane and the Corner for Various Approach Angles in the Region of Interest of the Radius of Curvature

obtained in this investigation, however, can be used to try to get an idea of how these two properties interact. Figures 30 and 32-34 show the W_{MAX}/U_e contours and the crossflow Reynolds numbers for the short nozzle. Figure 30 shows that the maximum value of W_{MAX}/U_e in the throat is almost 5 corresponding to R_{cf} of a little more than 500, $R_{cfR\&H}$ of approximately 500, and $R_{\delta 2}$ of about 300. These values occur with a crossflow pressure gradient of about -0.0325 as a fraction of the total pressure. In the long nozzle, the crossflow pressure gradient is about -0.0265 as a fraction of the total pressure, or about 18.5% smaller than in the short nozzle. Figures 53 and 57-59 show the W_{MAX}/U_e contours and the crossflow Reynolds numbers for the long nozzle. It can be seen in figure 53 that the maximum value of W_{MAX}/U_e is about 4. This is 20% smaller than in the short nozzle. However, in figures 57-59, the maximum crossflow Reynolds numbers are R_{cf} of approximately 500, $R_{cfR\&H}$ of about 450, and $R_{\delta 2}$ close to 300. This corresponds to only a slight decrease in R_{cf}, a 10% reduction in RcfR&H, and no real difference in the value of $R_{\delta 2}$.

This suggests that the decrease in the crossflow pressure gradient has a linear effect on the decrease in W_{MAX}. However, with this decrease comes an increase in the boundary-layer thickness evident in figure 40. This is most likely the reason for the standard crossflow Reynolds number being approximately constant. Therefore, if a new nozzle was designed with a radius of curvature of 10, the crossflow pressure gradient would be in the range of -0.021 or about 40% smaller than in the short nozzle design. The corresponding maximum value of W_{MAX}/U_e in the throat would then be around 2%. Since this analysis is very preliminary, it is unclear whether this reduction would be enough to prevent transition from occurring in the throat. Further analysis must be completed to verify these observations. The effect of crossflow pressure gradient on the resulting crossflow boundary-layer profiles is as yet poorly understood.

CHAPTER IV   CONCLUSIONS

CFD simulations of the flow through two Mach 2.4 nozzles with square test sections have been completed. The initial design of a Mach 8 nozzle with a square test section has also been completed. Grid refinement studies have been completed to verify the accuracy of the solutions. The results showed that the solutions are accurate enough for preliminary design work, but more accurate results must be obtained for reliable stability-based transition estimation techniques. The boundary-layer edge definition was also shown to be an important parameter for the calculation of the preliminary methods used to estimate transition.

Three preliminary methods of estimating crossflow-induced transition have been applied to the simulation results for both Mach 2.4 nozzles. Estimates have shown that transition is likely in the throat, and even more likely near the exit in both nozzles. Assuming transition does not occur in the throat of either nozzle, estimates of the quiet test length were completed for both nozzles. Results suggest that these nozzles might be suitable for quiet-flow facilities. However, recent investigations by other workers using e^N techniques suggest that transition occurs slightly downstream of the nozzle throat.

A design procedure has been developed to study the crossflow pressure gradient in the nozzle throat. Initial estimates, using the solutions for the Mach 2.4 nozzles, suggest that the ratio of radius of curvature to the throat radius of 10 or greater may be necessary to eliminate transition in the nozzle throat. These results are preliminary, however, and more cases need to be tested to verify this procedure.

LIST OF REFERENCES

LIST OF REFERENCES

1. Morkovin, Mark V.: Panoramic View of Changes in Vorticity Distribution in Transition Instabilities and Turbulence. *Boundary-Layer Stability and Transition to Turbulence*, ASME 1991.

2. Reshotko, Eli.: Boundary-Layer Instability, Transition and Control. AIAA Paper 94-0001, January 1994.

3. Stetson, Kenneth F. and Kimmel, Roger L.: On Hypersonic Boundary-Layer Stability. AIAA Paper 92-0737, January 1992.

4. Beckwith, I. E. and Miller, C. G., III.: Aerothermodynamics and Transition in High-Speed Wind Tunnels at NASA Langley. *Annual Review of Fluid Mechanics*, Vol. 22, 1990, pp 419-439.

5. Pate, S. R. and Schueler, C. J.: Radiated Aerodynamic Noise Effects on Boundary-Layer Transition in Supersonic and Hypersonic Wind Tunnels. *AIAA Journal*, Vol. 7, No. 3, March 1969, pp 450-457.

6. Laufer, John: Aerodynamic Noise in Supersonic Wind Tunnels. *Journal of Aerospace Sciences*, Vol. 28, 1961, pp 685-692.

7. Beckwith, I. E.; Creel, T. R.; Chen F.-J.; and Kendall, J. M.: Free Stream Noise and Transition Measurements on a Cone in a Mach 3.5 Pilot Quiet Tunnel. NASA TP-2180, September 1983.

8. Beckwith, I. E.: Development of a High Reynolds Number Quiet Tunnel for Transition Research. *AIAA Journal*, Vol. 13, No, 3, March 1975, pp 300-306.

9. Anders, J. B.; Stainback, P. C.; and Beckwith, I. E.: New Technique for Reducing Test Section Noise in Supersonic Wind Tunnels. *AIAA Journal*, Vol. 18, No. 1, January 1980, pp 5-6.

10. Wilkinson, S. P.; Anders, S. G.; and Chen, F.-J.: Status of NASA Langley Quiet Flow Facility Developments. AIAA Paper 94-2498, June 1994.

11. Beckwith, I. E.; Malik, M. R.; and Chen, F.-J.: Nozzle Optimization Study for Quiet Supersonic Wind Tunnels. AIAA Paper 84-1628, June 1984.

12. Chen, F.; Malik, M.; and Beckwith, I.: Advanced Mach 3.5 Axisymmetric Quiet Nozzle. AIAA Paper 90-1592, June 1990.

13. Chen, F. J.; Malik, M. R.; and Beckwith, I. E.: Instabilities and Transition in the Wall Boundary Layers of Low-Disturbance Supersonic Nozzles. AIAA Paper 85-1573, July 1985.

14. Wilkinson, S. P.; Anders, S. G.; Chen, F.-J.; and Beckwith, I. E.: Supersonic and Hypersonic Quiet Tunnel Technology at NASA Langley. AIAA Paper 92-3908, July 1992.

15. Wolf, Stephen W. D.; Laub, James A.; King, Lyndell S.; and Reda, Daniel C.: Development of the NASA-Ames Low-Disturbance Supersonic Wind Tunnel for Transition Research up to Mach 2.5. AIAA Paper 92-3909, July 1992.

16. Schneider, Steven P.; and Haven, Christine, E.: Mean Flow and Noise Measurements in the Purdue Quiet-Flow Ludwieg Tube. AIAA Paper 94-0546, January 1994.

17. King, L. S.; and Demetriades, A.: Comparison of Predictions with Measurements for a Quiet Supersonic Tunnel. AIAA Paper 93-0344, January 1993.

18. Demetriades, Anthony: Stabilization of a Nozzle Boundary Layer by Surface Heating. AIAA Paper 94-2501, June 1994.

19. Herbert, T.: Boundary-Layer Transition - Analysis and Prediction Revisited. AIAA Paper 91-0737, 1991.

20. Herbert, T.: Parabolized Stability Equations. AGARD R-793, 1994.

21. White, Frank M.: *Viscous Fluid Flows*. McGraw -Hill, Inc., New York, NY 1991.

22. Beckwith, I.; Chen, F.; Wilkinson, S.; Malik, M. and Tuttle, D.: Design and Operational Features of Low-Disturbance Wind Tunnels at NASA Langley for Mach Number from 3.5 to 18. AIAA Paper 90-1391, June 1990.

23. Chen, F.-J.; and Wilkinson, S. P.: Design of Mach 2.4 Quiet Nozzles for the NASA Langley Supersonic Low-Disturbance Pilot Tunnel. AIAA Paper 94-2506, June 1994.

24.   Saric, William S.: Görtler Vorticies. *Annual Review of Fluid Mechanics*, Vol. 26, 1994, pp 379-409.

25.   Davis, D. O.; Gessner, F. B.; and Kerlick, G. D.: Experimental and Numerical Investigation of Supersonic Turbulent Flow Through a Square Duct. *AIAA Journal*, Vol. 24, No. 9, September 1986, pp 1508-1515.

26.   Davis, D. O.; Gessner, F. B.; and Kerlick, G. D.: Supersonic Laminar Flow Development in a Square Duct. *AIAA Journal*, Vol. 25, No. 1, January 1987, pp 175-177.

27.   Mikhail, A. G.; and Ghia, K. N.: Viscous Compressible Flow in the Boundary Region of an Axial Corner. *AIAA Journal*, Vol. 16, No. 9, September 1978.

28.   Dhanak, M. R.: Instability of Flow in a Streamwise Corner. NASA CR-191419, December 1992.

29.   Alcenius, T. J.; Schneider, S. P.; Beckwith, I. E.; White, J. A.; and Korte, J. J.: Development of Square Nozzles for High-Speed Low-Disturbance Wind Tunnels. AIAA Paper 94-2578, June 1994.

30.   Zamir, M.: Similiarity and Stability of the Laminar Boundary-Layer in a Streamwise Corner. *Proceedings of the Royal Society London*, A 377, 1981, pp 269-288.

31.   Pfenninger, W.; and Syberg, J,: Reduction of Accoustic Disturbances in the Test Section of Supersonic Wind Tunnels by Laminarizing Their Nozzle and Test Section Wall Boundary Layers by Means of Suction. NASA CR-2436, November 1974.

32.   Reed, Helen L,; and Saric, William S.: Stability of Three-Dimensional Boundary Layers. *Annual Review of Fluid Mechanics*, Vol. 21, 1989, pp 235-284.

33.   Saric, William S.: Low-Speed Boundary-Layer Transition Experiments. *Transition: Experiments, Theory & Computations*. Corke, Eriebacher, and Hussaini, Oxyford, 1994.

34.   Arnal, D.: Boundary Layer Transition: Prediction, Application to Drag Reduction. AGARD R-786, March 1992.

35.   Saric, William S.: Laminar-Turbulent Transition: Fundementals. AGARD R-786, March 1992.

36.   Arnal, Daniel: Three-Dimensional Boundary Layers: Laminar-Turbulent Transition. AGARD R-741, 1986.

37. Poll, D. I. A.: Transition Description and Prediction in Three-Dimensional Flows. AGARD R-709, 1984.

38. Dagenhart, J. Ray: Amplified Crossflow Disturbances in the Laminar Boundary Layer on Swept Wings with Suction. NASA TP-1902, 1981.

39. Reed, Helen L.; and Haynes, Timothy S.: Transition Correlations in 3-D Boundary Layers. AIAA Papaer 93-3054, July 1993.

40. Godil, A.; and Bertelrud, A.: Design of a Wing Shape for Study of Hypersonic Crossflow Transition in Flight. *Computing Systems in Engineering*, Vol. 3, No. 1-4, 1992, pp 115-130.

41. Dagenhart, J. Ray; Saric, W. S.; Mousseux, Marc C.; and Stack, J. Peter: Crossflow-Vortex Instability and Transition on a 45-Degree Swept Wing. AIAA Paper 89-1892, June 1989.

42. Radeztsky, R. H., Jr.; Reibert, M. S.; and Saric, W. S.: Development of Stationary Crossflow Vorticies on a Swept Wing. AIAA Paper 94-2373, June 1994.

43. Obara, Clifford J.; Vijgen, Paul M. H. W.; and Lee, Cynthia C.: Analysis of Flight-Measured Boundary-Layer Stability and Transition Data. AIAA Paper 91-3282, September 1991.

44. Pfenninger, Werner: Laminar Flow Control: Laminarization. AGARD R-654, 1977.

45. Malik, M. R.; Li, F.; and Chang, C.-L.: Crossflow Disturbances in Three-Dimensional Boundary Layers: Nonlinear Development, Wave Interaction and Secondary Stability. *Journal of Fluid Mechanics*, Vol. 286, 1994, pp 1-36.

46. Wang, M.; Herbert, Th.; and Stuckert, G. K.: Crossflow-Induced Transition in Compressible Swept-Wing Flows. AIAA Paper 94-2374, June 1994.

47. Ostrander, Mark J.; Thomas, Scott R.; Voland, Randall T.; Guy, Robert W.; and Srinivasan, Shivakumar: CFD Simulation of Square Cross-Section Contoured Nozzle Flows: Comparison with Data. AIAA Paper 89-0045, January 1989.

48. Arnal, D.; Vignall, F.; and Laburthe, F.: Recent Supersonic Transition Studies with Emphasis on the Swept Cylinder Case. *Boundary-Layer Transition and Control*, The Royal Aeronautical Society, April 1991.

49. Beckwith, Ivan E.; Ridyard, Herbert W.; and Cromer, Nancy: The Aerodynamic Design of High Mach Number Nozzlew Utilizing Axisymmetric Flow with Application to a Nozzle of Square Test Section. NACA TN-2711, June 1952.

50. Hopkins, D. F.; and Hill, D. E.: Effect of Small Radius of Curvature on Transonic Flow in Axisymmetric Nozzles. *AIAA Journal*, Vol. 4, No. 8, August 1966, pp 1337-1343.

51. Sivells, J. C.: A Computer Program for the Aerodynamic Design of Axisymmetric and Planar Nozzles for Supersonic and Hypersonic Wind Tunnels. AEDC-TR-78-63, December 1978.

52. Alcenius, Timothy; and Schneider, Steven P.: Development of a Code for Wall Contour Design in the Transonic Region of Axisymmetric and Square Nozzles. NASA CR-194857, January 1994.

53. Schneider, Steven P.: Method of Characteristics Design of a Supersonic Wind Tunnel Nozzle with Square Cross-Section. NASA CR-194359, January 1993.

54. Harris, Julius E.; and Blanchard, Doris K.: Computer Program for Solving Laminar, Transitional, or Turbulent Compressible Boundary-Layer Equations for Two-Dimensional and Axisymmetric Flow. NASA TM-83207, 1982.

55. Tecplot; Amtec Engineering, Inc. P. O. Box 3633, Bellevue, WA.

56. White, J. A.: LARCK: Langley Algorithm for Research in Chemical Kinetics. Analytical Services and Materials, Inc., 107 Research Drive, Hampton, VA. Private Communications.

57. Jameson, A.; Schmidt, W.; and Turkel, E.: Numerical Solutions of the Euler Equations by Finite Volume Methods Using Runge-Kutta Time-Stepping Techniques. AIAA Paper 81-1259, June 1981.

58. Jameson, Antony: Numerical Solution of the Euler Equation for Compressible Inviscid Fluids. *Numerical Methods for the Euler Equations of Fluid Dynamics*, Ed. F. Angrand, 1985. pp 199-245.

59. Swanson, R. C.; and Radespiel, R.: Cell Centered and Cell Vertex Multigrid Schemes for the Navier-Stokes Equations. *AIAA Journal*, Vol. 29, No, 5, May 1991, pp 697-703.

60. Turkel, E.; Swanson, R. C.; Vatsa, V. N.; and White, J. A.: Multigrid for Hypersonic Viscous Two-Dimensional and Three-Dimensional Flows. NASA CR-187603, July 1991.

61.   Jameson, A.; and Baker, T. J.: Multigrid Solution of the Euler Equations for Aircraft Configurations. AIAA Paper 84-0093, January 1984.

62.   Swanson, R. C.; Turkel, E.; and White, J. A.: An Effective Multigrid Method for High-Speed Flows. NASA CR-187602, July 1991.

63.   Turkel, Eli: Improving the Accuracy of Central Difference Schemes. NASA CR-181712, September 1988.

64.   Lin, Ray-Sing; Edwards, Jack; and Malik, M.: High Technology Corporation, P. O. Box 7262, Hampton, VA 23666. Private Communications.

APPENDICES

APPENDIX

Appendix A   Grid Generation Programs and Data

The following program is used to convert the *.csd files from the SNODEC code to be used in the grid generation program.

```
*    This program was written to convert data from the *.csd file
*    created by a program called SNODEC for the development of
*    square nozzles.  The program reads the data and writes a file
*    for use in a grid generation code.
*
*    Written by:  Tim Alcenius
*                 Purdue University
*                 June 1993.
*
*    Identify variabels and open files to be read.
*
     real x,y,z
     integer i
     open(1, file = 'm8.csd')
     open(2, file = 'param')
     xmax = 0.
     xmin = 0.
*
*    Read the number of data points in any plane.  If it is 1, then go to
*    next section of the program.
*
20   read(1,*) imax
     if(imax .EQ. 1) then
       goto 30
     endif
*
*    Read in variables.  Set minimum and maximum values of x, and
*    then scale data to metric units.
*
     do 10 i = 1, imax
       read(1,*) y,z,x
       if(x .LT. xmin) then
         xmin = x
       endif
       if(x .GT. xmax) then
```

```
          xmax = x
          endif
          if(z .GT. 0 .AND. y .GT. 0 .AND. x .EQ. xmax) then
            yscale = .3048
          endif
10     continue
       goto 20
*
*      Rewind the file for which data was read and write the mimimum and
*      maximum values of x to the output file.
*
30     rewind(1)
       write(2,*) xmin*yscale, yscale*xmax
       print *, yscale
*
*      Read the number of points in the current data set.  If the value is
*      1, then quit.
*
40     read(1,*) imax
       if(imax .EQ. 1) then
         goto 50
       endif
*
*      Write data to the output file in the form of x, ymin, ymax, zmin, zmax.
*
       do 60 i = 1, imax
         read(1,*) y,z,x
       if(y .EQ. z .AND. y .GT. 0 .AND. z .GT. 0 .AND. i .LT. imax) then
         write(2,*) x*yscale,a,y*yscale,b,z*yscale
       endif
60     continue
       goto 40
50     end
```

The following file is the *.csd file for the short Mach 2.4 nozzle created by the SNODEC code. This is given as an example of this type of file.

```
5
  0.253884   0.253884  -0.437861
  0.253884  -0.253884  -0.437861
 -0.253884  -0.253884  -0.437861
 -0.253884   0.253884  -0.437861
  0.253884   0.253884  -0.437861
5
  0.251907   0.251907  -0.426026
  0.251907  -0.251907  -0.426026
 -0.251907  -0.251907  -0.426026
```

```
   -0.251907   0.251907  -0.426026
    0.251907   0.251907  -0.426026
 5
    0.249963   0.249963  -0.414193
    0.249963  -0.249963  -0.414193
   -0.249963  -0.249963  -0.414193
   -0.249963   0.249963  -0.414193
    0.249963   0.249963  -0.414193


                .

                .

                .


 5
    0.334358   0.334358   2.35498
    0.334358  -0.334358   2.35498
   -0.334358  -0.334358   2.35498
   -0.334358   0.334358   2.35498
    0.334358   0.334358   2.35498
 5
    0.334391   0.334391   2.36681
    0.334391  -0.334391   2.36681
   -0.334391  -0.334391   2.36681
   -0.334391   0.334391   2.36681
    0.334391   0.334391   2.36681
 5
    0.334421   0.334421   2.37865
    0.334421  -0.334421   2.37865
   -0.334421  -0.334421   2.37865
   -0.334421   0.334421   2.37865
    0.334421   0.334421   2.37865
 1
```

The following two programs are used in the initial generation of the nozzles. The first is called sivinput and is used to generate the data used in the Sivells code. The second is entitled makeblin and is used to make the input file for the Harris boundary-layer code.

```
* From moen Wed Nov 25 12:00:09 1992
c    this program writes an input file in the correct format for
c    sivells code; sps 6-27-90
c    modified 9-30-92 for the square nozzle work with streamlines sps
c    modified to produce starting streamlines on nozzle wall.
*    mod sps 11-30-92 to make mp=5
*    mod 11-30 sps to allow choices of IN, XC, IX
c
     character*10 title
     character*20 sivfile
c
```

```fortran
      write (*,*) 'enter a rootname to write sivells input file:'
      read (*,10) sivfile
      title = sivfile
      ileng = index(sivfile,' ') -1
      sivfile(ileng+1:ileng+4) = '.inp'
      write (*,*) 'opening file-',sivfile,'-for output'
      open(unit=2,file=sivfile,status='new')
c
*     write (*,*) 'enter title of run (10 characters): '
*     read (*,20) title
      write (*,*) 'enter jd (-1=2D, 0=axisym): '
      read (*,*) jd
      write (2,30) title,jd
*     write (*,*) 'enter sfoa:'
*     read (*,*) sfoa
      sfoa=0.    !use 3rd or 4th degree distribution
      gam = 1.40
      ar = 1716.563
      zo=1
c    following three used in bl computations, not used here
      ro=1
      visc=1
      vism=1
c
      xbl=1000.  !gives values at evenly spaced intervals
      write (2,40) gam,ar,zo,ro,visc,vism,sfoa,xbl
c
      write (*,*) 'enter etad,rc,bmach,cmc: '
      read (*,*) etad,rc,bmach,cmc
      xc=0.    !so 4th degree distribution, change?
*     write (*,*) 'enter xc, in: '
*     read (*,*) xc,in
*     write (*,*) 'xc,in= ',xc,in
      fmach=0.   !this sets distribution, change?
      sf = 0.    !nozzle throat radius = 1.0
      pp = 0.    !coordinates given relative to throat
      write (2,50) etad,rc,fmach,bmach,cmc,sf,pp,xc
c     write (*,*) 'enter mt,nt,ix,in,md,nd,nf,mp,jc,lr,nx:'
c     read (*,*) mt,nt,ix,in,md,nd,nf,mp,jc,lr,nx
      mt=61     !pts on char. EG, max 125
      nt=31     !pts on axis IE, max 149-LR
*     write (*,*) 'enter ix: '
*     read (*,*) ix
      ix=0     !is 3rd deriv matched?  change?
      in=10    !use Mach no. distrib on BC, makes 2nd deriv match rad. flow
c               change?
      iq=0     !calls for complete contour
      md=61    !pts on char. AB, max about 125, odd
      nd=15    !pts on axis BC, max about 150,
c               changed from 49 to 15 sps 7-2-90
      write (*,*) 'enter -1 for smoothing, 1 for no smoothing: '
      read (*,*) ismooth
```

```
      nf=ismooth*81  !pts on characteristic CD.  Neg calls for smoothing
      mp=5    !pts on GA, conical section, if Fmach ne Bmach
      jc=0    !if not 0, used to print intermediate characteristics
      lr=31   !pts on throat char., - prints out transonic soln
      nx=13   !spacing of pts on axis upstream, this no. recc.
      mq=0    !pts downstream of D
      jb=-1   !neg for no BL computation
      jx=1    !pos calls for streamlines
      it=0    !jack points, not used
      write (2,60) mt,nt,ix,in,iq,md,nd,nf,mp,mq,jb,jx,jc,
     >          it,lr,nx
c
      if (ismooth .eq. -1) then
      noup=10  !smoothing parameters, arbitrary
      nodo=10
      npct=90
      write (2,70) noup,npct,nodo
      end if
c
c     gives streamline distribution that corresponds
c     to the half wall for conversion to a square nozzle.
c     note that the number of streamlines requested will
c     be reduced by one because Sivells automatically
c     calculates the wall streamline.  Sivells output
c     will have the actual number of streamlines requested.
c     (moen 10-92)
c
      write (*,*) 'How many streamlines along halfwall?'
      read (*,*) nstream
      nstream=nstream-1
      dx=1.0/(float(nstream)*sqrt(2.0))
      ycnt=1.0/sqrt(2.0)
      do 100 istream = 0,nstream-1
       etadstr = etad*sqrt((istream*dx)**2+ycnt**2) !see btm page 59
       qm = sqrt((istream*dx)**2+ycnt**2)
       xj = 1  !look for more streamlines
       write (2,90) etadstr,qm,xj
       if (ismooth .eq. -1) then
         write (2,70) noup,npct,nodo    !must have for each!!
       end if
  100 continue
c
      close(2)
      stop
   10 format(a20)
   20 format(a10)
   30 format(1x,a10,2x,i2)
   40 format(8(1x,f9.3))
   50 format(8(1x,f9.3))
   60 format(1x,i4,15(i5))
   70 format(1x,i4,2(i5))
   90 format(3(1x,f9.4),1x)
```

118

```
        end

*  SUN VERSION WITH SPACES BEFORE ITEMS IN NAMELIST !! 9-92
*  Steven P. Schneider Purdue University 317-494-3343
*  this is a program to read in output from the sivells code
*    add specifics for Re, and write in a form readable
*    by the Harris code for bl.
*  specific for the nozzle block problem sps 6-90
*  add some code for the contraction computation 12-5-90 sps
*  add code for output of file for arbitrary shape using modified Newtionian thy
*    sps 3-6-91
*  allow for arbitrary power-law distribution of points 3-6-91 sps,
*    and for easy change of jsolve
*  add code for reading in pressure data from euler code, and shock location
*    data, and writing an output file for the harris code 7-13-91 sps
*  modified to fix bug with error code on different case 7-28-91 sps
*
        parameter(maxpts=1000,jsolve=1)
*  jsolve is the number of solution stations per station of input data
*    can increase to make finer resolution solution possible
        character*80 text
        character*20 root,infile,outfile,parmfl
*  most of these are the number of stations along the moc soln
*  ss is the number of stations in bl soln to get
        dimension x(maxpts),y(maxpts),pepo(maxpts),s(maxpts),theta(maxpts)
        dimension proval(maxpts),prntval(maxpts),ss(jsolve*maxpts)
        dimension tw(maxpts)
        dimension xsh(maxpts),ysh(maxpts)  !shock location
        common /param/pstar    !for passing to subroutines for arbitrary shapes
        data pi/3.1415926535/,ksprnt/1/,ksprof/5/
*      *(print info every ksprnt'th soln station; print profile info
*      * (every ksprof'th soln station)
*      need dense printing of soln for gortler work to get good values
*      for derivatives of wall height to get streamwise curvature!
*
        write (*,*) 'enter root filename for transfer: '
        read (*,5) root
    5 format(a20)
        ileng = index(root,' ') - 1
        write (*,*) 'enter 0 if this is a Sivells test, '
        write (*,*) 'enter 1 if this is a flat plate test, '
        write (*,*) 'enter 2 if this is a Lees modified newtonian test: '
        write (*,*) 'enter 3 if Euler output for body is to be read: '
        read (*,*) imodel
        if (imodel .eq. 0) then
          write (*,*) 'Sivells test'
          infile(1:ileng) = root(1:ileng)
          infile(ileng+1:ileng+3) = '.bl'
          write (*,*) 'reading input data from file ',infile
          open(unit=1,file=infile,status='old')
          read (1,10) text
   10   format(a80)
```

```
      read (1,10) text
      read (1,*) numpts
      if (numpts .gt. maxpts) stop 'too many points'
      do 50 i=1,numpts
        read (1,*) x(i),y(i),pepo(i)
 50   continue
      close (unit=1)
*     (done reading in info from sivells output file)
    else if (imodel .eq. 1) then
      write (*,*) 'enter numpts, mach, gam, plend: '
      read (*,*) numpts,amach,gam,plend
      gmexp = gam/(gam-1)
      gmfact = (gam-1)/2.0
      denom = (1.0 + gmfact*amach**2)**gmexp
      pep0 = 1.0/denom
      write (*,*) ' gives pep0= ',pep0
      do 60 i = 1,numpts
        x(i) = plend*float(i-1)/float(numpts-1)
        y(i) = 1.0  !not 0.0, messes up computations
        pepo(i) = pep0
 60   continue
    else if (imodel .eq. 2) then
      write (*,*) 'this is a modified newtonian test;'
      write (*,*) 'you must enter the shape in source code'
      write (*,*) 'enter numpts, mach, pstar, plend: '
      read (*,*) numpts,amach,pstar,plend
      gam = 1.4 !air
      if (numpts .gt. maxpts) stop 'too many points'
* now compute pressure ahead of shock, ratio to total pressure
*   in stilling chamber
      gmexp = gam/(gam-1)
      gmfact = (gam-1)/2.0
      denom = (1.0 + gmfact*amach**2)**gmexp
      pinfp0 = 1.0/denom
      write (*,*) ' gives pinfinity/p0= ',pinfp0
* now compute stagnation or total pressure behind normal shock,
*   ratio to p_infty ahead of shock(see Anderson p. 54, 3.17)
      denom1 = 4*gam*amach**2 - 2*(gam-1)
      piece1 = ( (gam+1)**2 * amach**2/denom1 )**(gmexp)
      piece2 = (1-gam+2*gam*amach**2)/(gam+1)
      ptpinf = piece1*piece2
      ptp0 = ptpinf*pinfp0
      write (*,*) 'pstag on body/p infty is ',ptpinf
      write (*,*) 'gives pstag on body/pstag in stilling=',ptp0
      cpmax = (2.0/(gam*amach**2)) * (ptpinf - 1) !Anderson 3.19
      write (*,*) 'cpmax computed as ',cpmax
* now compute body shape
*   for non-sphere shape, do this in subroutine
      write (*,*) 'passing to blunts; pstar,plend=',pstar,plend
      pause 'need to incorporate subroutine with body shape!!'
*     call blunts(plend,numpts,x,y,theta)
      do 80 i = 1,numpts
```

```
* now compute ratio of pe to ptotal ahead of shock, using Lees
*    modified newtonian thy - formula derived using p. 54
         pepo(i) = (ptp0 - pinfp0)*(sin(theta(i)))**2 + pinfp0
  80    continue
       else if (imodel .eq. 3) then
         write (*,*) 'working for euler data for blunt body'
         write (*,*) 'enter mach, gamma: '
         read (*,*) amach,gam
* now compute pressure ahead of shock, ratio to total pressure
*   in stilling chamber
         gmexp = gam/(gam-1)
         gmfact = (gam-1)/2.0
         denom = (1.0 + gmfact*amach**2)**gmexp
         pinfp0 = 1.0/denom
         write (*,*) ' gives pinfinity/p0= ',pinfp0
* now compute stagnation or total pressure behind normal shock,
*   ratio to p_infty ahead of shock(see Anderson p. 54, 3.17)
         denom1 = 4*gam*amach**2 - 2*(gam-1)
         piece1 = ( (gam+1)**2 * amach**2/denom1 )**(gmexp)
         piece2 = (1-gam+2*gam*amach**2)/(gam+1)
         ptpinf = piece1*piece2
         ptp0 = ptpinf*pinfp0
         write (*,*) 'pstag on body/p infty is ',ptpinf
         write (*,*) 'gives pstag on body/pstag in stilling=',ptp0
         write (*,*) 'reading euler data for blunt body: '
         infile(1:ileng) = root(1:ileng)
         infile(ileng+1:ileng+4) = '.eul'
         write (*,*) 'reading input data from file ',infile
         open(unit=1,file=infile,status='old')
         read (1,90) lineskip
  90    format(i6)    !number of lines to skip
         do 92 i = 1,lineskip  !skip 'lineskip' lines of text
            read (1,91) text
  91       format(a80)
  92    continue
         read (1,*) numpts
         if (numpts .gt. maxpts) stop 'too many points'
         do 95 i=1,numpts
            read (1,*) x(i),y(i),pepinf !read euler data for pressure
            pepo(i) = pepinf*pinfp0
  95    continue
*    Now read shock location data:
         read (1,90) lineskip
         do 96 i = 1,lineskip  !skip 'lineskip' lines of text
            read (1,91) text
  96    continue
         read (1,*) numshpts
         if (numshpts .gt. maxpts) stop 'too many points'
         do 97 i=1,numshpts
            read (1,*) xsh(i),ysh(i) !read euler data for shock location
  97    continue
         write (*,*) 'done reading from file'
```

```
      else
          stop 'imodel must be 0,1,2, or 3'
      end if
* now check computed values
      do 150 i = 1,numpts
        if (imodel .gt. 1) then
          if (pepo(i)-ptp0 .gt. -0.01*ptp0) then !arbitrary nearness
            write (*,*) 'pepo(',i,')= ',pepo(i)
            write (*,*) 'ptp0= ',ptp0
            write (*,*) 'if first gt second when computed by VGBLP,'
            write (*,*) 'this will give surface static pressure larger'
            write (*,*) ' than the total pressure on the surface'
            write (*,*) 'this would be a fatal error in VGBLP'
            if (pepo(i) .gt. ptp0) then
              write (*,*) 'reducing pepo(',i,') to 0.99999*ptp0'
              write (*,*) ' to forstall error in VGBLP'
              pepo(i) = 0.99999*ptp0
            end if
          end if
        end if
  150 continue
*
*  now read in parametric info from parameter file
*
      parmfl(1:ileng) = root(1:ileng)
      parmfl(ileng+1:ileng+3) = '.re'
      write (*,*) 'reading reynolds number scaling info from ',parmfl
      open(unit=1,file=parmfl,status='old')
      read (1,5) outfile    !read filename to write to
      read (1,*) throat      !throat radius in feet
* (assumes input scaled so throat radius is one unit) *
      read (1,*) prandtl
* ptotal,ttotal,xmach are conditions at infinity - see p. 44
*   for nozzle are stagnation chamber conditions
* for non-nozzle, xmach seems to affect mostly the computations
*   involving the flow behind the shock.  Should be freestream values!!
      read (1,*) ptotal
      read (1,*) rgas
      read (1,*) ttotal   !ahead of le shock
      read (1,*) xmachi
      if (imodel .ne. 0) then
        if (xmachi .lt. 1.0) then
          write (*,*) 'xmach given as ',xmachi
          write (*,*) 'should be freestream value ahead of shock,'
          write (*,*) ' not the value at stagnation!!'
        end if
      end if
      close (unit=1)
*
* now set defaults for input to harris program (besides harris's)
*
      if (imodel .eq. 2 .or. imodel .eq. 3) then
```

```
         ibody = 1    !stag pt at nose
         j = 1        !axisymmetric
        else
         ibody = 2    !no stagnation point at nose
         j = 0        !2D
        end if
        ie = 51    !from test case number 4
        if (imodel .eq. 3) then
         ientro = 2  !variable entropy calculation
        else
         ientro = 1
        end if
        igeom = 1    !create coords using geometric series; need xk,ie,xend!!
        kodunit=0    !US units
        if (imodel .eq. 0) then
         kodwal=1     !specify wall temperature distribution (no time to heat)
        else
         kodwal=2     !specify adiabatic wall
        end if
        iend1 = jsolve*numpts !number of soln stations
        proinc = 10.0 ! hopefully, none
        prntinc = 10.0
        sst = 1e+20 !no transition on body until then (laminar flow)
        if (imodel .gt. 1) then
         wave = 90.0  !shock wave angle at s=0, needed for test case 4 type flows
        else
         wave = 0.0  !needed for shockless type flows
        end if
c       xend = 120  !from blasius test case
        xend = 10    !as in test case 4
c       xk = 1.275  !value used in test cases in book, sets grid
c       xk = 1.1    !because value used in text gives hyper-dense
*          grid near wall, which makes for difficulties.
c       xk = 1.0    !like test case number 4
c       xk = 1.05   !because 1.0 gives little near wall for sphere
        xk = 1.1     !because 1.05 gives not great resolution for stability
*
* compute the arc length along the wall (see (66) of harris paper)
*   (approximate with straight line segments between stations)
        s(1) = 0.0
        write (*,*) 'setting wall temp equal to total temp, beware!'
* model temp same as total temp, ambient
* note that total temperature behind shock is the same as ahead of shock
*             *(true at stagnation point, anyway)*
        tw(1) = ttotal
        do 100 i = 2,numpts
         s(i) = s(i-1) + sqrt( (x(i)-x(i-1))**2 + (y(i)-y(i-1))**2 )
         tw(i) = ttotal !set above, assumes same along wall
  100 continue
* compute the s stations to get soln at, and to write at, even spacing
*   in sqrt(s) normally, other power for other cases
        if (imodel .lt. 2) then
```

```
         power = 2.0
         write (*,*) 'using square root distribution of pts'
      else
* with sphere, have problems with stepsize increasing too rapidly near le
         power = 1.0
         write (*,*) 'using linear distribution of pts, good for blunt'
*        *(try this, since problems with T<0 at le)*like test case 4
      end if
      root1 = 1.0/power
      rsinc = (s(numpts)-s(1))**root1/float(iend1)  !try-
      ss(1) = rsinc**power
      ss(2) = ss(1)  !required
      ss(3) = ss(1)  !also required, actually
      srun = 3*ss(1) !running value of s
      iprnt = 0
      ipro = 0
      do 200 i = 4,iend1
        srunold = srun
        srun = ( (srunold)**root1 + rsinc )**power
        ss(i) = srun-srunold
        if (mod(i,ksprnt) .eq. 0 .or. i .eq. 1) then
          iprnt = iprnt + 1
          prntval(iprnt) = srun
        end if
        if (mod(i,ksprof) .eq. 0) then
          ipro = ipro + 1
          proval(ipro) = srun
        end if
 200  continue
*
* Now write out NAM1 namelist into file
*
      write (*,*) ' writing bl input to file ',outfile
      open(unit=2,file=outfile)
      write (2,*) ' &NAM1'
      write (2,*) ' IBODY=',ibody
      write (2,*) ' IE=',ie
      write (2,*) ' IEND1=',iend1
      write (*,*) 'may need to reset param.inc, note that '
      write (*,*) 'ie is now ',ie,' and iend1= ',iend1
      write (2,*) ' IENTRO=',ientro
      write (2,*) ' IGEOM=',igeom
      write (2,*) ' IPRO=',ipro
      write (2,*) ' IPRNT=',iprnt
      write (*,*) 'ipro and iprnt are ',ipro,iprnt
      write (2,*) ' J=',j
      write (2,*) ' KODUNIT=',kodunit
      write (2,*) ' KODWAL=',kodwal
      if (imodel .ne. 2) then
        phii = (180.0/pi)*atan( (y(2)-y(1))/(x(2)-x(1)) )
      else
        write (*,*) 'setting leading edge angle = 90 degrees'
```

```
        phii = 90.0
      end if
      write (2,*) ' PHII=',phii
      write (2,*) ' PR=',prandtl
      write (2,*) ' PRNTINC=',prntinc
      write (2,*) ' PRNTVAL=',(prntval(i)*throat,i=1,iprnt)
      write (2,*) ' PROINC=',proinc
      write (2,*) ' PROVAL=',(proval(i)*throat,i=1,ipro)
      write (2,*) ' PT1=',ptotal
      write (2,*) ' R=',rgas
      write (2,*) ' SST=',sst
      write (2,*) ' TT1=',ttotal
      write (2,*) ' WAVE=',wave
      write (2,*) ' XEND=',xend
      write (2,*) ' XK=',xk
      write (2,*) ' XMA=',xmachi
      write (2,*) ' &END'    !end of namelist input
* end of writing nam1. Now compute and write nam2:
      write (2,*) ' &NAM2'
      write (2,*) ' NUMBER=',numpts
      write (*,*) 'and NUMBER is ',numpts
      write (2,*) ' PE=',(pepo(i)*ptotal,i=1,numpts)
      write (2,*) ' RMI=',(y(i)*throat,i=1,numpts)
      write (2,*) ' S=',(s(i)*throat,i=1,numpts)
      write (2,*) ' SS=',(ss(i)*throat,i=1,iend1)
      if (imodel .eq. 0) then
        write (2,*) ' TW=',(tw(i),i=1,numpts)
      else
        write (2,500) numpts-1     !make adiabatic wall
  500 format(' QW=',i4,'*0.0,0.0') !,0.0 kluge for compiler bug
      end if
      write (2,*) ' Z=',(x(i)*throat,i=1,numpts)
      write (2,*) ' &END'
* end of writing nam2. Now write nam3, if required
      if (imodel .eq. 3) then   !doing entropy computations through shock
        write (2,*) '&NAM3'
        write (2,*) 'NUMBER=', numshpts
        write (*,*) 'now numshpts (JL) is ',numshpts
        write (2,*) 'RRS= ',(xsh(i)*throat,i=1,numshpts)
        write (2,*) 'ZZS= ',(ysh(i)*throat,i=1,numshpts)
      end if
      write (2,*) '/
      close (unit=2)
*
      stop 'end of makeblin'

      end
```

The following file is created by the program described above. The short Mach 2.4 nozzle data is shown as an example of this type of file. This file is labeled PARAM

and is the exact coordinates for the short Mach 2.4 nozzle. The first line is minimum and maximum x values. Then the values are x, minimum y, maximum y, minimum z, and maximum z for one quadrant of the nozzle. Therefore, at any x location, the contour in the centerplane is found by taking the minimum z value and the maximum y value.

```
-0.133460  0.725013
-0.133460 0.  7.73838E-02 0.  7.73838E-02
-0.129853 0.  7.67813E-02 0.  7.67813E-02
-0.126246 0.  7.61887E-02 0.  7.61887E-02
-0.122639 0.  7.56108E-02 0.  7.56108E-02
-0.119032 0.  7.50485E-02 0.  7.50485E-02
-0.115425 0.  7.45017E-02 0.  7.45017E-02
-0.111818 0.  7.39707E-02 0.  7.39707E-02
-0.108211 0.  7.34556E-02 0.  7.34556E-02
-1.04604E-01 0.  7.29563E-02 0.  7.29563E-02
-1.00997E-01 0.  7.24735E-02 0.  7.24735E-02
-9.73897E-02 0.  7.20066E-02 0.  7.20066E-02
-9.37827E-02 0.  7.15555E-02 0.  7.15555E-02
-9.01757E-02 0.  7.11208E-02 0.  7.11208E-02
-8.65687E-02 0.  7.07023E-02 0.  7.07023E-02
-8.29614E-02 0.  7.03000E-02 0.  7.03000E-02
-7.93544E-02 0.  6.99138E-02 0.  6.99138E-02
-7.57474E-02 0.  6.95441E-02 0.  6.95441E-02
-7.21404E-02 0.  6.91905E-02 0.  6.91905E-02
-6.85334E-02 0.  6.88531E-02 0.  6.88531E-02
-6.49264E-02 0.  6.85321E-02 0.  6.85321E-02
-6.13194E-02 0.  6.82277E-02 0.  6.82277E-02
-5.77124E-02 0.  6.79396E-02 0.  6.79396E-02
-5.41054E-02 0.  6.76677E-02 0.  6.76677E-02
-5.04983E-02 0.  6.74126E-02 0.  6.74126E-02
-4.68913E-02 0.  6.71737E-02 0.  6.71737E-02
-4.32843E-02 0.  6.69511E-02 0.  6.69511E-02
-3.96773E-02 0.  6.67454E-02 0.  6.67454E-02
-3.60703E-02 0.  6.65561E-02 0.  6.65561E-02
-3.24630E-02 0.  6.63833E-02 0.  6.63833E-02
-2.88561E-02 0.  6.62272E-02 0.  6.62272E-02
-2.52492E-02 0.  6.60880E-02 0.  6.60880E-02
-2.16421E-02 0.  6.59651E-02 0.  6.59651E-02
-1.80351E-02 0.  6.58594E-02 0.  6.58594E-02
-1.44281E-02 0.  6.57701E-02 0.  6.57701E-02
-1.08211E-02 0.  6.56975E-02 0.  6.56975E-02
-7.21404E-03 0.  6.56417E-02 0.  6.56417E-02
-3.60700E-03 0.  6.56015E-02 0.  6.56015E-02
 4.41978E-08 0.  6.55820E-02 0.  6.55820E-02
 3.60703E-03 0.  6.55835E-02 0.  6.55835E-02
 7.21407E-03 0.  6.55945E-02 0.  6.55945E-02
 1.08211E-02 0.  6.56207E-02 0.  6.56207E-02
 1.44281E-02 0.  6.56640E-02 0.  6.56640E-02
 1.80351E-02 0.  6.57234E-02 0.  6.57234E-02
```

```
2.16422E-02  0.    6.57990E-02  0.    6.57990E-02
2.52492E-02  0.    6.58898E-02  0.    6.58898E-02
2.88562E-02  0.    6.59959E-02  0.    6.59959E-02
3.24633E-02  0.    6.61163E-02  0.    6.61163E-02
3.60703E-02  0.    6.62504E-02  0.    6.62504E-02
3.96773E-02  0.    6.63973E-02  0.    6.63973E-02
4.32843E-02  0.    6.65564E-02  0.    6.65564E-02
4.68913E-02  0.    6.67268E-02  0.    6.67268E-02
5.04983E-02  0.    6.69076E-02  0.    6.69076E-02
5.41054E-02  0.    6.70981E-02  0.    6.70981E-02
5.77124E-02  0.    6.72974E-02  0.    6.72974E-02
6.13194E-02  0.    6.75047E-02  0.    6.75047E-02
6.49264E-02  0.    6.77195E-02  0.    6.77195E-02
6.85334E-02  0.    6.79414E-02  0.    6.79414E-02
7.21407E-02  0.    6.81697E-02  0.    6.81697E-02
7.57477E-02  0.    6.84038E-02  0.    6.84038E-02
7.93547E-02  0.    6.86434E-02  0.    6.86434E-02
8.29617E-02  0.    6.88878E-02  0.    6.88878E-02
8.65687E-02  0.    6.91369E-02  0.    6.91369E-02
9.01757E-02  0.    6.93902E-02  0.    6.93902E-02
9.37827E-02  0.    6.96471E-02  0.    6.96471E-02
9.73897E-02  0.    6.99074E-02  0.    6.99074E-02
1.00997E-01  0.    7.01711E-02  0.    7.01711E-02
1.04604E-01  0.    7.04378E-02  0.    7.04378E-02
0.108211  0.    7.07069E-02  0.    7.07069E-02
0.111818  0.    7.09785E-02  0.    7.09785E-02
0.115425  0.    7.12522E-02  0.    7.12522E-02
0.119032  0.    7.15277E-02  0.    7.15277E-02
0.122639  0.    7.18051E-02  0.    7.18051E-02
0.126246  0.    7.20840E-02  0.    7.20840E-02
0.129853  0.    7.23644E-02  0.    7.23644E-02
0.133460  0.    7.26463E-02  0.    7.26463E-02
0.137067  0.    7.29289E-02  0.    7.29289E-02
0.140674  0.    7.32130E-02  0.    7.32130E-02
0.144281  0.    7.34976E-02  0.    7.34976E-02
0.147888  0.    7.37829E-02  0.    7.37829E-02
0.151495  0.    7.40691E-02  0.    7.40691E-02
0.155102  0.    7.43560E-02  0.    7.43560E-02
0.158709  0.    7.46431E-02  0.    7.46431E-02
0.162316  0.    7.49308E-02  0.    7.49308E-02
0.165923  0.    7.52188E-02  0.    7.52188E-02
0.169530  0.    7.55072E-02  0.    7.55072E-02
0.173137  0.    7.57958E-02  0.    7.57958E-02
0.176744  0.    7.60848E-02  0.    7.60848E-02
0.180351  0.    7.63737E-02  0.    7.63737E-02
0.183958  0.    7.66627E-02  0.    7.66627E-02
0.187565  0.    7.69522E-02  0.    7.69522E-02
0.191172  0.    7.72415E-02  0.    7.72415E-02
0.194779  0.    7.75311E-02  0.    7.75311E-02
0.198386  0.    7.78203E-02  0.    7.78203E-02
0.201993  0.    7.81102E-02  0.    7.81102E-02
0.205600  0.    7.83994E-02  0.    7.83994E-02
```

0.209207	0.	7.86887E-02	0.	7.86887E-02
0.212814	0.	7.89779E-02	0.	7.89779E-02
0.216421	0.	7.92672E-02	0.	7.92672E-02
0.220028	0.	7.95565E-02	0.	7.95565E-02
0.223635	0.	7.98457E-02	0.	7.98457E-02
0.227243	0.	8.01347E-02	0.	8.01347E-02
0.230850	0.	8.04239E-02	0.	8.04239E-02
0.234457	0.	8.07129E-02	0.	8.07129E-02
0.238064	0.	8.10021E-02	0.	8.10021E-02
0.241671	0.	8.12911E-02	0.	8.12911E-02
0.245278	0.	8.15803E-02	0.	8.15803E-02
0.248885	0.	8.18699E-02	0.	8.18699E-02
0.252492	0.	8.21598E-02	0.	8.21598E-02
0.256099	0.	8.24496E-02	0.	8.24496E-02
0.259706	0.	8.27398E-02	0.	8.27398E-02
0.263313	0.	8.30297E-02	0.	8.30297E-02
0.266920	0.	8.33195E-02	0.	8.33195E-02
0.270527	0.	8.36094E-02	0.	8.36094E-02
0.274134	0.	8.38986E-02	0.	8.38986E-02
0.277741	0.	8.41876E-02	0.	8.41876E-02
0.281348	0.	8.44762E-02	0.	8.44762E-02
0.284955	0.	8.47643E-02	0.	8.47643E-02
0.288562	0.	8.50520E-02	0.	8.50520E-02
0.292169	0.	8.53388E-02	0.	8.53388E-02
0.295776	0.	8.56250E-02	0.	8.56250E-02
0.299383	0.	8.59103E-02	0.	8.59103E-02
0.302990	0.	8.61944E-02	0.	8.61944E-02
0.306598	0.	8.64776E-02	0.	8.64776E-02
0.310204	0.	8.67592E-02	0.	8.67592E-02
0.313810	0.	8.70393E-02	0.	8.70393E-02
0.317419	0.	8.73176E-02	0.	8.73176E-02
0.321025	0.	8.75940E-02	0.	8.75940E-02
0.324633	0.	8.78684E-02	0.	8.78684E-02
0.328239	0.	8.81405E-02	0.	8.81405E-02
0.331845	0.	8.84106E-02	0.	8.84106E-02
0.335454	0.	8.86779E-02	0.	8.86779E-02
0.339060	0.	8.89431E-02	0.	8.89431E-02
0.342668	0.	8.92058E-02	0.	8.92058E-02
0.346274	0.	8.94661E-02	0.	8.94661E-02
0.349880	0.	8.97237E-02	0.	8.97237E-02
0.353489	0.	8.99785E-02	0.	8.99785E-02
0.357095	0.	9.02309E-02	0.	9.02309E-02
0.360703	0.	9.04805E-02	0.	9.04805E-02
0.364309	0.	9.07274E-02	0.	9.07274E-02
0.367918	0.	9.09715E-02	0.	9.09715E-02
0.371524	0.	9.12129E-02	0.	9.12129E-02
0.375130	0.	9.14516E-02	0.	9.14516E-02
0.378738	0.	9.16872E-02	0.	9.16872E-02
0.382344	0.	9.19201E-02	0.	9.19201E-02
0.385953	0.	9.21502E-02	0.	9.21502E-02
0.389559	0.	9.23776E-02	0.	9.23776E-02
0.393165	0.	9.26019E-02	0.	9.26019E-02

0.396773	0.	9.28235E-02	0.	9.28235E-02
0.400379	0.	9.30420E-02	0.	9.30420E-02
0.403988	0.	9.32575E-02	0.	9.32575E-02
0.407594	0.	9.34703E-02	0.	9.34703E-02
0.411200	0.	9.36800E-02	0.	9.36800E-02
0.414808	0.	9.38869E-02	0.	9.38869E-02
0.418414	0.	9.40908E-02	0.	9.40908E-02
0.422023	0.	9.42917E-02	0.	9.42917E-02
0.425629	0.	9.44898E-02	0.	9.44898E-02
0.429235	0.	9.46852E-02	0.	9.46852E-02
0.432843	0.	9.48775E-02	0.	9.48775E-02
0.436449	0.	9.50668E-02	0.	9.50668E-02
0.440058	0.	9.52531E-02	0.	9.52531E-02
0.443664	0.	9.54365E-02	0.	9.54365E-02
0.447270	0.	9.56173E-02	0.	9.56173E-02
0.450878	0.	9.57947E-02	0.	9.57947E-02
0.454484	0.	9.59696E-02	0.	9.59696E-02
0.458093	0.	9.61415E-02	0.	9.61415E-02
0.461699	0.	9.63104E-02	0.	9.63104E-02
0.465308	0.	9.64765E-02	0.	9.64765E-02
0.468913	0.	9.66399E-02	0.	9.66399E-02
0.472519	0.	9.68002E-02	0.	9.68002E-02
0.476128	0.	9.69575E-02	0.	9.69575E-02
0.479734	0.	9.71123E-02	0.	9.71123E-02
0.483343	0.	9.72641E-02	0.	9.72641E-02
0.486948	0.	9.74132E-02	0.	9.74132E-02
0.490554	0.	9.75595E-02	0.	9.75595E-02
0.494163	0.	9.77027E-02	0.	9.77027E-02
0.497769	0.	9.78436E-02	0.	9.78436E-02
0.501378	0.	9.79813E-02	0.	9.79813E-02
0.504983	0.	9.81163E-02	0.	9.81163E-02
0.508589	0.	9.82486E-02	0.	9.82486E-02
0.512198	0.	9.83785E-02	0.	9.83785E-02
0.515804	0.	9.85053E-02	0.	9.85053E-02
0.519413	0.	9.86296E-02	0.	9.86296E-02
0.523019	0.	9.87509E-02	0.	9.87509E-02
0.526624	0.	9.88698E-02	0.	9.88698E-02
0.530233	0.	9.89859E-02	0.	9.89859E-02
0.533839	0.	9.90996E-02	0.	9.90996E-02
0.537448	0.	9.92106E-02	0.	9.92106E-02
0.541054	0.	9.93191E-02	0.	9.93191E-02
0.544659	0.	9.94248E-02	0.	9.94248E-02
0.548268	0.	9.95279E-02	0.	9.95279E-02
0.551874	0.	9.96284E-02	0.	9.96284E-02
0.555483	0.	9.97266E-02	0.	9.97266E-02
0.559089	0.	9.98223E-02	0.	9.98223E-02
0.562697	0.	9.99156E-02	0.	9.99156E-02
0.566303	0.	1.00006E-01	0.	1.00006E-01
0.569909	0.	1.00094E-01	0.	1.00094E-01
0.573518	0.	1.00180E-01	0.	1.00180E-01
0.577124	0.	1.00264E-01	0.	1.00264E-01
0.580732	0.	1.00344E-01	0.	1.00344E-01

```
0.584338 0.  1.00423E-01 0.  1.00423E-01
0.587944 0.  1.00499E-01 0.  1.00499E-01
0.591553 0.  1.00574E-01 0.  1.00574E-01
0.595159 0.  1.00645E-01 0.  1.00645E-01
0.598767 0.  1.00714E-01 0.  1.00714E-01
0.602373 0.  1.00782E-01 0.  1.00782E-01
0.605979 0.  1.00846E-01 0.  1.00846E-01
0.609588 0.  1.00909E-01 0.  1.00909E-01
0.613194 0.  1.00970E-01 0.  1.00970E-01
0.616802 0.  1.01028E-01 0.  1.01028E-01
0.620408 0.  1.01085E-01 0.  1.01085E-01
0.624014 0.  1.01139E-01 0.  1.01139E-01
0.627623 0.  1.01191E-01 0.  1.01191E-01
0.631229 0.  1.01241E-01 0.  1.01241E-01
0.634837 0.  1.01289E-01 0.  1.01289E-01
0.638443 0.  1.01335E-01 0.  1.01335E-01
0.642049 0.  1.01379E-01 0.  1.01379E-01
0.645658 0.  1.01421E-01 0.  1.01421E-01
0.649264 0.  1.01462E-01 0.  1.01462E-01
0.652872 0.  1.01500E-01 0.  1.01500E-01
0.656478 0.  1.01536E-01 0.  1.01536E-01
0.660084 0.  1.01571E-01 0.  1.01571E-01
0.663693 0.  1.01604E-01 0.  1.01604E-01
0.667299 0.  1.01636E-01 0.  1.01636E-01
0.670907 0.  1.01665E-01 0.  1.01665E-01
0.674513 0.  1.01693E-01 0.  1.01693E-01
0.678122 0.  1.01719E-01 0.  1.01719E-01
0.681728 0.  1.01744E-01 0.  1.01744E-01
0.685334 0.  1.01767E-01 0.  1.01767E-01
0.688942 0.  1.01789E-01 0.  1.01789E-01
0.692548 0.  1.01808E-01 0.  1.01808E-01
0.696157 0.  1.01827E-01 0.  1.01827E-01
0.699763 0.  1.01844E-01 0.  1.01844E-01
0.703369 0.  1.01861E-01 0.  1.01861E-01
0.706977 0.  1.01875E-01 0.  1.01875E-01
0.710583 0.  1.01889E-01 0.  1.01889E-01
0.714192 0.  1.01901E-01 0.  1.01901E-01
0.717798 0.  1.01912E-01 0.  1.01912E-01
0.721404 0.  1.01922E-01 0.  1.01922E-01
0.725013 0.  1.01932E-01 0.  1.01932E-01
```

The following is the exact coordinates for the Long Mach 2.4 nozzle. The first line is minimum and maximum x values. Then the values are x, minimum y, maximum y, minimum z, and maximum z for one quadrant of the nozzle. Therefore, at any x location, the contour in the centerplane is found by taking the minimum z value and the maximum y value.

```
-0.174889  1.29548
-0.174889 0.  8.34442E-02 0.  8.34442E-02
```

```
-0.168412 0.  8.21951E-02 0.  8.21951E-02
-0.161934 0.  8.09820E-02 0.  8.09820E-02
-0.155457 0.  7.98119E-02 0.  7.98119E-02
-0.148980 0.  7.86859E-02 0.  7.86859E-02
-0.142502 0.  7.76042E-02 0.  7.76042E-02
-0.136025 0.  7.65679E-02 0.  7.65679E-02
-0.129548 0.  7.55770E-02 0.  7.55770E-02
-0.123070 0.  7.46315E-02 0.  7.46315E-02
-0.116593 0.  7.37317E-02 0.  7.37317E-02
-0.110115 0.  7.28783E-02 0.  7.28783E-02
 -1.03638E-01 0.  7.20709E-02 0.  7.20709E-02
 -9.71608E-02 0.  7.13101E-02 0.  7.13101E-02
 -9.06832E-02 0.  7.05956E-02 0.  7.05956E-02
 -8.42059E-02 0.  6.99278E-02 0.  6.99278E-02
 -7.77286E-02 0.  6.93073E-02 0.  6.93073E-02
 -7.12513E-02 0.  6.87336E-02 0.  6.87336E-02
 -6.47737E-02 0.  6.82069E-02 0.  6.82069E-02
 -5.82964E-02 0.  6.77278E-02 0.  6.77278E-02
 -5.18190E-02 0.  6.72962E-02 0.  6.72962E-02
 -4.53417E-02 0.  6.69124E-02 0.  6.69124E-02
 -3.88641E-02 0.  6.65765E-02 0.  6.65765E-02
 -3.23868E-02 0.  6.62885E-02 0.  6.62885E-02
 -2.59094E-02 0.  6.60486E-02 0.  6.60486E-02
 -1.94321E-02 0.  6.58572E-02 0.  6.58572E-02
 -1.29548E-02 0.  6.57146E-02 0.  6.57146E-02
 -6.47740E-03 0.  6.56195E-02 0.  6.56195E-02
0.  0.  6.55756E-02 0.  6.55756E-02
 6.47740E-03 0.  6.55856E-02 0.  6.55856E-02
 1.29548E-02 0.  6.56329E-02 0.  6.56329E-02
 1.94322E-02 0.  6.57210E-02 0.  6.57210E-02
 2.59095E-02 0.  6.58420E-02 0.  6.58420E-02
 3.23868E-02 0.  6.59886E-02 0.  6.59886E-02
 3.88644E-02 0.  6.61553E-02 0.  6.61553E-02
 4.53417E-02 0.  6.63382E-02 0.  6.63382E-02
 5.18190E-02 0.  6.65333E-02 0.  6.65333E-02
 5.82964E-02 0.  6.67384E-02 0.  6.67384E-02
 6.47740E-02 0.  6.69509E-02 0.  6.69509E-02
 7.12513E-02 0.  6.71691E-02 0.  6.71691E-02
 7.77286E-02 0.  6.73910E-02 0.  6.73910E-02
 8.42059E-02 0.  6.76156E-02 0.  6.76156E-02
 9.06835E-02 0.  6.78418E-02 0.  6.78418E-02
 9.71608E-02 0.  6.80692E-02 0.  6.80692E-02
 1.03638E-01 0.  6.82971E-02 0.  6.82971E-02
0.110115 0.  6.85257E-02 0.  6.85257E-02
0.116593 0.  6.87547E-02 0.  6.87547E-02
0.123070 0.  6.89832E-02 0.  6.89832E-02
0.129548 0.  6.92116E-02 0.  6.92116E-02
0.136025 0.  6.94395E-02 0.  6.94395E-02
0.142502 0.  6.96675E-02 0.  6.96675E-02
0.148980 0.  6.98958E-02 0.  6.98958E-02
0.155457 0.  7.01238E-02 0.  7.01238E-02
0.161934 0.  7.03518E-02 0.  7.03518E-02
```

0.168412	0.	7.05795E-02	0.	7.05795E-02
0.174889	0.	7.08075E-02	0.	7.08075E-02
0.181367	0.	7.10355E-02	0.	7.10355E-02
0.187844	0.	7.12635E-02	0.	7.12635E-02
0.194321	0.	7.14911E-02	0.	7.14911E-02
0.200799	0.	7.17191E-02	0.	7.17191E-02
0.207276	0.	7.19471E-02	0.	7.19471E-02
0.213754	0.	7.21748E-02	0.	7.21748E-02
0.220231	0.	7.24028E-02	0.	7.24028E-02
0.226708	0.	7.26308E-02	0.	7.26308E-02
0.233186	0.	7.28585E-02	0.	7.28585E-02
0.239663	0.	7.30865E-02	0.	7.30865E-02
0.246140	0.	7.33145E-02	0.	7.33145E-02
0.252618	0.	7.35425E-02	0.	7.35425E-02
0.259095	0.	7.37701E-02	0.	7.37701E-02
0.265573	0.	7.39981E-02	0.	7.39981E-02
0.272050	0.	7.42261E-02	0.	7.42261E-02
0.278527	0.	7.44541E-02	0.	7.44541E-02
0.285005	0.	7.46821E-02	0.	7.46821E-02
0.291482	0.	7.49101E-02	0.	7.49101E-02
0.297959	0.	7.51381E-02	0.	7.51381E-02
0.304437	0.	7.53661E-02	0.	7.53661E-02
0.310914	0.	7.55941E-02	0.	7.55941E-02
0.317391	0.	7.58220E-02	0.	7.58220E-02
0.323868	0.	7.60503E-02	0.	7.60503E-02
0.330345	0.	7.62783E-02	0.	7.62783E-02
0.336822	0.	7.65063E-02	0.	7.65063E-02
0.343302	0.	7.67346E-02	0.	7.67346E-02
0.349779	0.	7.69626E-02	0.	7.69626E-02
0.356256	0.	7.71909E-02	0.	7.71909E-02
0.362733	0.	7.74192E-02	0.	7.74192E-02
0.369210	0.	7.76472E-02	0.	7.76472E-02
0.375687	0.	7.78755E-02	0.	7.78755E-02
0.382164	0.	7.81038E-02	0.	7.81038E-02
0.388641	0.	7.83324E-02	0.	7.83324E-02
0.395121	0.	7.85613E-02	0.	7.85613E-02
0.401598	0.	7.87905E-02	0.	7.87905E-02
0.408075	0.	7.90197E-02	0.	7.90197E-02
0.414552	0.	7.92486E-02	0.	7.92486E-02
0.421029	0.	7.94772E-02	0.	7.94772E-02
0.427506	0.	7.97055E-02	0.	7.97055E-02
0.433983	0.	7.99341E-02	0.	7.99341E-02
0.440460	0.	8.01624E-02	0.	8.01624E-02
0.446940	0.	8.03910E-02	0.	8.03910E-02
0.453417	0.	8.06193E-02	0.	8.06193E-02
0.459894	0.	8.08476E-02	0.	8.08476E-02
0.466371	0.	8.10762E-02	0.	8.10762E-02
0.472848	0.	8.13045E-02	0.	8.13045E-02
0.479325	0.	8.15328E-02	0.	8.15328E-02
0.485802	0.	8.17611E-02	0.	8.17611E-02
0.492279	0.	8.19894E-02	0.	8.19894E-02
0.498760	0.	8.22180E-02	0.	8.22180E-02

0.505237	0.	8.24463E-02	0.	8.24463E-02
0.511714	0.	8.26746E-02	0.	8.26746E-02
0.518190	0.	8.29029E-02	0.	8.29029E-02
0.524668	0.	8.31312E-02	0.	8.31312E-02
0.531144	0.	8.33598E-02	0.	8.33598E-02
0.537621	0.	8.35880E-02	0.	8.35880E-02
0.544098	0.	8.38163E-02	0.	8.38163E-02
0.550579	0.	8.40446E-02	0.	8.40446E-02
0.557056	0.	8.42732E-02	0.	8.42732E-02
0.563533	0.	8.45015E-02	0.	8.45015E-02
0.570010	0.	8.47301E-02	0.	8.47301E-02
0.576487	0.	8.49584E-02	0.	8.49584E-02
0.582964	0.	8.51867E-02	0.	8.51867E-02
0.589441	0.	8.54153E-02	0.	8.54153E-02
0.595918	0.	8.56436E-02	0.	8.56436E-02
0.602398	0.	8.58722E-02	0.	8.58722E-02
0.608875	0.	8.61008E-02	0.	8.61008E-02
0.615352	0.	8.63291E-02	0.	8.63291E-02
0.621829	0.	8.65577E-02	0.	8.65577E-02
0.628306	0.	8.67860E-02	0.	8.67860E-02
0.634783	0.	8.70146E-02	0.	8.70146E-02
0.641260	0.	8.72432E-02	0.	8.72432E-02
0.647737	0.	8.74718E-02	0.	8.74718E-02
0.654217	0.	8.77004E-02	0.	8.77004E-02
0.660694	0.	8.79287E-02	0.	8.79287E-02
0.667171	0.	8.81573E-02	0.	8.81573E-02
0.673648	0.	8.83859E-02	0.	8.83859E-02
0.680125	0.	8.86145E-02	0.	8.86145E-02
0.686602	0.	8.88431E-02	0.	8.88431E-02
0.693079	0.	8.90720E-02	0.	8.90720E-02
0.699556	0.	8.93006E-02	0.	8.93006E-02
0.706036	0.	8.95292E-02	0.	8.95292E-02
0.712513	0.	8.97578E-02	0.	8.97578E-02
0.718990	0.	8.99867E-02	0.	8.99867E-02
0.725467	0.	9.02153E-02	0.	9.02153E-02
0.731944	0.	9.04439E-02	0.	9.04439E-02
0.738421	0.	9.06728E-02	0.	9.06728E-02
0.744898	0.	9.09014E-02	0.	9.09014E-02
0.751375	0.	9.11303E-02	0.	9.11303E-02
0.757855	0.	9.13589E-02	0.	9.13589E-02
0.764332	0.	9.15878E-02	0.	9.15878E-02
0.770809	0.	9.18167E-02	0.	9.18167E-02
0.777286	0.	9.20453E-02	0.	9.20453E-02
0.783763	0.	9.22742E-02	0.	9.22742E-02
0.790240	0.	9.25028E-02	0.	9.25028E-02
0.796717	0.	9.27317E-02	0.	9.27317E-02
0.803194	0.	9.29600E-02	0.	9.29600E-02
0.809674	0.	9.31883E-02	0.	9.31883E-02
0.816151	0.	9.34163E-02	0.	9.34163E-02
0.822628	0.	9.36437E-02	0.	9.36437E-02
0.829105	0.	9.38705E-02	0.	9.38705E-02
0.835582	0.	9.40963E-02	0.	9.40963E-02

0.842059	0.	9.43213E-02	0.	9.43213E-02
0.848536	0.	9.45453E-02	0.	9.45453E-02
0.855013	0.	9.47678E-02	0.	9.47678E-02
0.861493	0.	9.49882E-02	0.	9.49882E-02
0.867970	0.	9.52067E-02	0.	9.52067E-02
0.874447	0.	9.54228E-02	0.	9.54228E-02
0.880924	0.	9.56365E-02	0.	9.56365E-02
0.887401	0.	9.58474E-02	0.	9.58474E-02
0.893878	0.	9.60553E-02	0.	9.60553E-02
0.900355	0.	9.62604E-02	0.	9.62604E-02
0.906832	0.	9.64622E-02	0.	9.64622E-02
0.913312	0.	9.66606E-02	0.	9.66606E-02
0.919789	0.	9.68560E-02	0.	9.68560E-02
0.926266	0.	9.70480E-02	0.	9.70480E-02
0.932743	0.	9.72364E-02	0.	9.72364E-02
0.939220	0.	9.74214E-02	0.	9.74214E-02
0.945697	0.	9.76031E-02	0.	9.76031E-02
0.952174	0.	9.77807E-02	0.	9.77807E-02
0.958651	0.	9.79551E-02	0.	9.79551E-02
0.965131	0.	9.81255E-02	0.	9.81255E-02
0.971608	0.	9.82922E-02	0.	9.82922E-02
0.978085	0.	9.84553E-02	0.	9.84553E-02
0.984562	0.	9.86147E-02	0.	9.86147E-02
0.991039	0.	9.87701E-02	0.	9.87701E-02
0.997516	0.	9.89219E-02	0.	9.89219E-02
1.00399	0.	9.90698E-02	0.	9.90698E-02
1.01047	0.	9.92139E-02	0.	9.92139E-02
1.01695	0.	9.93538E-02	0.	9.93538E-02
1.02343	0.	9.94904E-02	0.	9.94904E-02
1.02990	0.	9.96230E-02	0.	9.96230E-02
1.03638	0.	9.97516E-02	0.	9.97516E-02
1.04286	0.	9.98766E-02	0.	9.98766E-02
1.04934	0.	9.99973E-02	0.	9.99973E-02
1.05581	0.	1.00114E-01	0.	1.00114E-01
1.06229	0.	1.00228E-01	0.	1.00228E-01
1.06877	0.	1.00337E-01	0.	1.00337E-01
1.07525	0.	1.00443E-01	0.	1.00443E-01
1.08172	0.	1.00545E-01	0.	1.00545E-01
1.08820	0.	1.00643E-01	0.	1.00643E-01
1.09468	0.	1.00738E-01	0.	1.00738E-01
1.10115	0.	1.00829E-01	0.	1.00829E-01
1.10763	0.	1.00916E-01	0.	1.00916E-01
1.11411	0.	1.01000E-01	0.	1.01000E-01
1.12059	0.	1.01080E-01	0.	1.01080E-01
1.12707	0.	1.01156E-01	0.	1.01156E-01
1.13354	0.	1.01229E-01	0.	1.01229E-01
1.14002	0.	1.01298E-01	0.	1.01298E-01
1.14650	0.	1.01365E-01	0.	1.01365E-01
1.15297	0.	1.01427E-01	0.	1.01427E-01
1.15945	0.	1.01486E-01	0.	1.01486E-01
1.16593	0.	1.01542E-01	0.	1.01542E-01
1.17241	0.	1.01595E-01	0.	1.01595E-01

```
1.17888 0.   1.01644E-01 0.   1.01644E-01
1.18536 0.   1.01691E-01 0.   1.01691E-01
1.19184 0.   1.01734E-01 0.   1.01734E-01
1.19832 0.   1.01775E-01 0.   1.01775E-01
1.20479 0.   1.01812E-01 0.   1.01812E-01
1.21127 0.   1.01846E-01 0.   1.01846E-01
1.21775 0.   1.01878E-01 0.   1.01878E-01
1.22422 0.   1.01907E-01 0.   1.01907E-01
1.23070 0.   1.01934E-01 0.   1.01934E-01
1.23718 0.   1.01958E-01 0.   1.01958E-01
1.24366 0.   1.01979E-01 0.   1.01979E-01
1.25013 0.   1.01999E-01 0.   1.01999E-01
1.25661 0.   1.02016E-01 0.   1.02016E-01
1.26309 0.   1.02031E-01 0.   1.02031E-01
1.26957 0.   1.02044E-01 0.   1.02044E-01
1.27604 0.   1.02055E-01 0.   1.02055E-01
1.28252 0.   1.02065E-01 0.   1.02065E-01
1.28900 0.   1.02073E-01 0.   1.02073E-01

1.29548 0.   1.02081E-01 0.   1.02081E-01
```

The program listed below is used for the generation of the grid for the Navier-Stokes calculation. It is called 3dgrid.f. Output from this file is binary data and is not shown here.

```
*    This program generates a three-dimensional nozzle grid for a N-S
*    calculation using an exponential stretching function adapted from
*    Dr. John Korte of NASA Langley.
*
*    by:
*
*    Tim Alcenius
*    Initially developed during LARSS Program participation
*    August 10, 1993
*
*    Define Variables.
*
     real xbeg, xend, delx, ymin(501), ymax(501), zmin(501), zmax(501)
     real sratio, beta, sexp, sfactc, xbar, ex, sratc, alp, sexc
     real xloc(501), x, y, z, sdec
     real r(305,97,97,3)
     integer choice, choice2, imax(1), jmax(1), kmax(1)
     integer i, j, k, l, m
*
*    Open input and output files and ask for stretching factor and
*    output format.
*
```

```
      open(1, file = 'param')
      open(2, file = 'geom', form = 'unformatted')
      print *, 'What stretching factor near the wall?'
      read *, beta
5     print *, 'Do you want Tecplot data?'
      print *, '1) yes'
      print *, '0) no'
      read *, choice
      if(choice .NE. 1 .AND. choice .NE. 0) then
        goto 5
      endif

*
*     Open files for Tecplot format.
*
      if(choice .EQ. 1) then
        open(3, file = 'grid')
        open(4, file = 'gridy')
        open(8, file = 'gridz')
      endif
*
*     Set maximum array dimensions for all directions and set ymax
*     variable for interpolation routine.
*
      imax(1) = 201
      jmax(1) = 65
      kmax(1) = 65
      do 4 i = 1,501
        ymax(i) = 0.000000000000000000000000000000
4     continue
*
*     Set all stretching constants.
*
      xbar = .1
      alp = 0
      sfactc = 1.25
      ex = 4.
      m = 1
      sratc = (sfactc +1.)/(sfactc - 1.)
      sratio = (beta+1.)/(beta-1.)
*
*     Write initial Tecplot data and inital data in binary format
*     for N-S calculation.
*
      if(chioce .EQ. 1) then
        write(3,*) 'TITLE="Streamline Plot For Supersonic Nozzle"'
        write(3,*) 'VARIABLES="X","Y","Z"'
      endif
      write(2)(imax(1),jmax(1),kmax(1),l=1,1)
*
*     Read in data from file containing nozzle coordinates.
*
```

```
      read(1,*) xbeg, xend
      delx = (xend-xbeg)/FLOAT(imax(1)-1)
      x = xbeg
      do 10 i = 1,228
        read(1,*) xloc(i), ymin(i), ymax(i), zmin(i), zmax(i)
10    continue
      do 20 i = 1, imax(1)
*
*     Call interpolation routine for placing equally spaced points
*     in the x-direction independant of the spacing of data in the
*     input file.
*
      call interpolate(x,xloc,ymin,ymax,zmin,zmax,ymn,ymx,zmn,zmx,i)
*
*     Stretching functions in y and z directions.
*
      do 30 j = 1, jmax(1)
        sexpy = (real(j-1)/real(jmax(1)-1) - alp )
   +         / (1.0 - alp)
        sdeny = 1. + sratio**sexpy
        sexcy = real(jmax(1)-j)/real(jmax(1)-1)
        sdecy = 1. + sratc**sexcy
          y = ymn
   .        + xbar * sexcy**ex
   .        * ( ( ymx - ymn )
   .        * ( 1.0 - sfactc + 2.0*sfactc/sdecy ) )
   .        + ( ( 1. - xbar ) + xbar * ( 1. - sexcy**ex ) )
   .        * (ymx - ymn )
   .        * ( 2.0 * alp / (2.0 * alp + 1)
   .        + beta / (2.0 * alp + 1) * (1.0 - 2.0/sdeny) )
        do 40 k = 1, kmax(1)
          sexpz = (real(k-1)/real(kmax(1)-1) - alp )
   +           / (1.0 - alp)
          sdenz = 1. + sratio**sexpz
          sexcz = real(kmax(1)-k)/real(kmax(1)-1)
          sdecz = 1. + sratc**sexcz
            z = zmn
   .          + xbar * sexcz**ex
   .          * ( ( zmx - zmn )
   .          * ( 1.0 - sfactc + 2.0*sfactc/sdecz ) )
   .          + ( ( 1. - xbar ) + xbar * ( 1. - sexcz**ex ) )
   .          * (zmx - zmn )
   .          * ( 2.0 * alp / (2.0 * alp + 1)
   .          + beta / (2.0 * alp + 1) * (1.0 - 2.0/sdenz) )
*
*     Write certain planes if Tecplot data is desired.
*
      if(choice .EQ. 1) then
        if(m .EQ. i) then
        if(flagx .EQ. 0) then
        write(3,*) 'ZONE T="Wall Countour",I=',jmax(1),',J=',
   +        kmax(1),',F=POINT'
```

```
              flagx = 1
              endif
              write(3,99) x, y, z
            endif
            if(y .EQ. ymx) then
             if(flagy .EQ. 0) then
              write(4,*) 'ZONE T="Wall Countour",I=',kmax(1),',J=',
     +        imax(1),',F=POINT'
              flagy = 1
             endif
              write(4,99) x, y, z
            endif
            if(z .LT. .0001 .AND. z .GT. 0) then
             if(flagz .EQ. 0) then
              write(8,*) 'ZONE T="Wall Countour",I=',jmax(1),',J=',
     +        imax(1),',F=POINT'
              flagz = 1
             endif
              write(8,99) x, y, z
            endif
            if(i .GT. m) then
              m = m+40
              flagx = 0
            endif
           endif
*
*    Put data in one array for use to write data in binary format.
*
            r(i,j,k,1) = x
            r(i,j,k,2) = y
            r(i,j,k,3) = z
40         continue
30        continue
          x = x + delx
20        continue
*
*    Write binary file of data for N-S calculation.
*
          write(2)(((((r(i,j,k,l)),i=1,imax(1)),j=1,jmax(1)),k=1,
     +    kmax(1)),l=1,3)
99        format(3(1x,e14.7))
          end




*
*      Interpolation subroutine.
*
          subroutine interpolate(x,xloc,ymin,ymax,zmin,zmax,ymn,ymx,zmn,
     +                zmx,i)
```

```
*
*    Define variables.
*
     real xloc(501), ymin(501), ymax(501),zmin(501), zmax(501)
     integer i,k
*
*    Set dummy variable so counter in program is unchanged.
*
     k = i
*
*    Make sure that counter does not exit the boundaries of the
*    nozzle parameter file.
*
100  if(ymax(k) .EQ. 0) then
       k = k-1
       goto 100
     endif
*
*    If the x location corresponds with the parameter file then use
*    the y and z values for that location.
*
     if(ABS(xloc(k)-x) .LT. .00001) then
200    ymn = ymin(k)
       ymx = ymax(k)
       zmn = zmin(k)
       zmx = zmax(k)
       return
     endif
*
*    Make sure that counter does not exit the boundaries of the
*    nozzle parameter file.
*
     if( k .LT. 1) then
       k = k+1
       goto 200
     endif
*
*    Find boundaries on x and determine y and z by using a first
*    order interpolation routine.
*
     if(xloc(k) .LT. x) then
       if(xloc(k+1) .GT. x) then
       ymn = ((ymin(k+1)-ymin(k))*(x-xloc(k)))/(xloc(k+1)-xloc(k))+
    +       ymin(k)
       ymx = ((ymax(k+1)-ymax(k))*(x-xloc(k)))/(xloc(k+1)-xloc(k))+
    +       ymax(k)
       zmn = ((zmin(k+1)-zmin(k))*(x-xloc(k)))/(xloc(k+1)-xloc(k))+
    +       zmin(k)
       zmx = ((zmax(k+1)-zmax(k))*(x-xloc(k)))/(xloc(k+1)-xloc(k))+
    +       zmax(k)
       return
     else
```

```
            k = k+1
            goto 100
          endif
        else
*
*       Find boundaries on x and determine y and z by using a first
*       order interpolation routine.
*
        if(xloc(k-1) .LT. x) then
          ymn = (ymin(k)-ymin(k-1))*(x-xloc(k-1))/(xloc(k)-xloc(k-1))+
     +        ymin(k-1)
          ymx = (ymax(k)-ymax(k-1))*(x-xloc(k-1))/(xloc(k)-xloc(k-1))+
     +        ymax(k-1)
          zmn = (zmin(k)-zmin(k-1))*(x-xloc(k-1))/(xloc(k)-xloc(k-1))+
     +        zmin(k-1)
          zmx = (zmax(k)-zmax(k-1))*(x-xloc(k-1))/(xloc(k)-xloc(k-1))+
     +        zmax(k-1)
          return
        else
          k = k-1
          goto 100
        endif
      endif
      return
      end
```

Appendix B   Post-Processing Code

The program below was developed to calculate the crossflow from the results of the numerical simulation.

```
*     This program has been made to calculate various flowfield
*     parameters after a three-dimensional N-S nozzle calculation.
*
*     by:
*
*     Tim Alcenius
*     Purdue University
*     August 13, 1994
*
*     Identify variables
*
      real mach(305,97,97), p(305,97,97), wmaxpct(305,97)
      real r(98,98,306,5), x(305,97,97,3)
      real uold, vold, wold, p0old, diffp(305), t2, t1
      real unew, vnew, wnew, pint, machint, p0new, ymax, capu, p0
      real s1, s2, s3, sdiv, ndistnew, prof(97,6), capum1
      real magV, shpfct(305,97), n1, n2, n3, q1, q2, q3
```

```fortran
      real qdiv, delst(305,97), theta(305,97), c5, c2, c3, c4
      real grtheta, beta, xxsi, yxsi, zxsi, xeta, yeta, zeta
      real rhoe, nue, crss, p01, p02, Hint, tdel10, gamma, pi
      real Ve, magVo, wmax, magucf, del10, H, rcf(305,97)
      real tnew, told, xnew, xold, znew, zold, rcfnew(305,97)
      real A, L, cst, mache, cstad, tstote, ndist, ndisttot
      real C1(305,97), rcfd2int, rcfdel2(305,97), tstadote
      real rhoold, rhonew, nminus, magucfo
      integer imax(1), jmax(1), kmax(1), i, j, k, m
      integer iref, kedge, jedge, flag
      pi = ACOS(-1.)
*
*     Open needed files and read data from LARCK output files written
*     in binary format.
*
      open(1, file = 'geom', form = 'unformatted')
      open(2, file = 'plt3d.q', form = 'unformatted')
      open(7, file = 'diffp')
      open(8, file = 'streammag')
      open(9, file = 'bledge')
      open(10, file = 'delst')
      open(11, file = 'theta')
      open(14, file = 'crossflow')
      open(15, file = 'corner')
      open(16, file = 'crossflowmag')
      read(1)(imax(m), jmax(m), kmax(m), m=1,1)
      read(1)((((x(i,j,k,m), i=1,imax(1)), j=1,jmax(1)), k=1,kmax(1)),
     +    m=1,3)
      read(2)(imax(m), jmax(m), kmax(m), m=1,1)
      read(2) c5, c2, c3, c4
      read(2)((((r(j,k,i,m), i=1,imax(1)), j=1,jmax(1)), k=1,kmax(1)),
     +    m=1,5)
      imax(1) = imax(1) - 1
      jmax(1) = jmax(1) - 1
      kmax(1) = kmax(1) - 1
*
*     Set-up Tecplot format in top of output files.
*
      write(7,*)'TITLE="Delta P"'
      write(7,*)'VARIABLES="x","delta P"'
      write(7,*)'ZONE T="planes",I=',imax(1)-1,',F=POINT'
      write(8,*)'TITLE="Streamwise"'
      write(8,*)'VARIABLES="y","V"'
      write(9,*)'TITLE="Streamwise"'
      write(9,*)'VARIABLES="y","edge"'
      write(10,*)'TITLE="delst"'
      write(10,*)'VARIABLES="x","delst"'
      write(10,*)'ZONE T="planes",I=',imax(1)-1,',F=POINT'
      write(11,*)'TITLE="theta"'
      write(11,*)'VARIABLES="x","theta"'
      write(11,*)'ZONE T="planes",I=',imax(1)-1,',F=POINT'
      write(14,*)'TITLE="Crossflow Re"'
```

```
      write(14,*)'VARIABLES="x","y","Conventional","Reed&Haynes",
     +     "Wmax/Ue","R","Arnal","Arnal C1","Shp"'
      write(14,*)'ZONE T="planes",I=',jmax(1)-2,',J=',imax(1)-
     +     1,',F=POINT'
      write(15,*)'TITLE="Corner"'
      write(15,*)'VARIABLES="x","y","u","v","mach"'
      write(15,*)'ZONE T="planes",I=',jmax(1),',J=',imax(1)-1,',F=POINT'
      write(16,*)'TITLE="Crossflow"'
      write(16,*)'VARIABLES="y","w"'

*
*     Calculate variables u, v, w from conserved variables rho*u,
*     rho*v, and rho*w.  Also pressure, Mach number,
*     and total pressure.
*
      do 10 i= 1,imax(1)
       do 20 j = 1,jmax(1)
        do 30 k = 1,kmax(1)
         do 40 m = 2,4
          if(m .EQ. 2) r(j,k,i,2) = r(j,k,i,2)/r(j,k,i,1)
          if(m .EQ. 3) r(j,k,i,3) = r(j,k,i,3)/r(j,k,i,1)
          if(m .EQ. 4) r(j,k,i,4) = r(j,k,i,4)/r(j,k,i,1)
40       continue
         p(i,j,k) = .4*(r(j,k,i,5)-.5*r(j,k,i,1)*(r(j,k,i,2)**2+
     +        r(j,k,i,3)**2+r(j,k,i,4)**2))
         mach(i,j,k) = SQRT((r(j,k,i,2)**2+r(j,k,i,3)**2+
     +           r(j,k,i,4)**2)/(1.4*p(i,j,k)/r(j,k,i,1)))
30      continue
        wmaxpct(i,j) = -.0005
20     continue
10    continue
      p0 = p(2,1,1)*(1.+.2*mach(2,1,1)**2)**(3.5)
*
*     Call subroutine to outer limit of marching in any
*     constant i-plane.
*
      do 150 i = 2,imax(1)
      call findjedge(p0, jedge, mach, p, i, jmax)
      diffp(i) = (p(i,jmax(1),kmax(1))-p(i,1,kmax(1)))/p0
      write(7,*) x(i,1,1,1),diffp(i)
*
*     Calculate the inward normal to the wall
*
      do 200 j = 1, jedge
      iref = i
      xxsi = x(i+1,j,kmax(1),1)-x(i,j,kmax(1),1)
      yxsi = x(i+1,j,kmax(1),2)-x(i,j,kmax(1),2)
      zxsi = x(i+1,j,kmax(1),3)-x(i,j,kmax(1),3)
      xeta = x(i,j+1,kmax(1),1)-x(i,j,kmax(1),1)
      yeta = x(i,j+1,kmax(1),2)-x(i,j,kmax(1),2)
      zeta = x(i,j+1,kmax(1),3)-x(i,j,kmax(1),3)
      n1 = (yeta*zxsi-yxsi*zeta)/(SQRT((yeta*zxsi-yxsi*zeta)**2+
```

```
      +     (xeta*zxsi-xxsi*zeta)**2+(xxsi*yeta-yxsi*xeta)**2))
      n2 = -n1*((xeta*zxsi-xxsi*zeta)/(yeta*zxsi-yxsi*zeta))
      n3 = (-xxsi*n1-yxsi*n2)/zxsi
*
*     Set inital variables and reset all integral counters.
*
      H = 0.0
      Hint = 0.0
      wmax = 0.0000
      del10 = 0.
      delst(i,j) = 0.
      theta(i,j) = 0.
      rcfd2int = 0.
      told = p(i,j,kmax(1))/(287.*r(j,kmax(1),i,1))
      xold = x(i,j,kmax(1),1)
      zold = x(i,j,kmax(1),3)
      uold = r(j,kmax(1),i,2)
      vold = r(j,kmax(1),i,3)
      wold = r(j,kmax(1),i,4)
      rhoold = r(j,kmax(1),i,1)
      p0old= p(i,j,kmax(1))*(1.+.2*mach(i,j,kmax(1))**2)**(3.5)
      ndisttot = 0.0
*
*     Check to make sure normal vector doesn't cross a line outside
*     of the domain.
*
      if(n1 .LT. 0) then
        iref = i - 1
      else
        iref = i + 1
      endif
      if(iref .LE. 0 .OR. iref .GT. imax(1)) then
        wmax = 0.0
        goto 1010
      endif
      flag = 0
*
*     Find each location that the normal vector crosses a z = constant
*     line to find wmax, .1*wmax, and integrate to find H.
*
      do 220 k = kmax(1), 1, -1
        grtheta = ATAN(ABS(x(iref,j,k,3)-x(i,j,k,3))/
     +        ABS(x(iref,j,k,1)-x(i,j,k,1)))
        beta = ATAN(ABS(n1/n3))
        gamma = pi/2. - beta + grtheta
        delx3 = (x(i,j,kmax(1),3)-x(i,j,k,3))*SIN(beta)/
     +        SIN(gamma)
1000    diag = SQRT((x(iref,j,k,3)-x(i,j,k,3))**2+
     +        (x(iref,j,k,1)-x(i,j,k,1))**2)
*
*     Make sure normal vector crosses grid lines inside the domain.
*
```

```
          if(delx3 .GT. diag) then
            if(n1 .LT. 0) then
              iref = iref - 1
            else
              iref = iref + 1
            endif
            if(iref .LE. 0 .OR. iref .GT. imax(1)) then
              wmax = 0.0
              goto 1010
            endif
            goto 1000
          endif
*
*     Calculate normal distance in grid cell for integration using
*     trapezoidal method along line normal to the wall.  Interpolate
*     variables at each crossing and save temperature, distance,
*     and velocity components.  Finished when normal vector
*     crosses 98% of Po on the centerline.
*
          znew = x(i,j,k,3)+delx3*(x(iref,j,k,3)-x(i,j,k,3))/diag
          xnew = x(i,j,k,1)+delx3*(x(iref,j,k,1)-x(i,j,k,1))/diag
          t2 = p(iref,j,k)/(287.*r(j,k,iref,1))
          t1 = p(i,j,k)/(287.*r(j,k,i,1))
          tnew = (t1 + (t2-t1)*delx3/diag)
          ndist = SQRT((xnew-xold)**2+(znew-zold)**2)
          unew = (r(j,k,i,2) + (r(j,k,iref,2)-r(j,k,i,2))*
     +        delx3/diag)
          vnew = (r(j,k,i,3) + (r(j,k,iref,3)-r(j,k,i,3))*
     +        delx3/diag)
          wnew = (r(j,k,i,4) + (r(j,k,iref,4)-r(j,k,i,4))*
     +        delx3/diag)
          pint = (p(i,j,k) + (p(iref,j,k)-p(i,j,k))*
     +        delx3/diag)
          machint = (mach(i,j,k) + (mach(iref,j,k)-mach(i,j,k))*
     +        delx3/diag)
          rhonew = pint/(287.*tnew)
          pOnew= pint*(1.+.2*machint**2)**(3.5)
          if(pOnew .GT. .98*pO) then
            ndistnew = (.98*pO-pOold)*ndist/(pOnew-pOold)
            ndisttot = ndisttot + ndistnew
            prof(k,1) = told + ndistnew*(tnew-told)/ndist
            prof(k,2) = ndisttot
            prof(k,3) = uold + ndistnew*(unew-uold)/ndist
            prof(k,4) = vold + ndistnew*(vnew-vold)/ndist
            prof(k,5) = wold + ndistnew*(wnew-wold)/ndist
            prof(k,6) = rhoold + ndistnew*(rhonew-rhoold)/ndist
            mache = SQRT((prof(k,3)**2+prof(k,4)**2+prof(k,5)**2)/
     +          (1.4*287*prof(k,1)))
            rhoe = .98*pO/(287*prof(k,1)*(1.+.2*mache**2)**(3.5))
            nue = (.1716e-4*(prof(k,1)/273.111)**1.5*(383.444/
     +          (prof(k,1)+110.333)))/rhoe
            kedge = k
```

```
          goto 1020
        else
          ndisttot = ndisttot + ndist
          prof(k,1) = tnew
          prof(k,2) = ndisttot
          prof(k,3) = unew
          prof(k,4) = vnew
          prof(k,5) = wnew
          prof(k,6) = rhonew
        endif
*
*
*     Set all old variables to current values for next step in
*     do-loop.
*
        xold = xnew
        zold = znew
        told = tnew
        uold = unew
        vold = vnew
        wold = wnew
        rhoold = rhonew
        p0old = p0new
220   continue
*
*     Calculate crossflow direction unit normal.
*
1020    if((prof(kedge,3)*n3-prof(kedge,5)*n1) .NE. 0.) then
        q2 = 1.
        q3 = (-prof(kedge,3)*n2+n1*prof(kedge,4))/(prof(kedge,3)*
     +        n3-prof(kedge,5)*n1)
        q1 = -(prof(kedge,4)+q3*prof(kedge,5))/prof(kedge,3)
        qdiv = SQRT(q1**2+q2**2+q3**2)
        q1 = q1/qdiv
        q2 = q2/qdiv
        q3 = q3/qdiv
      else
        q1 = 0.
        q2 = 1.
        q3 = 0.
      endif
*
*     Calculate streamiwse unit vector.
*
      s1 = 1.
      s3 = (q1*n2-q2*n1)/(n3*q2-q3*n2)
      s2 = -(s3*q3+q1)/q2
      sdiv = SQRT(s1**2+s2**2+s3**2)
      s1 = s1/sdiv
      s2 = s2/sdiv
      s3 = s3/sdiv
*
*     Find Wmax, del10, and integrate for H, dle*, Theta, and
```

```fortran
*    Rdel2 form Arnal AGARD R-786.
*
      magucfo = 0.
      magVo = 0.
      Ve = SQRT(prof(kedge,3)**2+prof(kedge,4)**2+
     +      prof(kedge,5)**2)
      do 260 k = kmax(1), kedge, -1
        magucf = prof(k,3)*q1 + prof(k,4)*q2 + prof(k,5)*q3
        magV = prof(k,3)*s1 + prof(k,4)*s2 + prof(k,5)*s3
        if(ABS(magucf) .GT. ABS(wmax) .AND. k .NE. kmax(1)) then
          wmax = magucf
        else
          if(k .EQ. kedge .AND. magucf*magucfo .LT. 0.) then
            magucf = -magucf
          endif
          if(ABS(magucf) .LE. .1*ABS(wmax) .AND. magucf*
     +      magucfo .GT. 0. .AND. ABS(magucfo) .GT. .1*
     +      ABS(wmax)) then
            if(ABS(magucfo-magucf) .LT. .000001) then
              nminus = 0.
            else
              nminus = (.1*wmax-magucf)*(prof(k,2)-prof(k+1,2))/
     +              (magucfo-magucf)
            endif
            del10 = prof(k,2) - nminus
            tdel10 = prof(k+1,1) + (prof(k,1)-prof(k+1,1))*
     +          (del10-prof(k+1,2))/(prof(k,2)-prof(k+1,2))
            H = Hint + .5*(del10-prof(k+1,2))*(tdel10+
     +              prof(k+1,1))/prof(kedge,1)
          endif
        endif
*
*    Write crossflow profiles approximately half-way between
*    corner and centerplane of the nozzle.
*
        if(j .EQ. 19) then
          if(flag .EQ. 0) then
            write(16,*)'ZONE T="planes",I=',kmax(1)-kedge+1,
     +',F=POINT'
            write(8,*)'ZONE T="planes",I=',kmax(1)-kedge+1,
     +',F=POINT'
            write(9,*) x(i,j,kedge,2),prof(kedge,2)
            flag = 1
          endif
          write(16,*) prof(k,2)/prof(kedge,2),magucf
          write(8,*) prof(k,2)/prof(kedge,2),magV
        endif
        Hint = Hint + .5*(prof(k-1,2)-prof(k,2))*
     +      (prof(k,1)+prof(k-1,1))/prof(kedge,1)
        if(k .NE. kmax(1)) then
          rcfd2int = rcfd2int + .5*(prof(k,2)-prof(k+1,2))*
     +              (ABS(magucf)+ABS(magucfo))
```

```
*
*     Calculate delta* and theta.
*
            capu = 1.-(prof(k,6)/prof(kedge,6))*(magV/Ve)
            capum1 = 1.-(prof(k+1,6)/prof(kedge,6))*(magVo/Ve)
            delst(i,j) = delst(i,j) + .5*(prof(k,2)-prof(k+
     +          1,2))*(capum1+capu)
            capu = (1.-capu)*(1.-(magV/Ve))
            capum1 = (1.-capum1)*(1.-(magVo/Ve))
            theta(i,j) = theta(i,j) + .5*(prof(k,2)-prof(k+1,2))*
     +          (capum1+capu)
          endif
          magucfo = magucf
          magVo = magV
260       continue
*
*     Calculate standar crossflow Reynolds number and crossflow
*     Reynolds number from Arnal.
*
1010    rcf(i,j) = ABS(wmax)*del10/nue
        rcfdel2(i,j) = rcfd2int/nue
        shpfct(i,j) = delst(i,j)/theta(i,j)
        if(shpfct(i,j) .GT. 2.3) then
          C1(i,j) = 300.*ATAN(.106/((shpfct(i,j)-2.3)**2.05))/pi
        else
          if(shpfct(i,j) .EQ. 2.3) then
            C1(i,j) = 150.
          else
            C1(i,j)=0.
          endif
        endif
*
*     Calculate crossflow Reynolds number according to eqns 5-12 in
*     AIAA 93-3054 by Reed and Haynes.
*
        A = SQRT(0.72)*0.2*mache**2
        tstote = 0.5 + 0.5*prof(kmax(1),1)/prof(kedge,1) + A/6.
        tstadote = 0.5 + 0.5*(1.+A) + A/6.
        cst = (SQRT(tstote)*(1+110.4/prof(kedge,1)))/(tstote+
     +      110.4/prof(kedge,1))
        cstad = (SQRT(tstadote)*(1+110.4/prof(kedge,1)))/
     +      (tstadote+110.4/prof(kedge,1))
        if(H .EQ. 0.) then
          H = 1.
        else
          H = del10/H
        endif
        L = (SQRT(cst/cstad)*(3.279+1.721*(1.+A)+0.664*A))/
     +      (5.+2.385*A)
        rcfnew(i,j) = H*L*rcf(i,j)
*
*     Calculate Wmax/Ue in % and set 0. to slightly greater
```

```
*    than 0. for use in divsor later.
*
     wmaxpct(i,j) = 100.*wmax/SQRT(prof(kedge,3)**2+
    +          prof(kedge,4)**2+prof(kedge,5)**2)
     if(ABS(wmaxpct(i,j)) .LT. 0.00005) then
       wmaxpct(i,j) = -.00005
     endif
     if(j .EQ. 1) then
       write(10,*) x(i,j,k,1), delst(i,j)
       write(11,*) x(i,j,k,1), theta(i,j)
     endif
200  continue
*
*    Write files for Reynolds number contours and diagonal
*    plane variables.
*
     do 230 m = 2, jmax(1)-1
       write(14,*) x(i,m,kmax(1),1),x(i,m,kmax(1),2),rcf(i,m),
    +        rcfnew(i,m),wmaxpct(i,m),rcfnew(i,m)/ABS(wmaxpct(i,m)),
    +        rcfdel2(i,m),C1(i,m),shpfct(i,m)
230  continue
     do 240 j = 1, jmax(1)
       do 250 k = 1, kmax(1)
       if(j .EQ. k) then
         write(15,*) x(i,j,k,1),SQRT(2.)*x(i,j,k,2),r(j,k,i,2),
    +          SQRT(r(j,k,i,3)**2+r(j,k,i,4)**2),mach(i,j,k)
       endif
250    continue
240  continue
150  continue
     end




*
*    This subroutine finds the boundary layer edge by determining
*    where the total pressure drops to 98% of its value on the
*    centerline of the nozzle.
*
*    Define variables
*
     subroutine findjedge(p0, jedge, mach, p, i, jmax)
     real locp0, p0, mach(305,97,97), p(305,97,97)
     integer flag, jedge, jmax(1), i, j
*
*    Calculate local p0.  If below 98% of the centerline value,
*    jedge is saved.
*
     flag = 0
     do 20 j = 1, jmax(1)
       locp0 = p(i,j,1)*(1.+.2*mach(i,j,1)**2)**(3.5)
```

```
       if(locp0 .LT. .98*p0 .AND. flag .NE. 1) then
          jedge = j-1
          flag = 1
       endif
20    continue
      return
      end
```